DAMPING AUGMENTATION OF HELICOPTER ROTORS USING MAGNETORHEOLOGICAL DAMPERS

by

Yongsheng Zhao

Dissertation submitted to the Faculty of the Graduate School of the
University of Maryland, College Park in partial fulfillment
of the requirements for the degree of
Doctor of Philosophy
2003

Advisory Committee:

Associate Professor Norman Wereley, Chair/Advisor
Professor Amr Baz
Professor Inderjit Chopra
Associate Professor Darryll J. Pines
Associate Professor Robert Sanner

ABSTRACT

Title of Dissertation: DAMPING AUGMENTATION OF HELICOPTER ROTORS USING MAGNETORHEOLOGICAL DAMPERS

Yongsheng Zhao, Doctor of Philosophy, 2003

Dissertation directed by: Associate Professor Norman Wereley
Department of Aerospace Engineering

This dissertation describes on investigation exploring the use of magnetorheological (MR) dampers to augment the stability of helicopter rotors. Helicopters with advanced soft in-plane rotors are susceptible to ground resonance instabilities due to the coupling of the lightly damped rotor lag modes and fuselage modes. Traditional passive lag dampers, such as hydraulic or elastomeric dampers, can be used to allievate these instabilities. However, these passive dampers suffer from the disadvantages that they produce large damper loads in forward flight conditions. These damper forces increase fatigue loads and reduce component life. Thus, it is desirable to have lag dampers controllable or adaptable, so that the damper can apply loads only when needed. MR fluid based dampers have recently been considered for helicopter lag damping augmentation

because the forces generated by these dampers can be controlled by an applied magnetic field.

In this dissertation, control schemes to integrate MR dampers with helicopters are developed and the influences of the MR dampers on rotorcraft ground resonance are studied. Specifically, the MR dampers are incorporated into the ground resonance model in two ways: using a linear equivalent viscous damping and using a nonlinear damper model. The feasibility of using MR dampers to stabilize ground resonance is studied. The open loop on-off control is utilized where MR dampers are turned on over RPM where ground resonance occurs, and turned off otherwise. To further explore the damping control ability of MR dampers, the nonlinear semi-active closed loop feedback control strategies are developed: feedback linearization control and sliding mode control. The performance of the two control strategies is evaluated using two examples: to stabilize an unstable rotor and to augment the stability of a marginally stable rotor.

In addition, the robustness of the closed loop control strategies is studied using two cases: damper degradation and parameter perturbation. In first case, it is assumed that some MR dampers are damaged which lead to an unstable or marginally stable rotor. The use of the remaining operational MR dampers to recover the stability margin is investigated. It is shown that using the developed control strategy, the MR dampers can successfully recover the stability and stability margin of the rotor in most studied cases. The robustness of parameter perturbations are studied by perturbing mass, damping, and stiffness parameters. The method to improve the robustness of the feedback linearization control is suggested and is approved feasible.

To evaluate the damping provided by lead lag dampers and predict the

aeromechnical instability, damping identification algorithms from rotor stability test data are developed. First, the linear damping identification is researched. Three existing methods: Hilbert transform, moving block method with time domain window, and wavelet transform are evaluated and compared. Hybrid algorithms combining the advantages of the three methods are developed and applied to experimental test data. A nonlinear damping identification algorithm designed specifically for the system with MR dampers is developed. The envelope of the free response of such system is derived and the damping identification problem is transformed to envelope detection problem, so that algorithms used in linear damping identification can be applied. For the single degree of freedom system, all three methods accurately identify dampings: Hilbert transform, moving block method with time domain window, and wavelet transform. For the system with persistent excitation such as rotor stability test data, the hybrid methods again show better performance than other methods.

DEDICATION

To my wife, parents, and my daughter

ACKNOWLEDGEMENTS

I would thank all the professors and my colleague students of the Alfred Gessow Rotorcraft Center and the Aerospace department of the University of Maryland for the help they gave me generously. I would thank all my committee members for their advises on my research. Especially, I would like to thank my advisor, Dr. Norman Wereley, for his guidance and encouragement throughout the course of this research, his motivation and his warmth and friendship, and his support at every stage.

Finally, I would thank my wife, Tao Yu, for all the sacrifice she made and all the endless support she gave me for the accomplishment of this work.

TABLE OF CONTENTS

LIST OF TABLES

LIST OF FIGURES

Nomenclature

$\overset{\star}{(\cdot)}$	Derivative with respect to azimuth, ψ
$\bar{(\cdot)}$	Nondimensionalized quantity
A_e	Amplitude of sinusoidal damper excitation
$a(t)$	Analytical envelope signal
$A_1(t_k)$	Fourier cosine coefficient at time t_k
$B_1(t_k)$	Fourier sine coefficient at time t_k
C, C_0	Damping matrices
C_{po}	Post-yield damping of MR damper
C_{pr}	Pre-yield damping of MR damper
C_x	Longitudinal support damping coefficient
C_y	Lateral support damping coefficient
C_ζ	Lag damping coefficient
$C_{\zeta,eq}$	Equivalent lag damping coefficient
$\bar{c}$	Control gain
E	Energy dissipated in a circle
F	Damper force
F_i	Damper force on each blade
F_y	Yield force of MR damper
G	Sliding surface gradient
K, K_0	Stiffness matrices

K_x	Longitudinal support stiffness
K_y	Lateral support stiffness
I_b	Blade mass moment of inertia
M, M_0	Inertial matrices
M_x	Longitudinal fuselage inertia
M_y	Lateral fuselage inertia
P, Q	Transform matrices
q, q_0, z	State vectors
R	Rotor radius
R_1	Distance between damper attachment
S_ζ	Blade first mass moment
SM	Stability margin
$\bar{u}, \bar{v}, \bar{V}$	Control input vector
ψ	Azimuth
ν_ζ	Blade lag frequency
ω_x	Longitudinal fuselage support frequency
ω_y	Lateral fuselage support frequency
Ω	Rotor rotational frequency
Ω_e	Frequency of sinusoidal damper excitation
ζ	Lag angle
ζ_0	Collective lag mode

ζ_2	Differential lag mode
ζ_{1c}	Longitudinal cyclic lag mode
ζ_{1s}	Lateral cyclic lag mode
ζ_{hf}	High frequency lag mode
ζ_{lf}	Low frequency lag mode
$\zeta_{(i)}$	Lag angle of blade i
$\overset{\star}{\zeta}_y$	Yield velocity
x_h	Longitudinal displacement relative to rotor radius
y_h	Lateral displacement relative to rotor radius
ϕ_g, λ	Positive constants
$y(t)$	Transient signal of interest
j	$\sqrt{-1}$
$\tilde{y}(t)$	Hilbert transform of $y(t)$
ζ	Viscous damping ratio
$\theta(t)$	Instantaneous phase signal
ϕ	Phase shift of signal
Ω	Natural frequency of 1/rev
Ω_{lag}	Natural frequency of the lag mode
ω_d	Damped natural frequency of transient
ω_n	Natural frequency of transient

Chapter 1

Introduction

Advanced rotor systems, such as the hingeless and bearingless rotors, greatly reduce the mechanical complexity of the helicopter rotor system by replacing traditional hinges and bearings with flexures or flexbeams. However, such rotors are soft in-plane, that is, the in-plane lag frequency is less than the rotor operational frequency, so that these rotors are susceptible to the problems of air and ground resonance. The augmentation of lag damping is the major stabilizing influence for both air and ground resonance, and evaluation of damping is a key step when predicting aeromechanical stabilities.

Traditionally, conventional articulated rotors have been equipped with hydraulic lag dampers to mitigate aeromechanical instabilities. For advanced hingless and bearingless rotors, elastomeric dampers are widely applied as lag dampers. Research on using MR dampers as lag dampers has also been being undertaken due the damping control ability of MR dampers[1].

To evaluate the benefits of the damping augmentation, rotor stability test must be performed and damping levels identified from the stability test data. In a typical stability test, the rotor is first trimmed and the modes of the interests

are excited through a rotor control mechanism called the swash plate. The excitation signal could be either the impulse signal or sinusoidal signal. The aim of such a test is to set up a forced vibratory response and allow it to decay after cutting off the excitation. The natural frequency and damping values of the modes of interest can be determined from the transient response.

The research in this thesis has two thrusts. The first thrust is to examine hub mounted MR dampers to stabilize ground resonance of helicopters. The second thrust is to develop a damping identification algorithm to estimate the lag damping from transient response data, so that the damping provided by the MR dampers can be evaluated. Before embarking on this investigation, we first assess the state of the art in these two research areas.

1.1 Field Responsive Fluids

MR and ER fluids belong to the class of smart materials. The properties of these fluids can be controlled by applying magnetic or electric field, respectively. The controllable effects of MR or ER fluid was observed as early as 1947[2, 3]. However, because of commercial doubts about the success of MR and ER devices, it is only in the past two decades that interest in research on MR and ER fluids has been reinvigorated[4, 5, 6].

According to previous research, the MR and ER fluids exhibit qualitatively similar rheological characteristics. When field is applied, both fluids form chain structures parallel to the direction of the applied field. A shear stress in excess of the yield stress needed to break the chain structures must be applied before the fluid can flow and exhibit visco-plastic behavior. Once the material has yielded,

flows like a Newtonian fluid with constant viscosity[7, 8, 9]. By changing the applied field, the yield stress can be controlled. According to this property, the idealized Bingham plastic model is widely used to describe the MR and ER fluid behavior[7]. This model provides a fairly accurate description of post-yield behavior and works well for high strain rates where the onset of flow has occurred, however, it does not accurately describe the fluid behavior for small strain rates below the yield point where there is some elastic deformation[8, 9].

In dynamic applications of ER and MR fluids such as dampers the exact description of material characteristics in the pre-yield region is important and the entire hysteresis cycle needs to be predicted. In dynamic models, the amplitude, inertia and frequency effects must be considered. Complex modulus approach was used to model the ER and MR fluid[10]. However, this approach implies a linearization in the frequency domain and is not accurate for modeling the nonlinear hysteresis. Gamota and Filisko (1991) proposed a mechanical model based on experimental Couette cell ER hysteresis measurements, which consisted of a 3-parameter solid element in series with viscous dashpot and Coulomb element. The high frequency experiments were performed solely in the pre-yield region. In an effort to simulate the response, authors examined the Fourier spectra of the stress response and obtained the coefficients of the different harmonics. The hysteresis loops were then constructed using the dominant harmonics and the onset of nonlinearity was well defined by the appearance of higher harmonic terms[11, 12, 13]. Kamath and Wereley[14] defined a nonlinear viscoelastic-plastic model for ER and MR fluids. This model used a viscoelastic mechanism for pre-yield behavior and a viscous-inertial model for the post-yield phase of the fluid. The two models were combined together using a nonlinear weighting

function and parameter identification was carried out using experimental results. The advantages of this modeling approach are that the nonlinear viscoelastic-plastic model accounts for dynamic behavior for varying field strengths and the model can be easily integrated into complex dynamic system simulation. Wereley, Pang, and Kamath[20] discussed four hysteresis models for linear stroke MR dampers based on a sinusoidal displacement excitation test and compared the models with the data from experiments on MR dampers. The four models are (1) the equivalent viscous model which is a standard linearization technique, (2) the non-linear Bingham plastic model which includes a yield force to a linear damping model, (3) the non-linear biviscous model which considers the pre-yield and post yield phases as linear damping model with two different damping coefficients, and (4) non-linear hysteretic biviscous model which enhance the previous model by adding hysteresis phenomenon to the force vs velocity behavior. The results showed that the three nonlinear models performed well when predicting energy dissipation, however, the non-linear hysteretic model provides the best representation of force vs. velocity hysteresis behavior. Wang and Gordaninejad[15] used the Herschel-Bulkley constitutive equation to develop a model for predicting the behavior of ER and MR dampers. In this model the compressibility of fluid was included. Wereley and Lindler[21] demonstrated that the ER damper with a leakage valve exhibited biviscous behavior. The leakage added to smooth out the force response of the damper. The leakage effects are described as a pre-yield viscosity and are directly included in the biviscous model.

Numerous applications of ER and MR fluids have been developed including clutches[16, 17], brakes[18], bearings, shock absorbers[18, 19], engine mounts,

and vibration suppression systems[17, 20, 21, 22, 23]. In these applications, a significant number focus on vibration control using MR and ER dampers, including the design of ER and MR dampers, dampers modeling, controller design, and experimental validation. Carlson et al[17] described the general design and state-of-the-art of controllable MR fluid devices. Two damper modes, the valve mode and the shear mode, were described. Examples of commercial MR fluid devices were illustrated: an MR damper for the suspension system of truck seat, an MR fluid rotary brake, an MR fluid vibration damper. The examples showed that MR fluid devices could provide desired system characteristics with feedback control, and are smooth acting, compact and require low power to operate. Jeon et al [22] showed that using MR dampers as a variable damper in an automotive suspension system can provide more effective performance than the conventional controllable damper. Lam et al[23] applied the MR dampers to suspension system of high speed vehicles to improve the ride comfort and safety. Dyke et al[24] applied MR dampers to civil engineering to prevent the structural damage on building due to earthquake. The benefit of using MR dampers is that its power requirement is low so that MR dampers can work when earthquake happens, in case the external power supply is ineffective. A damper provided by the Lord Corporation was modeled using experimental data and the clipped optimal control strategy based on acceleration feedback was applied. The effectiveness of this approach was illustrated through numerical examples. Kelso[25] provided a new MR fluid damper technology. In development of the technology, several parameters were addressed including (1) materials of construction of piston, cylinder and piston shaft, (2) commercial, off the shelf components, (3) serviceability and maintenance, (4) zero-field damping adjustment. The author

showed that this technology is feasible and meets the goal of providing a 'whole approach' MR solution and it is of simple construction. Carlson et al [26] applied MR dampers to smart prosthetics. The MR dampers, used as semi-acitive control devices, can provide the proper motion or locking of artificial knee based on the instantaneous action being carried out by users, so that the system adapted in real time to the users walking speed, stairs, slope of terrain, weight of the leg. Jolly[27] applied MR brake to pneumatic motion control so that robust and accurate motion control was achieved. Zhu, Bobb, and Ewins [28] developed a disk type MR fluid damper for rotor system vibration control. The disk-type MR damper is based on the shear operation mode and the magnetic field of the damper was analyzed by the finite element method. The effectiveness of the disk-type MR damper for attenuating vibration of rotor systems and of a simple open-loop on-off control based on the feedback of rotational speed on controlling vibration of rotor systems were experimentally studied.

The application of MR dampers as lead lag damper in helicopters was also conducted. We will discuss it in next section.

1.2 Ground Resonance

Ground resonance is a catastrophic aeromechanical instability that takes place when the helicopter is on the ground. It is an instability involving the low frequency cyclic lag motion of the rotor and the motion of the helicopter fuselage on its support, that is, landing gears or struts. The standard analysis of the ground resonance was developed by Coleman and Feingold[29]. In their analysis, an articulated four blade rotor was considered. It was shown that as rotor rotational

speed increase, the low frequency rotor lag frequency changes. Ground resonance can occur in rotational speed regions where the lag frequency coalesces with a landing support natural frequency. Aerodynamic forces do not play a significant role in this instability and can be neglected. As a matter of fact, this instability can occur in vacuum. Ground resonance is a very violent instability and must be avoided during the operation of the helicopter. Coleman's analysis though simple, gave a satisfactory prediction of the instability and was widely applied. Fundamental parametric investigations of the ground resonance phenomenon for articulated rotor helicopters were also conducted by Hooper[30] and Gabel[31].

For the soft in-plane hingless and bearingless rotors, ground and air resonance became major concerns. Aerodynamics and flapping motion can play important role in ground resonance. Therefore, the ground resonance model became more complex. Body pitch angle (α_x) and roll angle (α_y) as well as cyclic flap angles (β_{1c}, β_{1s}) are included in analysis[32, 33, 34]. In these cases, the aeromechanical instability was modeled as nonlinear aeroelastic problem rather than a linear mechanical instability problem. Lytwin and Miao[35] used the rigid-hinged blade representation with flap, lag, and torsion degrees of freedom to analyze air and ground resonance of soft in-plane hingeless rotor. Five degrees of freedom were included for rigid body motions: three translation, and body pitch and roll rotations. Quasi-steady aerodynamics was used. The conclusion that soft in-plane hingeless rotors can be designed to be free from unstable behavior was made. Donham et al (1969) studied the characteristics of ground and air resonance for a soft in-plane rigid-rotor system. The rotors were unstable when they were not operated at the normal RPM. It was shown that the ground resonance instability can be alleviated by the use of aerodynamic damping via pitch/flap coupling

and pitch/in-plane coupling[37]. Bousman[38] conducted testing of ground resonance stability for a model hingeless rotor. The model consisted of a soft in-plane rotor with flap-lag flexures and rigid blades, and the body with pitch and roll gimbal springs. Two configurations were considered: one matched stiffness, that is, non-rotating flap frequency equaled the lag frequency, and the other with the flap flexure much softer than the lag flexure. It was concluded that the matched stiffness rotor with negative pitch-lag coupling was able to stabilize the ground resonance. To improve the prediction of the instability, the dynamic inflow model to account for the influence of unsteady aerodynamic effects were included. Johnson[32] demonstrated the importance of dynamic inflow for hingeless rotor ground resonance. Friedmann and Venkatesan[40] analyzed the influence of various unsteady aerodynamic models on the aeromechanical stability of a hingeless rotor helicopter in ground resonance. It was concluded that the dynamic inflow models improved the correlation of the predicted results with the experimental results. Jang and Chopra[41, 42] examined the aeromechanical stability of a bearingless rotor helicopter in hover and forward flight by introducing the effects of fuselage motion in the finite element analysis. Kunz[43] developed complete, nonlinear equations to analyze the nonlinear effect of ground resonance. Both elastomeric blade and landing gear dampers were included in the mathematical model. The nonlinear analysis was performed using the method of multiple scales. The nonlinear analysis showed that the response amplitudes and the locations of the primary resonances depend on the number of blades in the rotor. Linear analysis alone can neither predict response amplitudes nor primary resonances other than those corresponding to the eigenvalues.

One of the major ways to prevent the ground resonance is to use lead-lag

dampers. The specialized high damping elastomeric dampers were developed as lead-lag dampers due to its advantages of no moving parts and ease of maintenance. The elastomeric dampers were widely applied to helicopter rotor blades and demonstrated their efficiency for rotor stabilization[45]. However, these dampers exhibit strange nonlinearity under single frequency excitation and dual frequency excitation[46]. Also, elastomeric damper characteristics are dependent on temperature[47]. These disadvantages cause difficulties in the analysis the properties of the dampers and their effect on aeromechanical and aeroelastic instabilities.

Besides using lead-lag dampers, several other ways to prevent ground resonance were developed. Nath[48] investigated using active constrained layer on rotorcraft flex beam to augment lead-lag damping and mitigate the ground and air resonance instabilities. The flex beam of hingeless and bearingless rotors, as a candidate structure for implementing active constrained layer damping, was modeled so that the open-loop transfer function from the piezo to beam states, as well as the sensitivity transfer function from the tip force to beams states, can be computed using this modeling approach. These transfer functions were in a useful form for single-input single-output feedback controller synthesis. Smith and Chopra[49] studied using elastically tailored composite rotor blades to prevent air and ground resonance. It was shown that elastic couplings introduced through tailored composite blade spars can have a powerful effect on both air and ground resonance behavior. Air resonance stability is diminished by elastic pitch-flap couplings in hover and forward flight. Negative pitch-lag elastic coupling has a stabilizing effect on the regressive lag mode in hover and forward flight. The negative pitch-lag coupling has a detrimental effect on ground res-

onance stability. Extension-torsion elastic coupling (blade pitch decreases due to tension) decreases regressive lag mode stability in both airborne and ground contact conditions. Zotto[50] investigated the effect of pitch-lag coupling on the damping requirement to stabilize the ground and air resonance. It was shown that for certain configurations, pitch-lag coupling can be used to reduce overall lag damping requirements. Gandhi and Hathaway[51] used formal optimization methods to determine a combination of aeroelastic coupling parameters that can alleviate ground resonance instability of a soft-in-plane rotor. It was found that negative pitch-lag coupling, positive pitch-flap coupling, flap flexibility outboard of pitch, and lag flexibility inboard of pitch were most beneficial. Liu et al[52] investigate the method that use a special type of smart materials, segmented constrained layer (SCL) damping, to improve rotor aeromechanical stability. In their research, the SCLs were bonded to the upper and lower surfaces of the box beam to provide passive damping. A classic ground resonance model and an air resonance model were used in the rotor-body coupled stability analysis. The Pitt dynamic inflow model was used in the air resonance analysis under hover condition. Results indicated that the surface bonded SCLs significantly increase rotor lead-lag regressive modal damping in the coupled rotor-body system.

Using feedback control to stabilize the aeromechanical instability of rotorcraft has been studied from 1984. In 1984, Straub[37] studied using active blade pitch control to increase helicopter rotor/body damping. In the study, the fuselage was modeled to have 4 degrees of freedom which are lateral and longitudinal displacement and pitch and roll motions, and each blade was modeled to have 2 degrees of freedom which are flap and lag motions. The flap/lag coupling was included in the analysis. The model was nonlinear and periodic with 4+2N

parameters where N is the number of blades. The model was linearized and Floquet analysis was used for periodic coefficients. The state feedback control system then developed for this model. Feedback parameters include cyclic rotor flap and lead-lag states, and body pitch and roll rotations. The use of position, rate, and acceleration feedback is studied for the various state variables. In particular, the influence of the closed-loop feedback gain and phase on system stability was investigated. It turned out that for the rotor/body configuration analyzed, rotor cyclic in-plane motion and body roll-rate and roll-acceleration feedback can considerably augment system damping levels and eliminate ground resonance instabilities. Scheduling of the feedback state, phase and gain with rotor rotation speed can be used to maximize the damping augmentation. This increase in lead-lag damping can be accomplished without altering any of the system modal frequencies. Also,the influence of rotor design parameters (hinge offset, blade precone, blade flapping stiffness) was assessed. It was pointed out that these rotor characteristics have significant influence on the active feedback control effectiveness. The higher the offset and stiff stiffness, the better the damping augmentation. So it was concluded that this kind of active control would be particularly powerful for hingeless and bearingless rotors. Gandhi and Weller [54] investigated using fuselage state feedback for aeromechanical stability augmentation. The study analytically investigates the influence of body pitch and roll position, velocity, and acceleration feedback on aeromechanical stability characteristics of a model bearingless rotor. It was shown that fuselage acceleration feedback was seen to have maximum benefit in alleviating ground resonance. The destabilizing trend with increasing collective pitch for the uncontrolled system can be alleviated by choosing an optimal controller phase at

higher collective pitch values. The feedback control scheme was effective in augmenting aeromechanical stability over a broad range of variations in rotor speed and collective pitch, and for variations in model configuration. Using moderate controller gains prevented instability of body modes at high rotational speeds, collective pitch values, or in the case of changes in body inertias. Hathaway[55] and Gandhi studied using individual blade control to mitigate the helicopter ground resonance. Individual Blade Control (IBC) through blade root pitch actuation in the rotating system, based on rotor state feedback, was developed. Formal optimization techniques are used on two different model rotors to determine a combination of controller gains, for each rotor, that will alleviate resonance over a broad range of conditions. It was shown that for both model rotors considered, IBC stabilized ground resonance over a wide range of rotational speeds and collective pitch values. The robustness of these IBC schemes was verified by their continued effectiveness in case of changes in fuselage inertia. It was concluded that IBC had a greater stabilizing effect on ground resonance than either aeroelastic couplings or active control through the swashplate based on fuselage state feedback. The optimized Individual Blade Control used to alleviate ground resonance was found to improve aeromechanical stability in hover. Marathe et al[56] explored the feasibility of using MR dampers for lag damping augmentation in helicopters. The damper was modeled as Bingham-Plastic model which is a parallel combination of a viscous element and a friction element. The viscous element captured the post-yield domain and the friction element was dominant on the pre-yield behavior. The Coleman and Feingold model was used as rotor/fuselage model. The aerodynamic forces are ignored and all dampers are assumed linear and similar. The flap motions were added and the fuselage

motions were dropped for forward flight stability analysis. Damper was sized by assuming that 6% of linear damping was required to stabilize ground resonance instability. Two control schemes were developed. The first one was On/Off control. Two criteria are used to obtain equivalent linear damping for the nonlinear MR damper as a function of the size of perturbation and the applied field. Hub loads were computed for different advance ratios. It was shown that hub loads can be eliminated in forward flight if yield force on MR dampers is minimized. If some damping is required at very high advance ratio, magnetic field can be applied and stabilized the rotor, however, high hub loads were generated too. A more advanced scheme was developed to size the damper using feedback control scheme. The design objective was to change damping actuation and reduce the hub load using a feedback control. The control scheme was to be demonstrated to be very efficient. The On/Off control is straightforward and easy to implement but it is not optimal for reducing hub loads. Feedback control is more versatile but required more complexity due to sensors and feedback control system. Prasanth et al[57] applied the energy to peak control to ground resonance problem. Energy to peak control problem for LPV systems involves the design of a stabilizing controller that guarantees satisfaction of time domain L_∞ constraints for all bounded energy disturbances and admissible parameter trajectories. As an application, the ground resonance problem is rotorcraft is formulated as an energy to peak control problem. Then, an energy-to-peak controller scheduled with respect to RPM was designed. The approach offers a fast and economical means to develop LPV models and design active controllers for rotorcraft aeromechanical instabilities.

1.3 Damping Identification

1.3.1 Hilbert Transform

Hilbert transform is well known envelope detection method and is widely applied in signal processing and image processing. Its application in mechanical system was explored by many researchers.

Agneni[58] first applied Hilbert transform to damping coefficient estimation using time domain data. In his research, considerations on the possibility to regard as analytic the complex signal formed by the impulse response of a structure and its Hilbert transform were presented. Band pass filters were used to isolate the mode of interest from the impulse response of a structure and the results prove the effectiveness of the approach and the possibility to get significant results even when the relatively limited time windows are used and highly truncated signals are considered.

Feldman et al[59, 60, 61, 62, 63] applied the Hilbert transform for non-linear vibration system and non-stationary signals investigation. The techniques enable identification of non-linear system instantaneous modal parameters (natural frequency, damping characteristics and their dependencies on a vibration amplitude and frequency) during free vibration analysis and different kinds of dynamic system excitation. The proposed method of vibration analysis determines instantaneous modal parameters even if an input signal is a high sweep frequency quasi-harmonic signal or random signal. A method to separate and estimate varying absolute amplitudes and frequencies of double-component vibration signal is also proposed. For a multi-degrees of freedom system, when the frequency of excitation is close or equal to one of the undamped natural

frequencies, this mode shape is identical to the principal (normal) mode shape of the system. In this case vibration of the system depends only on parameters of this one particular normal mode and on excitation. Using a swept frequency excitation, the modal parameters of a corresponding normal mode shape can be estimated using Hilbert transform.

Kang[64] discussed using Hilbert transforms to identify the modal parameters by using a scanning Laser Doppler Vibrometer. In the paper, the Hilbert transform was a replacement of the Fourier transform based approach to avoid the leakage problem introduced by the discrete Fourier transform. To increase the processing efficiency, the Hilbert transform approach is extended to measure multi-mode shape data through a set of experimental procedure. The feasibility of this approach is illustrated along with results of numerical simulations.

Nagarajaiah[65] presented a new and innovative semi-active variable stiffness tuned mass damper (SAIVS-TMD) system. In the system, the Hilbert transform was used to estimate instantaneous frequency so that the system robust to changes in building stiffness and damping.

Huang[66] developed a new method for nonlinear and nonstationary time series analysis using Hilbert transform. It is well known that Hilbert transform can only be applied to single degree of freedom system. However, for some applications, the signal consists of multiple modes which are nonlinear and nonstationary. Huang developed a method called Empirical Mode Decomposition method, with which any complicated data set can be decomposed into a finite and often small number of Intrinsic Mode Functions (IMF). This decomposition method is adaptive, and, therefore, highly efficient. Since the decomposition is based on the local characteristic time scale of the data it is applicable to nonlin-

ear and nonstationary processes. With the Hilbert transform, the Intrinsic Mode Functions yield instantaneous frequencies as functions of time that give sharp identifications of embedded structures. Comparisons with Wavelet and window Fourier analysis show the new method offers much better temporal and frequency resolutions. This method is also called Hilbert-Huang transform. It has been applied to fatigue analysis of marine risers[67], machine fault diagnosis[68], identification of civil structures[69], and modal damping analysis[70].

1.3.2 Moving Block Method

Moving block technique is developed from short time Fourier transform, or windowed Fourier transform. It was applied in rotary wing aeroelastic stability testing in reference[71]. Hammond[72] applied the method to determine the subcritical damping and frequency during aeroelastic testing of flight vehicles. The author derived the basic formula of moving block method. Generally there are three steps to implement the moving block method. First is data acquisition and FFT analysis. The data is collected and the entire transient response is transformed into frequency domain so that the frequency of desired mode is determined. If the frequency resolution is not high enough to provide the accurate frequency of the mode of interesting, an optimization procedure[72] can be used so that the high frequency resolution can be reached. The second step is to choose a small block of data. The block is first positioned at the beginning of the record, then the spectral amplitude of a particular mode is calculated for this block. The block is then moved down the data record one data sample and this process is repeated till the end of data record is reached. Last, the damping in the mode being analyzed is estimated using the least square fit of the natural log of

the amplitude. Author also showed that the multimode response can be viewed as a summation of several single degree of freedom response, and the moving block technique effectively provided the means for isolating the various components of the response, so that the frequency and damping information for each of the modes can be calculated. Bousman and Winkler[73] discussed how to apply the moving block method in two modes. Several factors that influence the identification accuracy are discussed. Goertzels' algorithm and the use of variable block size were suggested to determine the analysis frequency accurately. Leakage is a major problem of the moving block technique. In this study, the author discussed how to reduce the leakage by using Hanning window and how tuning the block size can improve damping estimation. Tasker and Chopra[78, 79] derived a new recursive formulation which includes the Hanning window and used a moving block analysis to identify rotor stability characteristics, to overcome the difficulty that using window function would result in substantial increase in computational cost. Smith and Wereley[74] applied FFT based moving block to identify damping of composite rotorcraft flexbeams with viscoelastic damping layers. It was concluded that FFT based moving block method is not suitable for nonlinear damping identification due to the contradiction between the frequency resolution and damping estimation accuracy. The primary difficulty is that for accurate nonlinear damping estimates, a short moving block is needed, which results in poor frequency resolution. However, in a spectrally dense environment such as a helicopter rotor, high frequency resolution is necessary in order to differentiate between spectrally close modes. To overcome this difficulty, the moving block technique based on a periodic Fourier series decomposition was developed[75, 77]. Since the moving block analysis provides a quick damping

estimate for desired mode, it is widely used in helicopter industry[80, 81].

1.3.3 Wavelet Transform

The wavelet transform was developed in past two decades and was applied to signal processing and image processing. Wavelet analysis can be defined as an alternative to the classical windowed Fourier analysis. It is efficient for local analysis of nonstationary and fast transient signals. Similar to the short-time Fourier transform, Wigner distribution and ambiguity function, the wavelet transform is a mapping of the signal to the time-scale joint representation. The temporal aspect of the signals is preserved. The wavelet transform provides multiresolution analysis with dilated windows. The high frequency analysis is done using narrow windows and the low frequency analysis is done using wide windows. The wavelet transform is powerful for multiresolution local spectrum analysis of nonstationary signals, such as sound, radar, sonar, seismic, and electrocardiographic signals, and for image compression, image processing, and pattern recognition.

Application of wavelet transform to the structural system identification has been researched to improve the traditional methods. The determination of accurate structural models from measured response data remains a challenge to dynamics specialists. For traditional purposes, i.e., accurate experimental determination of structural vibration modes and mode shapes for design improvements of passive vibration suppression systems, the identification of the dominant and troublesome modes and mode shapes usually suffices. However, the development of the active vibration control and on line health monitoring required that an accurate in-situ determination of structural dynamics models far beyond the traditional modal testing and model determination. It may be necessary to obtain

a larger set of modes and mode shapes, and to construct the mass, damping and stiffness properties.

Robertson[84] researched the use of discrete wavelet transforms for the identification of structural dynamics models. In the paper, discrete temporal impulse response functions were first obtained from vibration records by the discrete wavelet transform (DWT). The functions were then used for system realizations and the structural modes, mode shapes and damping parameters were extracted from the realized state space model. The paper addressed that the present DWT-based structural system identification procedure is a serious alternative to the FFT-based procedure, and outperforms FFT methods for narrow frequency-band inputs. Lamarque[85] analyzed a damped signal recorded in physical basis with wavelet patterns optimally localized both in time and frequency domains and to extract "local" information to estimate the damping ratio. A wavelet based formula similar to the logarithmic decrement formula is introduced to estimate damping in multi-degree-of-freedom systems from time domain response. The formula then applied to identify the damping of in situ dynamic responses of a civil engineering building excited with both harmonic and shock testing.[86]

1.4 Research Objectives

The main purpose of this research is to assess the feasibility of using MR dampers to mitigate the aeromechanical instability of helicopter rotors. Although there is some literature on this research, they are limited and not fully explored[56]. The main advantage of using MR dampers is the adjustable damping of MR dampers can provide controllable damping to stabilize the ground resonance and to avoid

large damping forces when damping is not needed. There are two key objectives of this thesis. The first is to develop a control strategy to control MR dampers to supply current to stabilize the ground resonance. The second is to develop an algorithm to assess the damping levels of rotors which using MR dampers as lead-lag dampers from rotor stability test data. Thus, this thesis is concerned with stabilizing the ground resonance of helicopters using MR dampers. This research is divided into two parts.

In the first part, using MR dampers as lag dampers of helicopter is researched. The MR dampers are controlled using feedback control theory to stabilize the ground resonance. The damping level can be adjusted according to different damping requirement.

The objective of second part is to develop an accurate damping identification algorithm from the rotor stability test data to identify the lag damping when MR dampers are implemented. In the rotor stability test data, the damped lag response is often corrupted by the persistent excitation of 1/rev response. The damping estimation of lag response is difficult due to the 1/rev persistent excitation is often spectrally close to lag response and the amplitude of the 1/rev persistent excitation is often much lager than the lag response. The existing methods can not get the accurate damping identification of lag motion. A new damping identification algorithm is developed based on the existing methods and the characteristic of rotor stability test data.

1.4.1 Contribution of Present Work

(1) Using MR dampers as semi-active devices to stabilize the ground resonance of helicopter rotors is investagted. The feasibility of using MR dampers as lag

damper to mitigate the ground resonance is investigated first. Two ways of integrating MR dampers are introduced: Using linearized damping and using nonlinear model directly.

(2) Nonlinear control strategies are developed. The sliding mode control and the feedback linearization control strategies are used for the nonlinear properties of MR dampers and ground resonance problem. MR dampers, combined with the developed control strategies, are shown to be able to stabilize the ground resonance instability.

(3) The robustness of using MR dampers is investigated in two different ways: by considering the degradation of dampers and by considering parameter perturbations. For the first case, the linear time periodic model is developed and the Floquet theory is used for the stability analysis. For the second case, the parameters are perturbed and performance of the control algorithms are evaluated, so that the robustness of the control algorithms is assessed.

(4) A hybrid damping identification algorithm is developed. This algorithm can precisely estimate the lag damping from the rotor stability test data in which the lag damped response is corrupted by 1/rev persistent excitation. The development of this algorithm is based on the analysis of three existing methods: the Hilbert transform, the Fourier based moving block method, and the wavelet transform. The analysis of the three existing methods gets the conclusion that because the energy of the rotor stability test data is concentrate on 1/rev persistent excitation, and because the 1/rev signal and lag response is spectrally close, it is difficult to identify the lag damping directly from the data using existing method. Instead, the hybrid method try to filter out the 1/rev persistent excitation first, which makes the residual signal is lag response only, so that the

damping identification is simple and straight forward.

(5) The estimation of nonlinear damping characteristics of the system using ER/MR dampers is developed. The most used model for the ER/MR dampers is Bingham-Plastic model. In this model, the pre-yield property is modeled as Coulomb damping and the post-yield property is viscous damping. An algorithm to identify the Coulomb damping characteristic and viscous damping characteristic simultaneous from the transient response data is developed. The application of the algorithm on rotor stability test data is also investigated.

Chapter 2

Semi Active Damping of Helicopter Rotor Systems Using Magnetorhological Dampers

2.1 Introduction

In this chapter, we will research how to use MR damper to mitigate the ground resonance problem. Ground resonance is a dynamic instability caused by the coupling of the blade lag motion and the hub inplane motion. When happening, it will result in a catastrophe. To avoid this problem, enhancement of lag damping is a major design consideration. Tranditionally, hydraulic or elastomeric dampers are mounted in the hub to mitigate this instability. Mitigation of ground resonance is a critical and dominant factor when designing these lag dampers. However, the high levels of lag damping are only required for specific rotor operating conditions, such as those where ground resonance may occur. For other flight situations, high damping produces excessively large periodic damper loads because of periodic flap/lag/torsion blade motions. Moreover, the design of

elastomeric lag dampers is complicated by elastomeric material bulk properties being dependent on temperature, strain amplitude, and frequency [98, 114]. For these reasons, an attractive proposition is to utilize semi-active lag dampers that are capable of adjusting their damping levels in response to the rotor operational conditions, such as RPM, and temperature. In recent years, magnetorheological (MR) fluid based dampers have demonstrated the capability to offer damping levels comparable to fluid elastic dampers, while offering continuous control of damping level via changes in applied magnetic field [1, 107]. Thus, it is natural to introduce MR damping devices to provide the controllable lag damping, and enhance stability of the rotor in the face of ground resonance. In this chapter, we will explore the semi-active control of ground resonance in a helicopter because such a strategy may have a significant impact in improving the overall stability augmentation of the rotor. The objectives of this chapter are: (1) develop a methodology for the integration of the MR damper into a classic linear ground resonance analysis assuming an isotropic rotor hub (all dampers and blades similar) and an anisotropic rotor hub (due to lag damper dissimilarity due to damage, for example), (2) control to a stability margin, (3) stabilize an unstable rotor and augment the stability of a slightly stable rotor

2.2 Ground Resonance Model

The ground resonance model we used in this chapter is developed by Coleman and Feingold. This model though simple, is effective to predict and analyse the ground resonance problem. The model only considers lag motions of blades and longitudinal and lateral hub motions, which correspond to degrees of freedom

of helicopter fuselage on its landing gear. The diagram to show that how the four blades and fuselage or landing gear are linked and modeled is shown in Figure. The stiffness and damping of fuselage are represented by the effective parameters: $\bar{k_x}$, $\bar{k_y}$, $\bar{C_x}$, $\bar{C_y}$. Lag dampers are assumed similar and in this model they are considered to behave as linear viscous model, so that the damping moment can be written as:

$$\text{Damper Force } F_i = C\,\overset{\star}{\zeta_i} \;\text{ for } i = 1, 2, 3, 4$$

where i is the blade number. Later we will introduce the nonlinear damping force into this model.

In the rotating frame, the lag moment equilibrium at the lag hinge of each blade can be expressed as:

$$\overset{\star\star}{\zeta_i} + {\nu_\zeta}^2\zeta_i + \bar{C}\,\overset{\star}{\zeta_i} + \bar{S_\zeta}(\overset{\star\star}{x_h}\sin\psi_i - \overset{\star\star}{y_h}\cos\psi_i) = 0 \text{ for } i = 1, 2, 3, 4 \tag{2.1}$$

The aerodynamic forces are not considered since they are not important to ground resonance analysis.

Tranforming these equations from the rotating frame to the non-rotating frame using FCT for a 4-bladed rotor ($N_b = 4$), collective lag equation (in ζ_0), differential lag equation (in ζ_2) and two cyclic lag equations (in ζ_{1c} and ζ_{1s}) are obtained :

$$\overset{\star\star}{\zeta_o} + {\nu_\zeta}^2\zeta_0 + \bar{C}\,\overset{\star}{\zeta_o} = 0 \tag{2.2}$$

$$\overset{\star\star}{\zeta_2} + {\nu_\zeta}^2\zeta_2 + \bar{C}\,\overset{\star}{\zeta_2} = 0 \tag{2.3}$$

$$\overset{\star\star}{\zeta_{1c}} + \bar{C}\,\overset{\star}{\zeta_{1c}} + 2\,\overset{\star}{\zeta_{1s}} + ({\nu_\zeta}^2 - 1)\zeta_{1c} + \bar{C}\zeta_{1s} - \bar{S_\zeta}\,\overset{\star\star}{y_h} = 0 \tag{2.4}$$

$$\overset{\star\star}{\zeta_{1s}} + \bar{C}\,\overset{\star}{\zeta_{1s}} - 2\,\overset{\star}{\zeta_{1c}} + ({\nu_\zeta}^2 - 1)\zeta_{1s} - \bar{C}\zeta_{1c} - \bar{S_\zeta}\,\overset{\star\star}{x_h} = 0 \tag{2.5}$$

Note that, with assumptions made previously (isotropic hub and linear damping), Eqs. 2.2 and 2.3 are uncoupled to cyclic equations as well as fuselage motions and can be solved separately so that they are not considered any longer as a part of the system. Later we will consider the anisotropic hub and nonlinear damping, so that Eqs. 2.2 and 2.3 have to be added to the system.

The body equations (X and Y directions) are obtained by calculating the hub loads, applying Fourier Coordinate Transformation (FCT)[105], and finally non-dimensionalizing, to yield:

$$\overset{\star\star}{x}_h + \frac{1}{2}\frac{\bar{S}_\zeta}{\bar{M}_x}\overset{\star\star}{\zeta}_{1s} + \bar{C}_x \overset{\star}{x}_h + \frac{\omega_x^2}{\Omega^2}x_h = 0 \tag{2.6}$$

$$\overset{\star\star}{y}_h + \frac{1}{2}\frac{\bar{S}_\zeta}{\bar{M}_y}\overset{\star\star}{\zeta}_{1c} + \bar{C}_y \overset{\star}{y}_h + \frac{\omega_y^2}{\Omega^2}y_h = 0 \tag{2.7}$$

The non-dimensional expressions of inertia ($\bar{M}_x$,$\bar{M}_y$), support frequencies (ω_x,ω_y) and damping coefficients ($\bar{C}_x$,$\bar{C}_y$) of the fuselage are given at the end of this section in Table 2.1.

Eqs. 2.4, 2.5, 2.6, 2.7 can be summarized by the following linear matrix equation:

$$\begin{bmatrix} 1 & 0 & 0 & -\bar{S}_\zeta \\ 0 & 1 & \bar{S}_\zeta & 0 \\ 0 & \frac{1}{2}\frac{\bar{S}_\zeta}{\bar{M}_x} & 1 & 0 \\ -\frac{1}{2}\frac{\bar{S}_\zeta}{\bar{M}_y} & 0 & 0 & 1 \end{bmatrix} \begin{Bmatrix} \overset{\star\star}{\zeta}_{1c} \\ \overset{\star\star}{\zeta}_{1s} \\ \overset{\star\star}{x}_h \\ \overset{\star\star}{y}_h \end{Bmatrix} + \begin{bmatrix} \bar{C} & 2 & 0 & 0 \\ -2 & \bar{C} & 0 & 0 \\ 0 & 0 & \bar{C}_x & 0 \\ 0 & 0 & 0 & \bar{C}_y \end{bmatrix} \begin{Bmatrix} \overset{\star}{\zeta}_{1c} \\ \overset{\star}{\zeta}_{1s} \\ \overset{\star}{x}_h \\ \overset{\star}{y}_h \end{Bmatrix}$$

$$+ \begin{bmatrix} {\nu_\zeta}^2 - 1 & \bar{C} & 0 & 0 \\ -\bar{C} & {\nu_\zeta}^2 - 1 & 0 & 0 \\ 0 & 0 & \frac{\omega_x^2}{\Omega^2} & 0 \\ 0 & 0 & 0 & \frac{\omega_y^2}{\Omega^2} \end{bmatrix} \begin{Bmatrix} \zeta_{1c} \\ \zeta_{1s} \\ x_h \\ y_h \end{Bmatrix} = 0 \tag{2.8}$$

Figure 2.2 is the Coleman diagram or fan diagram and modal damping dia-

gram. The Coleman diagram shows the evolution of each mode frequency when increasing RPM. Modal damping diagram indicates the damping of each mode versus RPM. In the Coleman diagram, coalescences of the regressive mode with the longitudinal one, in the first time, and the lateral one, in a second time, can be clearly identified. One can notice that the regressive mode merges with the longitudinal fuselage mode then with the lateral fuselage mode. The first coalescence occurs for a range of RPM from $0.0466\Omega_0$ and $0.6\Omega_0$. The second one starts at $0.683\Omega_0$ and stops at Ω_0. This second instability is the dominant one since it occures over a wider range of RPM. Moreover, the modal damping plot shows that it generates a stronger instability. Indeed the regressive mode reaches a very high value of modal damping. Since the system does not present any damping, ground resonance leads to instability.

2.3 Magnetorheological Dampers

In recent years, MR dampers have demonstrated the capability to offer damping levels comparable to fluid elastic dampers, while offering continuous control of damping level via changes in applied magnetic field [1, 107]. MR fluid typically consists of micron-sized magnetically polarizable particles suspended in a carrier fluid such as silicon oil. Under magnetic field, particle chains are formed and the fluid becomes semi-solid and thus, exhibits visco-plastic behavior. By varying the magnetic field in the magnetorheological valve of the damper, the force response, and thus the damping, can be controlled. Magnetorheological dampers are typically modeled using an idealized Bingham-plastic model [113, 109]. When the force applied to the damper is below a threshold, called the yield force, F_y,

the damper is rigid. However, once the force applied to the damper exceeds the yield force, the damper behaves as a Newtonian or viscous damper offset by this yield force. The Bingham plastic model can be expressed as

$$\bar{F}(\overset{\star}{\zeta}) = \bar{F}_y \text{sign}\left(\overset{\star}{\zeta}\right) + \bar{C}_{po}\,\overset{\star}{\zeta} \tag{2.9}$$

where $\bar{F}_y$ is the nondimensional dynamic yield force and $\bar{C}_{po}$ is the post-yield damping. Here, the damping force F, and damping C, are nondimensionalized as follows:

$$\bar{F} = \frac{F}{I_b \Omega^2} \tag{2.10}$$

$$\bar{C}_{po} = \frac{C_{po}}{I_b \Omega} \tag{2.11}$$

A damper that follows this Bingham plastic behavior tends to exhibit a response with high frequency force jitter [106]. Piston bleed is often added to smoothen the response [106]. Therefore, to better model the damper response with piston bleed, a biviscous damper model will be used [20]. This model assumes: (1) in the pre-yield domain, the damper behaves as a linear viscous damper with a very high damping coefficient, $\bar{C}_{pr}$, and (2) in the post-yield domain, the post-yield damping, $\bar{C}_{po}$, drops substantially, so that $\bar{C}_{pr} > \bar{C}_{po}$. The biviscous damper can be expressed as

$$\bar{F}(\overset{\star}{\zeta}) = \begin{cases} \bar{C}_{po}\,\overset{\star}{\zeta} + \bar{F}_y & \overset{\star}{\zeta} \geq \overset{\star}{\zeta}_y \\ \bar{C}_{pr}\,\overset{\star}{\zeta} & -\overset{\star}{\zeta}_y \leq \overset{\star}{\zeta} \leq \overset{\star}{\zeta}_y \\ \bar{C}_{po}\,\overset{\star}{\zeta} - \bar{F}_y & \overset{\star}{\zeta} \leq -\overset{\star}{\zeta}_y \end{cases} \tag{2.12}$$

where the yield velocity, $\overset{\star}{\zeta}_y$, and the nondimensional preyield damping, $\bar{C}_{pr}$, are defined as:

$$\overset{\star}{\zeta}_y = \frac{\bar{F}_y}{\bar{C}_{pr} - \bar{C}_{po}} \tag{2.13}$$

$$\bar{C}_{pr} = \frac{C_{pr}}{I_b \Omega} \tag{2.14}$$

The three parameters of this model are the nondimensional pre-yield damping coefficient, $\bar{C}_{pr}$, the nondimensional post-yield damping coefficient, $\bar{C}_{po}$, and the nondimensional yield force, $\bar{F}_y$. Fig. 2.3 shows the yield force, $\bar{F}_y$ as a function of lag velocity $\overset{\star}{\zeta}$ for the biviscous MR damper model. Control of the damping level is provided by changing the yield force, $\bar{F}_y$, via the application of magnetic field. The yield force typically increases monotonically with magnetic field until the MR fluid reaches a condition of magnetic saturation, that is, increasing the magnetic field no longer increases the yield stress. In the absence of magnetic field, we will assume that the yield force is negligible, and that the damper behaves as a linear viscous damper with a damping, $\bar{C}_{po}$. The maximum value of yield force is limited by the saturation of the damper (increasing the magnetic field will not provide higher yield force).

2.4 Feasibility Analysis

In this section, we examine if it is feasible to use MR dampers to stabilize an unstable rotor in ground resonance. Feasibility means that we verify that the parameters of the MR dampers are in a proper range to stabilize the rotor, and that the sizing of the MR damper is suitable to be used in rotors. The analysis is made in the sense of energy dissipated by the MR dampers. The Coleman-Feingold ground resonance model is used directly by modeling the MR dampers as equivalent viscous (linearized) dampers.

2.4.1 Equivalent Viscous Damping

The MR damper model is introduced into the system using the equivalent viscous damping based on the energy dissipated over one cycle. For a sinusoidal damper excitation of amplitude, A_e, and frequency, Ω_e, the energy dissipated, E, over a cycle for the nonlinear biviscous damper is equal to:

$$E = \oint F(\psi) d\zeta = \int_0^{2\pi} F(\psi) \overset{\star}{\zeta}(\psi) d\psi \tag{2.15}$$

Equating this dissipated energy to that of an equivalent viscous damper leads to an expression for the equivalent viscous lag damping, $C_{\zeta,eq}$:

$$C_{\zeta,eq} = \frac{E}{\pi \Omega_e A_e^2} \tag{2.16}$$

Then the equivalent viscous damping is nondimensionalized as

$$\bar{C}_{\zeta,eq} = \frac{C_{\zeta,eq}}{I_b \Omega_e} = \frac{E}{\pi I_b \Omega_e^2 A_e^2} \tag{2.17}$$

From Eqns.(2.15), (2.16) and(2.17), the equivalent damping is a function of amplitude, A_e, as well as frequency of excitation Ω_e. The ground resonance frequency can be assumed to be near the rotating lag frequency ν_ζ [105], so that the rotor speed defines the frequency of the lag damper excitation and thus the frequency of linearization. Moreover, an amplitude of 3 deg of lag angle was chosen as the equilibrium lag angle when performing the linearization. From Eqn.(2.16), it can be seen that the higher the amplitude of perturbation, the lower the equivalent damping coefficient. If the stability of the system is demonstrated for the high lag perturbation selected (3 degrees in our case), this approach guarantees rotor stability for lower perturbations (due to the resulting higher damping coefficient). This equivalent damping technique is applied using the biviscous damper model.

2.4.2 Stability Analysis

In this first example, an unstable rotor is considered where the objective is to stabilize the rotor system. Rotor and fuselage characteristics are given in Table 2.1. The damping coefficients are: $\bar{C}_x$=0.1450, $\bar{C}_y$=0.1664 and $\bar{C}_{po}$=0.05 at the operational rotor speed Ω_0. The support damping coefficients correspond to the typical values found in [102]. The post-yield coefficient of the MR damper is a low value of lag damping coefficient, so that the rotor/fuselage system has an unstable ground resonance. Using the isotropic rotor stability analysis, we calculated the Coleman diagram and the modal damping diagram (Fig. 2.4).

Fig. 2.4 presents the Coleman diagram and the modal damping of the system with the characteristics given above, and when the yield force in the MR dampers is zero (no damper actuation). The system is unstable when the relative RPM is between 0.48 and 1.03. Indeed, the low frequency mode coalesces with the longitudinal and lateral fuselage modes and its relative modal damping (here, defined as the opposite sign of real part of the eigenvalue divided by RPM) reaches a negative value. These instabilities are generated by the lack of lag damping in the system. Each coalescence leads to a minimum relative modal damping of the low frequency mode. These minimums correspond to the degree of instability reached by the system for each coalescence. In Fig. 2.4, the first coalescence is labeled as Point A, and Point B is used to quantify the second coalescence. The ordinates of A and B are will be used to characterize the stability margin of the system, and the stability margin at points A and B are very dependent on the damping included into the lag direction.

From this unstable rotor system, the MR damper parameters ($\bar{F}_y$ and $\bar{C}_{po}/\bar{C}_{pr}$) are varied in order to investigate their impact on system stability. Fig. 2.5 shows

the result of this analysis. The minimum relative modal damping (ordinate of points A and B) reached by the low frequency rotor mode during each coalescence is plotted versus the yield force $\bar{F}_y$. It can be seen that increasing the yield force generates a overall increase of the rotor stability. Indeed, the minimum relative modal damping of both coalescences increase as $\bar{F}_y$ grows. The response of coalescences A and B are similar qualitatively to an increase in yield force. The plots related to the both coalescences exhibit a specific trend. For low $\bar{F}_y$, the rotor is stabilized with higher yield force. For large $\bar{F}_y$ (>0.016), varying the yield force does not change the stability of the system. For these high values of $\bar{F}_y$, the MR damper is acting in the high viscosity pre-yield domain only, so that the yield force does not influence the MR damper performance. That explains the two distinct parts in Fig. 2.5. The stability analysis was done for values of $\bar{C}_{po}/\bar{C}_{pr} = 1/8$, 1/10 and 1/12. These values correspond to typical value of MR dampers with biviscous behavior [106, 107]. The stability of the system is not affected by the value of the damping coefficient ratio. It shows that the key factor in controlling the rotor damping is the yield force and the performance of the MR damping augmentation strategy is not affected by the damping coefficient $\bar{C}_{po}/\bar{C}_{pr}$.

From Fig. 2.5, we conclude that this unstable rotor/fuselage system can be stabilized by the introduction of MR dampers. These dampers met the following nondimensional requirements: $\bar{C}_{po} = 0.05$, $\bar{C}_{po}/\bar{C}_{pr} = 1/8$, maximum yield force $\bar{F}_y = 0.006$. These values are dimensionalized, as shown in Table 2.2, in order to compare requirements above with actual MR damper performance and thus ensure feasibility of the application. The distance between the damper attachment points, R_1, as shown in Fig. 2.1, is required to perform the dimensionalization.

Using a biviscous model, the yield force that must be developed by the MR damper can be computed [114], and the results are shown in Table 2.3 for different values of the distance between the damper attachment point. A value of $R_1 = 1.5ft$ is a practical value that requires a yield force of $3,158$ lbs illustrating that the MR damper is a feasible preliminary option.

The stabilization of ground resonance phenomena appears to be feasible using physically motivated biviscous MR dampers according to these results. It was demonstrated that this instability requires a high amount of damping over the specific RPM range where modal coalescence occurs. Control laws will now be developed to take advantage of MR damper adaptability. The goal of these controllers will be to adjust the damping in the rotor in order to prevent ground resonance, but also to avoid over-damping at low and high RPM (which generates high hub loads). A simple and robust open loop control strategy, On-Off control, will be utilized in the next section. The scheduled output of the controller is damper yield force as a function of RPM. Feedback control strategies will be developed in the following section.

2.4.3 On-Off Control Strategy

The On-Off control strategy allows MR dampers to be in two states: state On where maximum field is applied and the MR damper is actuated at its full capacity, and Off where field is absent and the MR damper has zero yield force. The On-Off control strategy is as follows: (1) specify the lowest acceptable stability margin denoted as the design stability margin, (2) calculate the zero field stability margin as a function of RPM, (3a) if the zero field stability margin is lower than the design stability margin, then the controller turns all MR dampers on for

this value of RPM, else (3b),the dampers remain Off for this value of RPM, (4) repeat for the desired RPM range. This strategy is applied to the unstable rotor characterized in Fig. 2.1. For low and high RPM, the rotor is stable (no coalescence) therefore no actuation is required and MR dampers are Off. But during coalescence of rotor modes with fuselage modes, MR dampers are turned On to increase the overall damping in the rotor thereby mitigating ground resonance. The modal damping diagram of the rotor system with the On-Off strategy implemented is given in Fig. 2.6. The controlled rotor system is no longer unstable and the relative modal damping is always higher than the specified stability margin of 0.01.

2.5 Advanced Nonlinear Control Strategy

Though the simple On-Off control works well, there still exist some problems. The equivalent viscous damping is an approximate representation of the nonlinear MR damper, which cannot accurately represent the nonlinear field dependent behavior of MR dampers. To more accurately assess the effects of MR dampers on ground resonance, it is preferable to apply the MR damper model directly to the ground resonance model. Due to the high nonlinearity of the MR model, nonlinear analysis and nonlinear control design methods are needed. Furthermore, On-Off control law is a conservative control strategy. From Fig. 2.6, we can see that it is not necessary to turn the MR dampers fully On at all unstable rotor RPM values. A feedback control law is needed to exploit the MR damper's varying damping ability.

Since we apply the MR damper model directly to the ground resonance analy-

sis, the resulting model is different from the Coleman and Feingold model. The damping forces are incorporated into the model as control input. Because the damping forces are functions of the lag angle velocity in the rotating frame, the collective and differential modes in the fixed frame are no longer decoupled. All six degrees of freedom are considered in the model.

$$[M]\left\{\overset{\star\star}{q}\right\} + [C]\left\{\overset{\star}{q}\right\} + [K]\{q\} + [D(\psi)]\{\bar{u}\} = 0 \tag{2.18}$$

where

$$[M] = \begin{bmatrix} 1 & 0 & 0 & 0 & 0 & 0 \\ 0 & 1 & 0 & 0 & 0 & 0 \\ 0 & 0 & 1 & 0 & 0 & -\bar{S}_\zeta \\ 0 & 0 & 0 & 1 & \bar{S}_\zeta & 0 \\ 0 & 0 & 0 & \frac{1}{2}\frac{\bar{S}_\zeta}{\bar{M}_x} & 1 & 0 \\ 0 & 0 & -\frac{1}{2}\frac{\bar{S}_\zeta}{\bar{M}_y} & 0 & 0 & 1 \end{bmatrix}$$

$$[C] = \begin{bmatrix} 0 & 0 & 0 & 0 & 0 & 0 \\ 0 & 0 & 0 & 0 & 0 & 0 \\ 0 & 0 & 0 & 2 & 0 & 0 \\ 0 & 0 & -2 & 0 & 0 & 0 \\ 0 & 0 & 0 & 0 & \bar{C}_x & 0 \\ 0 & 0 & 0 & 0 & 0 & \bar{C}_y \end{bmatrix}$$

$$
[K] = \begin{bmatrix} {\nu_\zeta}^2 & 0 & 0 & 0 & 0 & 0 \\ 0 & {\nu_\zeta}^2 & 0 & 0 & 0 & 0 \\ 0 & 0 & {\nu_\zeta}^2 - 1 & 0 & 0 & 0 \\ 0 & 0 & 0 & {\nu_\zeta}^2 - 1 & 0 & 0 \\ 0 & 0 & 0 & 0 & \frac{\omega_x^2}{\Omega^2} & 0 \\ 0 & 0 & 0 & 0 & 0 & \frac{\omega_y^2}{\Omega^2} \end{bmatrix}
$$

The matrices $[M]$, $[C]$, and $[K]$ are time invariant. However the control distribution matrix, $[D(\psi)]$,

$$
[D(\psi)] = \begin{bmatrix} \frac{1}{4} & \frac{1}{4} & \frac{1}{4} & \frac{1}{4} \\ -\frac{1}{4} & \frac{1}{4} & -\frac{1}{4} & \frac{1}{4} \\ \frac{1}{2}cos(\psi) & -\frac{1}{2}sin(\psi) & -\frac{1}{2}cos(\psi) & \frac{1}{2}sin(\psi) \\ \frac{1}{2}sin(\psi) & \frac{1}{2}cos(\psi) & -\frac{1}{2}sin(\psi) & -\frac{1}{2}cos(\psi) \\ 0 & 0 & 0 & 0 \\ 0 & 0 & 0 & 0 \end{bmatrix}
$$

is time periodic(Appendix A). The state vector and control vector are given as

$$
\begin{aligned} \{q\}^t &= \{\zeta_0, \zeta_2, \zeta_{1c}, \zeta_{1s}, x_h, y_h\} \\ \{\bar{u}\}^t &= \left\{ \bar{F}_1(\overset{\star}{\zeta}_{(1)}), \bar{F}_2(\overset{\star}{\zeta}_{(2)}), \bar{F}_3(\overset{\star}{\zeta}_{(3)}), \bar{F}_4(\overset{\star}{\zeta}_{(4)}) \right\} \end{aligned}
$$

$\bar{F}_i(\overset{\star}{\zeta}_{(i)})$ for i=1,2,3,4, is the nondimensional damping force on each blade, which is highly nonlinear.

2.5.1 Controller Design

Since Eqn. (7.20) is a nonlinear model, nonlinear control design methods will be used to design the control law for the MR dampers.

Feedback Linearization Control

Feedback linearization is an approach to nonlinear control design which has attracted a great deal of research interest in recent years. The central idea of the approach is to algebraically transform a nonlinear system dynamic into a linear one, so that linear control techniques can be applied. The differs entirely from conventional linearization in that feedback linearization is achieved by exact state transformations and feedback, rather than by linear approximations of the dynamics [116].

Consider the last term of the Eqn. (7.20). If we let

$$\{\bar{u}\} = [Q]\,\{\bar{v}\} \tag{2.19}$$

where

$$[Q] \quad = \quad \begin{bmatrix} 1 & -1 & cos(\psi) & sin(\psi) \\ 1 & 1 & -sin(\psi) & cos(\psi) \\ 1 & -1 & -cos(\psi) & -sin(\psi) \\ 1 & 1 & sin(\psi) & -cos(\psi) \end{bmatrix}$$

and

$$\{\bar{v}\}^t = \{\bar{v_1}, \bar{v_2}, \bar{v_3}, \bar{v_4}\} \tag{2.20}$$

are control inputs to be designed then, we have

$$[D]\{\bar{u}\} = [D][Q]\{\bar{v}\} = \begin{bmatrix} I_{4\times 4} \\ --- \\ O_{2\times 4} \end{bmatrix} \{\bar{v}\} = \{\bar{V}\} \tag{2.21}$$

Substitute Eqn. (2.21) into Eqn. (7.20), we have

$$[M]\left\{\overset{\star\star}{q}\right\} + [C]\left\{\overset{\star}{q}\right\} + [K]\{q\} + \{\bar{V}\} = 0 \tag{2.22}$$

Eqn. (2.22) is now a linear model with control input to be designed. We can apply linear control design techniques such as LQR, pole placement, or output feedback to stabilize the rotor. Comparing Eqn. (2.22) with Eqn. (7.20), the periodic control distribution matrix and nonlinear damping forces have been linearized, greatly simplifying the controller design problem.

However, since linear control algorithms are formulated on the basis of active type actuators, the designed control law cannot be directly applied to the MR damper system. Therefore, in general, a secondary control law in Eqn. (2.23) must be superimposed on the controller which is designed to satisfy the semi-active condition as below [24]

$$\bar{F}_i(\overset{\star}{\zeta}_{(i)}) = \begin{cases} \bar{F}_i(\overset{\star}{\zeta}_{(i)}) & \text{if} \quad \bar{F}_i(\overset{\star}{\zeta}_{(i)})\,\overset{\star}{\zeta}_{(i)} > 0 \\ 0 & \text{if} \quad \bar{F}_i(\overset{\star}{\zeta}_{(i)})\,\overset{\star}{\zeta}_{(i)} \leq 0 \end{cases} \qquad \forall i \in 1,2,3,4 \tag{2.23}$$

Note that the introduction of the secondary control law will deteriorate the control performance. A more elegant way is to design a semi-active control law directly, so that the designed controller satisfies the semi-active constraint

$\bar{F}_i(\overset{\star}{\zeta}_{(i)})\ \overset{\star}{\zeta}_{(i)} > 0$ automatically, so that its behavior is like velocity feedback. To satisfy the semi-active condition implicitly, we use output feedback:

$$\{\bar{v}\} = [P]\,\{z\} \tag{2.24}$$

where

$$\begin{aligned}
[P] &= \begin{bmatrix} 0 & 0 & \bar{c} & 0 & 0 & 0 \\ 0 & 0 & 0 & \bar{c} & 0 & 0 \\ 0 & \bar{c} & 0 & 0 & \bar{c} & 0 \\ -\bar{c} & 0 & 0 & 0 & 0 & \bar{c} \end{bmatrix} \\
\{z\}^t &= \left\{ \begin{array}{cccccc} \zeta_{1c} & \zeta_{1s} & \overset{\star}{\zeta}_o & \overset{\star}{\zeta}_2 & \overset{\star}{\zeta}_{1c} & \overset{\star}{\zeta}_{1s} \end{array} \right\}
\end{aligned}$$

$\bar{c}$ is the control gain and is constrained so that $\bar{c} \geq 0$, and is called the damping constant. Also, z are those states selected for output feedback.

After closing the feedback loop, the system can be expressed as:

$$[M]\left\{\overset{\star\star}{q}\right\} + ([C] + [C_u])\left\{\overset{\star}{q}\right\} + ([K] + [K_u])\,\{q\} = 0 \tag{2.25}$$

where

$$[C_u] = \begin{bmatrix} \bar{c} & 0 & 0 & 0 & 0 & 0 \\ 0 & \bar{c} & 0 & 0 & 0 & 0 \\ 0 & 0 & \bar{c} & 0 & 0 & 0 \\ 0 & 0 & 0 & \bar{c} & 0 & 0 \\ 0 & 0 & 0 & 0 & 0 & 0 \\ 0 & 0 & 0 & 0 & 0 & 0 \end{bmatrix}$$

$$[K_u] \;=\; \begin{bmatrix} 0 & 0 & 0 & 0 & 0 & 0 \\ 0 & 0 & 0 & 0 & 0 & 0 \\ 0 & 0 & 0 & \bar{c} & 0 & 0 \\ 0 & 0 & -\bar{c} & 0 & 0 & 0 \\ 0 & 0 & 0 & 0 & 0 & 0 \\ 0 & 0 & 0 & 0 & 0 & 0 \end{bmatrix}$$

The control input, Eqn. (2.24), is like velocity feedback, which increases damping in the system. From Eqn. (2.28) we can see that the feedback control law indeed increases the damping. Choose $\bar{c}$ large enough, and the system will have sufficient damping, and be stabilized.

Using the control law in Eqn. (2.24), the semi-active condition does not need to be imposed explicitly because the constraint $\bar{F}_i(\overset{\star}{\zeta}_{(i)})\,\overset{\star}{\zeta}_{(i)} > 0$ is always satisfied implicitly. To prove this, substitute Eqn. (2.24) into Eqn. (2.19), so that

$$\begin{Bmatrix} \bar{F}_1(\overset{\star}{\zeta}_{(1)}) \\ \bar{F}_2(\overset{\star}{\zeta}_{(2)}) \\ \bar{F}_3(\overset{\star}{\zeta}_{(3)}) \\ \bar{F}_4(\overset{\star}{\zeta}_{(4)}) \end{Bmatrix} = [Q]\,[P] \begin{Bmatrix} \zeta_{1c} \\ \zeta_{1s} \\ \overset{\star}{\zeta}_o \\ \overset{\star}{\zeta}_2 \\ \overset{\star}{\zeta}_{1c} \\ \overset{\star}{\zeta}_{1s} \end{Bmatrix} = \bar{c} \begin{Bmatrix} \overset{\star}{\zeta}_{(1)} \\ \overset{\star}{\zeta}_{(2)} \\ \overset{\star}{\zeta}_{(3)} \\ \overset{\star}{\zeta}_{(4)} \end{Bmatrix} \tag{2.26}$$

The damping constant $\bar{c}$ is greater than or equal to zero, so the $\bar{F}_i(\overset{\star}{\zeta}_{(i)})$, i $= 1, 2, 3, 4$, always have the same sign as $\overset{\star}{\zeta}_{(i)}$, i $= 1, 2, 3, 4$. Then,

$$\bar{F}_i(\overset{\star}{\zeta}_{(i)})\,\overset{\star}{\zeta}_{(i)} = \bar{c}\,\overset{\star}{\zeta}{}^2_{(i)} \geq 0 \qquad \forall \mathrm{i} \in 1, 2, 3, 4 \tag{2.27}$$

Finally, the closed loop system reaches to the following equation:

$$[M_c]\left\{\overset{\star\star}{q}\right\} + ([C_c])\left\{\overset{\star}{q}\right\} + ([K_c]\{q\} = 0 \tag{2.28}$$

where

$$[M_c] = [M]$$

$$[C_c] = \begin{bmatrix} \bar{c} & 0 & 0 & 0 & 0 & 0 \\ 0 & \bar{c} & 0 & 0 & 0 & 0 \\ 0 & 0 & \bar{c} & 2 & 0 & 0 \\ 0 & 0 & -2 & \bar{c} & 0 & 0 \\ 0 & 0 & 0 & 0 & \bar{C}_x & 0 \\ 0 & 0 & 0 & 0 & 0 & \bar{C}_y \end{bmatrix}$$

$$[K_c] = \begin{bmatrix} {\nu_\zeta}^2 & 0 & 0 & 0 & 0 & 0 \\ 0 & {\nu_\zeta}^2 & 0 & 0 & 0 & 0 \\ 0 & 0 & {\nu_\zeta}^2 - 1 & \bar{c} & 0 & 0 \\ 0 & 0 & \bar{c} & {\nu_\zeta}^2 - 1 & 0 & 0 \\ 0 & 0 & 0 & 0 & \frac{\omega_x^2}{\Omega^2} & 0 \\ 0 & 0 & 0 & 0 & 0 & \frac{\omega_y^2}{\Omega^2} \end{bmatrix}$$

This closed loop model is same as Coleman and Feingold model except that in this model the control gain $\bar{c}$ can be controlled. According to Coleman and Feingold 's results and other previous research results, the ground resonance can be stabilized by choosing $\bar{c}$ large enough. This is the reason that damping augamentation of lag motion can stabilize the ground resonance. The stability criteria is called Deutsch Stability Criteria[105], which is:

For longitudinal mode:

$$\bar{c}\bar{C}_x > \frac{(1-\nu_\zeta)}{4\nu_\zeta}\left(\frac{\omega_x}{\Omega}\right)^2 \frac{S_\zeta^2}{\bar{M}_x} \tag{2.29}$$

For lateral mode

$$\bar{c}\bar{C}_y > \frac{(1-\nu_\zeta)}{4\nu_\zeta}\left(\frac{\omega_y}{\Omega}\right)^2 \frac{S_\zeta^2}{\bar{M}_y} \tag{2.30}$$

Hence, by choosing $\bar{c}$ large enought, the stability of the rotor system is guaranteed.

The damping constant $\bar{c}$ must vary with the RPM, so that the damping force can be increased at the ground resonance conditions, and reduced when there is no danger of ground resonance. The algorithm to choose $\bar{c}$ is the following for each RPM: (1) set $\bar{c} = \bar{C}_{po}$, calculate the stability margin of the system, (2) if the stability margin of the system is less than the minimum stability margin, then find the $\bar{c}$ that increases the stability margin of the system to the minimum stability margin, (3) else return $\bar{c} = \bar{C}_{po}$. The following cost function, J, is created to numerically generate the controller algorithm:

$$J = \begin{cases} 0 & if \quad SM_{system} > SM_{min} \\ SM_{min} - SM_{system} & if \quad SM_{system} \leq SM_{min} \end{cases} \tag{2.31}$$

where SM_{system} is the stability margin of the system and SM_{min} is the minimum design stability margin. Note that SM_{system} is a function of RPM as well as yield force applied on MR dampers. Thus the cost function, J, is also a function of RPM and $\bar{c}$. For each RPM, a Matlab equation solver is used to fine tune the appropriate value of damping constant $\bar{c}$ that sets J to zero.

Sliding Mode Control Strategy

$$[M]\left\{\overset{\star\star}{q}\right\}+[C]\left\{\overset{\star}{q}\right\}+[K]\{q\}=-[D]\{\bar{u}\} \tag{2.32}$$

The sliding surface is defined by

$$\{S\}=[G]\left(\frac{d}{d\psi}+\lambda\right)\{e\} \tag{2.33}$$

where $[G]\in R^{4\times 6}$ is the sliding surface gradient, $\{e\}=\{q\}-\{q_d\}$ is the error, and $\{q_d\}$ is the desired value. In this study, because the control target is to suppress the vibration, $\{q_d\}=\{0\}$. λ is a positive constant.

We can formulate SMC as follows

$$\begin{aligned}\{\bar{u}\} &= ([G][M]^{-1}[D])^{-1}\Big(-[G][M]^{-1}[C]\left\{\overset{\star}{q}\right\} \\ &\quad -[G][M]^{-1}[K]\{q\}+\lambda[G]\left\{\overset{\star}{q}\right\}+\phi_g\frac{\{S\}}{||\{S\}||}\Big)\end{aligned} \tag{2.34}$$

where $\left([G][M]^{-1}[D]\right)$ is nonsingular, and $\phi_g>0$.

System stability with the controller in Eqn. (2.34) is proven as follows. The Lyapunov function is given by

$$V=\frac{1}{2}\{S\}^T\{S\} \tag{2.35}$$

Then we have

$$\begin{aligned}\overset{\star}{V} &= \{S\}^T\left\{\overset{\star}{S}\right\} \\ &= -\{S\}^T[G][M]^{-1}\left([D]\{\bar{u}\}+[C]\left\{\overset{\star}{q}\right\}+[K]\{q\}-\lambda[G]\left\{\overset{\star}{q}\right\}\right) \\ &= -\phi_g||\{S\}||<0\end{aligned} \tag{2.36}$$

So the sliding condition is satisfied and the system is stable.

It is noted that in practice, it is not desirable to use the discontinuous control input in Eqn.(2.34) because of chattering. Therefore, we may replace $\frac{S}{||S||}$ in Eqn.(2.34) with an appropriate boundary layer width of ϵ [117, 118].

To make the controller semi-active, the secondary controller in Eqn. (2.23) must be combined with the SMC controller. This secondary controller ensures the force is always dissipative [24]. However, the secondary controller may deteriorate the stability.

2.5.2 Stabilization of an unstable rotor

To demonstrate performance of the proposed control strategies, we apply these control strategies to the unstable rotor from section 4. In the absence of MR damper control, i.e., when all MR damper are in the Off state or at zero yield force state, the rotor system is unstable when $\Omega/\Omega_0 > 0.4$. When the rotor speed reaches about 0.8/rev (point B in Fig. 2.4), the rotor reaches the most unstable state. The control strategies are applied to the MR dampers so that the damping of the rotor is increased. The results are shown in Fig. 2.7 to Fig. 2.14. Since the closed loop system is linear when using feedback linearization control, we can show the modal frequency and modal damping as well as time response. But the closed loop system is still nonlinear when using sliding mode control, so only time response results are shown.

The results of using the feedback linearization controller and the sliding mode controller are shown in Fig. 2.7, Fig. 2.9, Fig. 2.10, Fig. 2.11, and Fig. 2.12. The figures show the time response of the collective lag angle, ζ_0, cyclic lag angle, ζ_{1c}, and lateral hub motion, y_h respectively at point B in Fig. 2.4, the most

unstable point. The results for the differential lag angle, ζ_2, cyclic lag angle, ζ_{1s}, and longitudinal hub motion, x_h are similar to the results of ζ_0, ζ_{1c}, and y_h respectively, so that they are not shown.

Both the sliding mode controller and the feedback linearization controller stabilized the rotor system very well. The time responses of the lag angle and the hub motion are well damped and the vibration is suppressed quickly. The control inputs on the first blade using the two proposed controller are shown in Fig. 2.13. We can see that the control input of the feedback linearization controller is continuous, however, the control input of the sliding mode control is not. The reason is that the feedback linearization control satisfies the semi-ative condition automatically, but for the sliding mode control, the semi-active condition needs to be superimposed on the control law, which cut off some control effort, so that the control input is discontinuous, and reaches the saturation value at the first several control steps. The discontinuous control input causes a minor low frequency chattering in the response of the collective lag angle, which is shown in Fig. 2.7. Also, the control effort of the sliding mode control is larger than that of the feedback linearization control. But the advantage is that with the large control effort, the transient of cyclic response and the hub response are quickly suppressed (Fig. 2.9, Fig. 2.10, Fig. 2.11, and Fig. 2.12). Moreover, the figure also shows that the MR damper's varying damping capability is exploited. Compared to the On-Off strategy, the MR dampers are not fully turned on thereby conserving power. The control strategies cause the MR dampers to provide only the damping needed to stabilize the rotor.

The feedback linearization control strategy also results in the modal damping diagram of Fig. 2.14. The modal damping of the low frequency mode is

controlled when dampers are actuated; the stability margin is maintained at the constant value. The feedback linearization control provides the optimal damping to maintain the stability margin.

2.5.3 Augment Stability of a Stable Rotor

In the last section we stabilized an unstable rotor system using MR lag dampers. In this section, we consider another scenario: the baseline open loop rotor system is stable, but the stability margin specification is not met. We use the same rotor as which in last section. We increases the $\bar{C}_{po}$ of the MR dampers, so that when the MR dampers are off, the rotor is stable. The MR dampers are controlled to augment the stability of the rotor system so that the desired stability margin is satisfied.

Fig. 2.15 shows the modal damping of the baseline stable rotor. We can see at the rotor speed point B, the low frequency mode is almost undamped. For this kind of system, the system is marginally stable and a slight disturbance may destabilize the system. We need to increase the stability to make the system safe and reach a certain desired stability margin. The MR dampers are controlled with sliding mode control and the feedback linearization control to augment the stability of the baseline rotor system.

Fig. 2.16 shows the time responses of cyclic lag angle, ζ_{1c}, corresponding to point B in Fig. 2.15, for open loop system, the system using MR dampers controlled by sliding mode control, and the system using feedback linearization to control MR dampers respectively. In this motion for the open loop system, the lightly damped low frequency mode is dominant. Both the two control strategies suppressed the vibration and have comparable results. The response

is well damped and approaches to zero quickly. The response of the cyclic lag angle ζ_{1s} has a similar result except it is phase shifted.

Fig. 2.17 shows the time responses of collective lag angle ζ_0 corresponding to point B in Fig. 2.15, for open loop, sliding mode control, and feedback linearization to control MR dampers, respectively. Because the collective mode is well damped in the open loop system, the time response of the collective motion does not vibrate much. But anyway the proposed controllers increased damping of the system and the vibration in response of collective lag angle is suppressed. The response of the differential lag angle is similar.

Fig. 2.18 shows the time responses of the lateral hub motion. Similar to the cyclic angle response, the slightly damped low frequency mode is dominant in this lateral hub response for the open loop system, which makes the response vibrate strongly. Again, both of the proposed controllers work very well: the response of the closed loop system is well damped and the vibration is quickly suppressed.

Table 2.1: Rotor and fuselage characteristics (using uniform blades assumption)

Dimensionalized form	Value
Number of blades, N_b	4
Rotor Radius, R	$18.5 ft$
Operationnal rotor speed, Ω_0	$31.42\ rad/s$ (300 RPM)
Blade mass, M_b	$6.5\ slugs$
Blade mass moment, S_b	$65.0\ slug - ft$
Blade mass moment of inertia, I_b	$800.0\ slug - ft^2$
Lag hinge offset, e	$1.0\ ft$
Lag spring, k_ζ	$0.0\ ft - lb/rad$
Hub mass, M_x	$550.0\ slugs$
Hub mass, M_y	$225.0\ slugs$
Hub spring, k_x	$85000.0\ lb/ft$
Hub spring, k_y	$85000.0\ lb/ft$
Fuselage support frequency, $\omega_x = \sqrt{\frac{k_x}{M_x + N_b M_b}}$	$12.148\ rad/s$
Fuselage support frequency, $\omega_y = \sqrt{\frac{k_y}{M_y + N_b M_b}}$	$18.402\ rad/s$
Nondimensionalized form	**Value**
Blade first mass moment, $\bar{S}_\zeta = RS_b/I_b$	1.5
Blade lag frequency, $\nu_\zeta = \sqrt{e\frac{S_b}{I_b} + \frac{k_\zeta}{I_b \Omega^2}}$	$0.285/rev$
Fuselage inertia, $\bar{M}_x = \frac{(M_x + N_b M_b)R^2}{N_b I_b}$	68.175
Fuselage inertia, $\bar{M}_y = \frac{(M_y + N_b M_b)R^2}{N_b I_b}$	29.708

Table 2.2: Damping constants for MR lag damper

Quantity	Nondimensional	Dimensional
C_{po}	0.05	1256 [ft-lb-sec/rad]
C_{pr}	0.4	10048 [ft-lb-sec/rad]
C_{po}/C_{pr}	1/8	1/8

Table 2.3: MR damper yield force and stroke

R_1 [ft]	1	1.5	2
Maximum yield force, F_{ymax} [lbs]	4737	3158	2369
Damper stroke [mils]	91	138	182

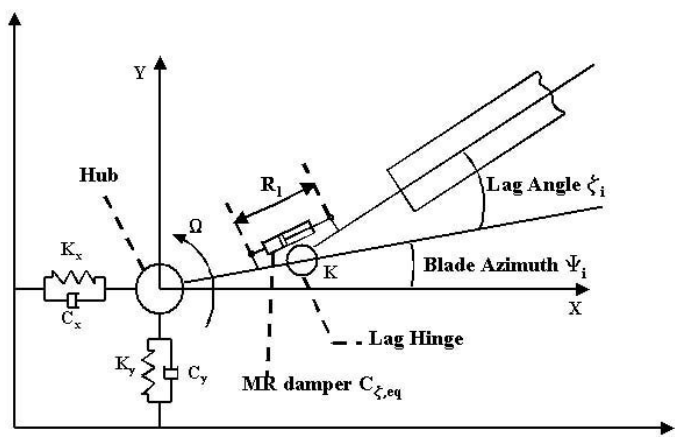

Figure 2.1: Schematic of the rotor/hub system

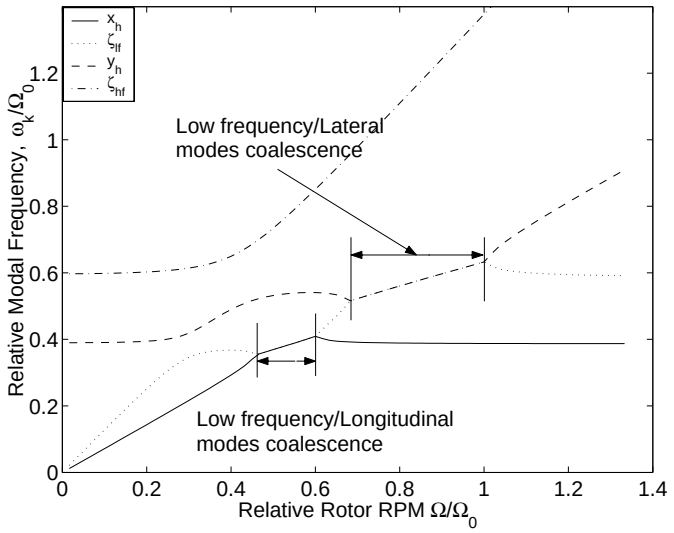

(a) Coleman diagram

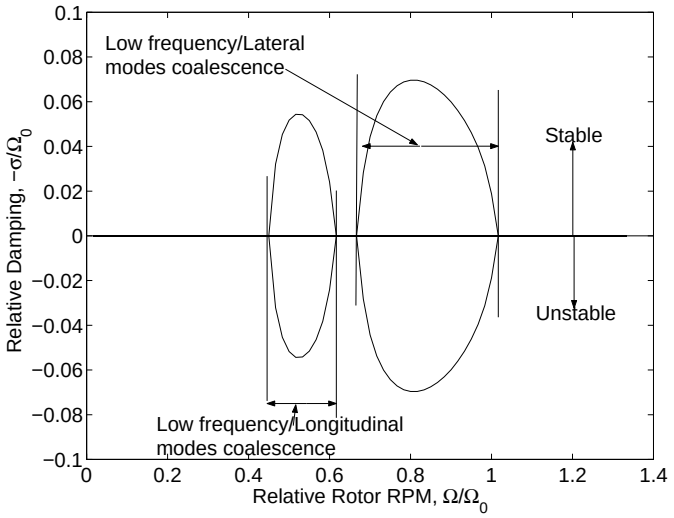

(b) Modal damping diagram

Figure 2.2: Coleman and modal damping diagram for an undamped rotor system

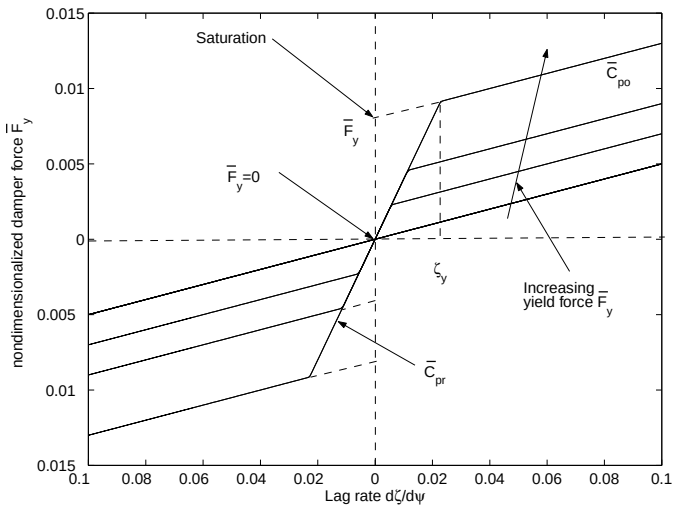

Figure 2.3: Biviscous damper model

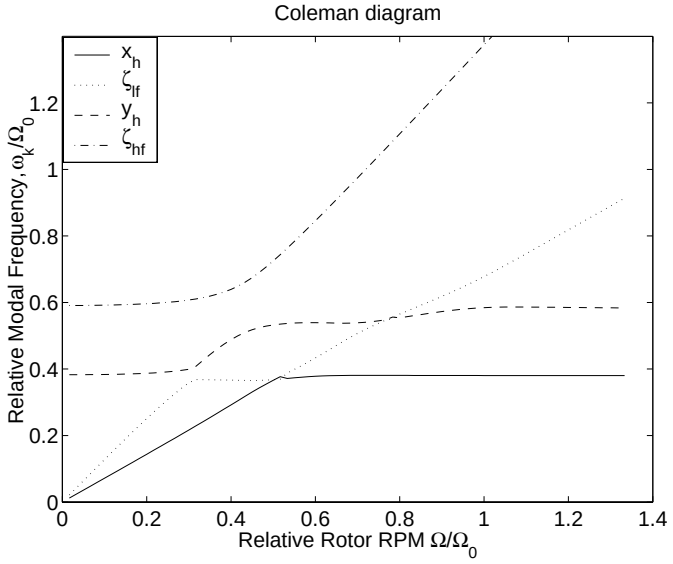

(a) Coleman diagram

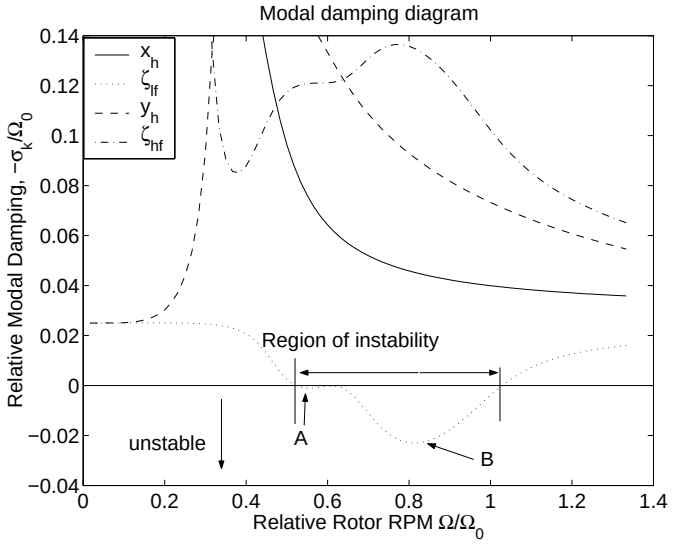

(b) Modal damping diagram

Figure 2.4: Coleman and modal damping diagram of the baseline unstable system

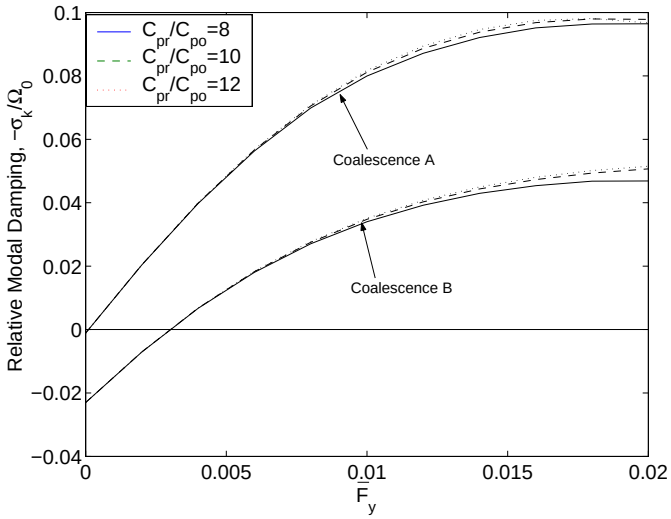

Figure 2.5: Effect of yield force $\bar{F}_y$ on modal damping

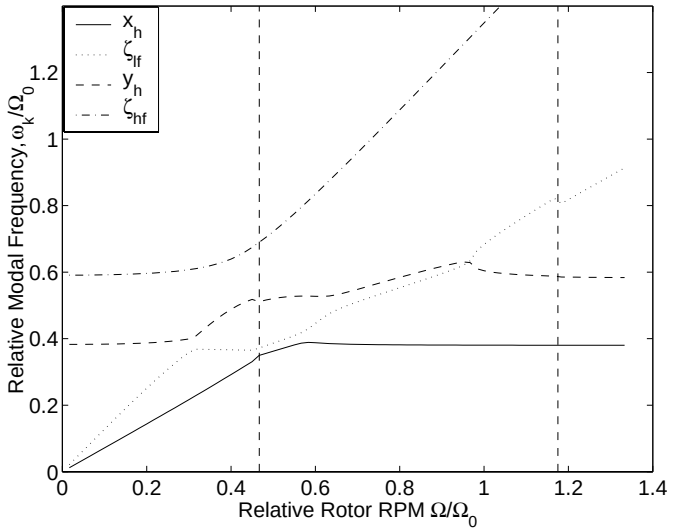

(a) Coleman diagram

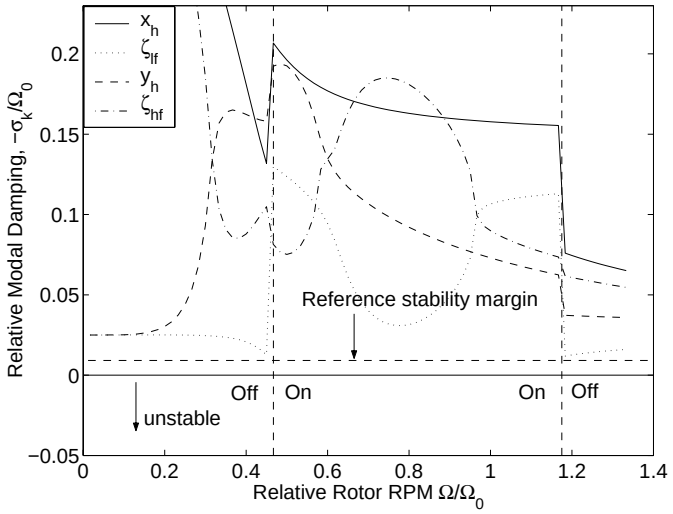

(b) Modal damping diagram

Figure 2.6: Coleman and modal damping diagram of the rotor system by applying On-Off control

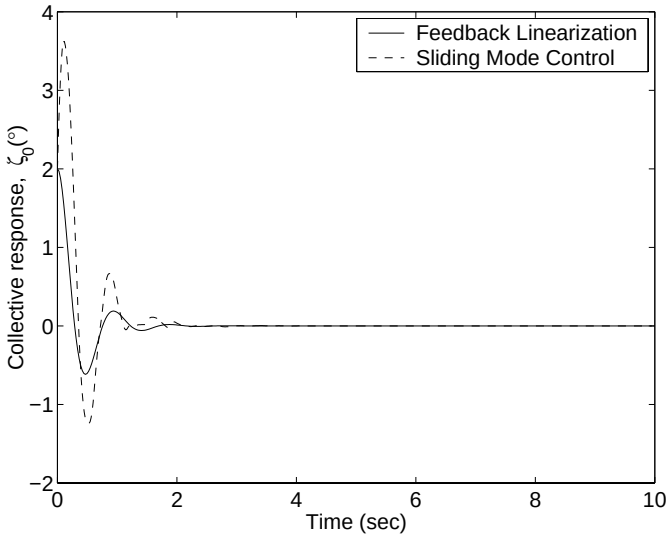

Figure 2.7: The collective lag response with sliding mode control and feedback linearization control

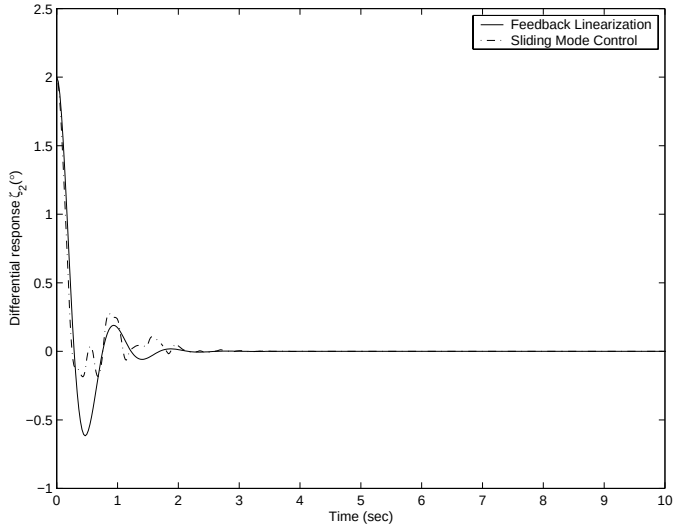

Figure 2.8: The differential lag response with sliding mode control and feedback linearization control

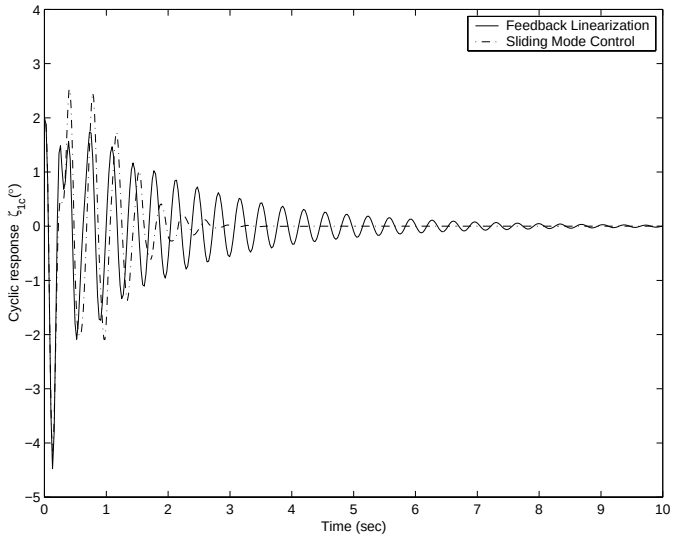

Figure 2.9: The lateral cyclic lag response with sliding mode control and feedback linearization control

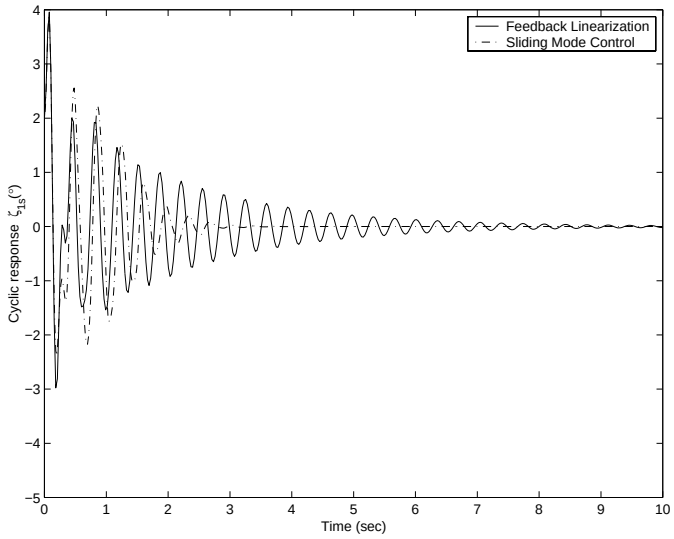

Figure 2.10: The longitudinal cyclic lag response with sliding mode control and feedback linearization control

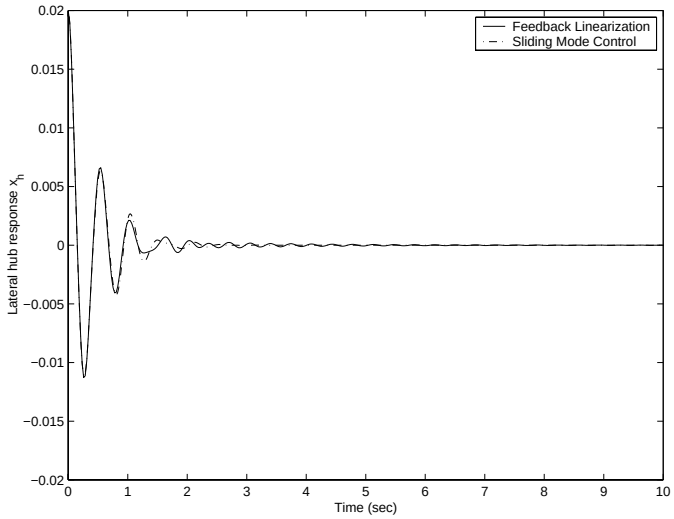

Figure 2.11: The lateral hub response with sliding mode control and feedback linearization control

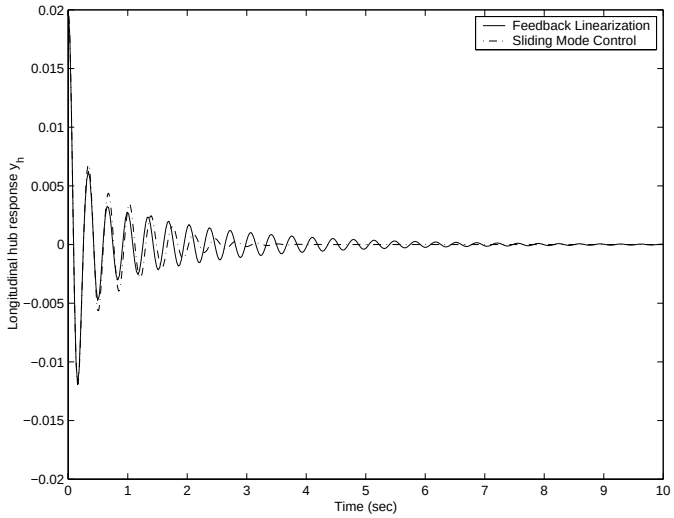

Figure 2.12: The longitudinal hub response with sliding mode control and feedback linearization control

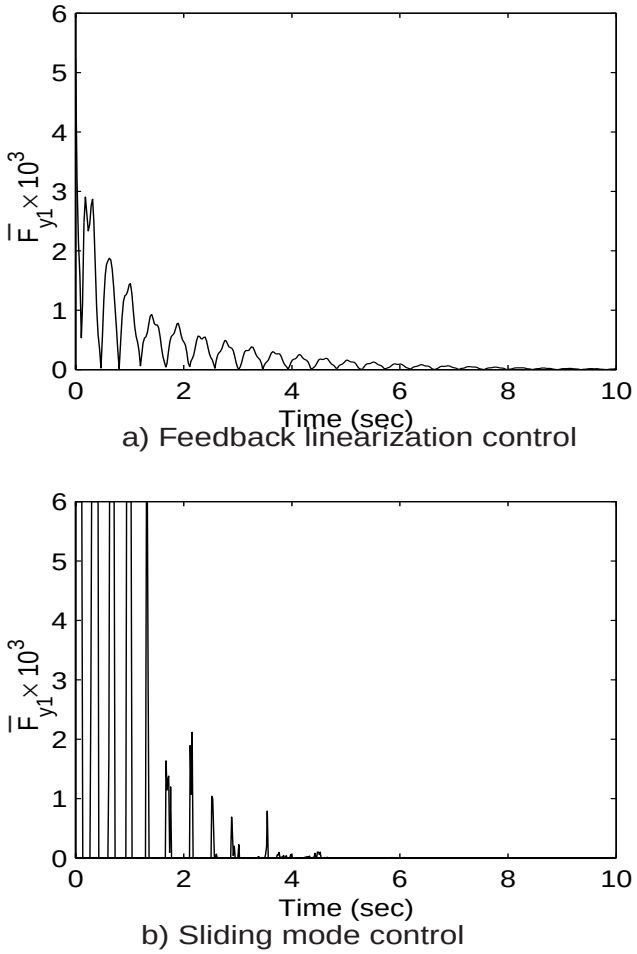

Figure 2.13: The nondimensional yield force on the first blade

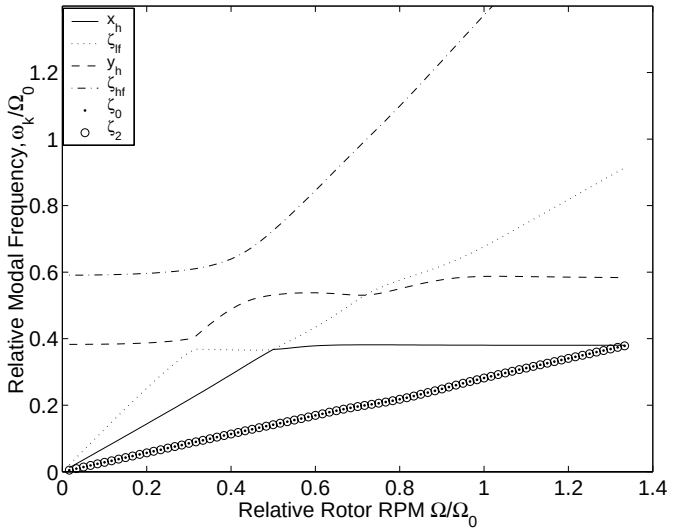

(a) Coleman diagram

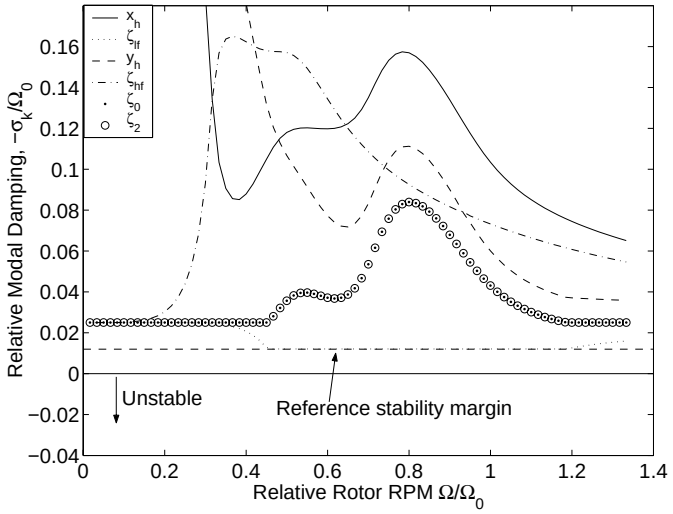

(b) Modal damping diagram

Figure 2.14: Coleman diagram and modal damping diagram of rotor system using feedback linearization strategy

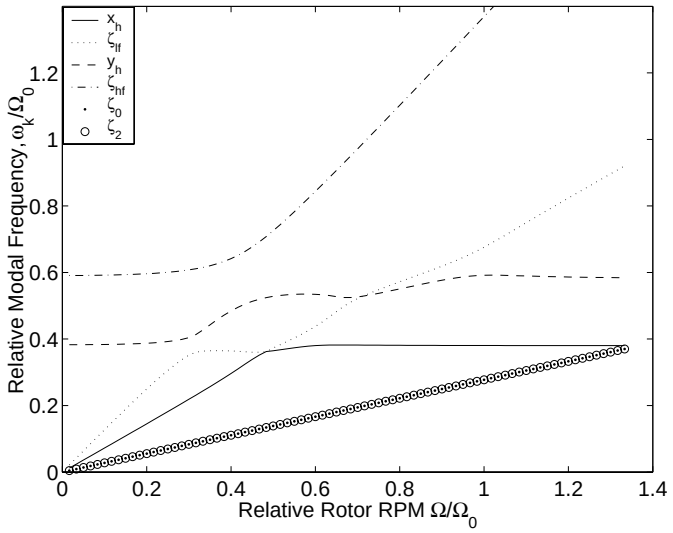

(a) Coleman diagram

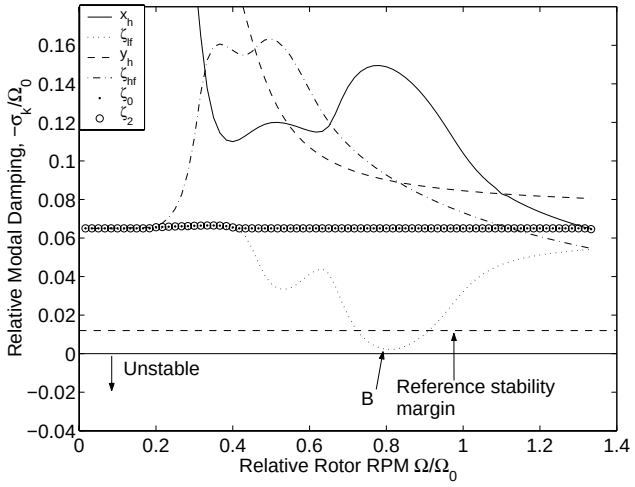

(b) Modal damping diagram

Figure 2.15: Coleman and modal damping diagram of the baseline stable rotor for stability augmentation

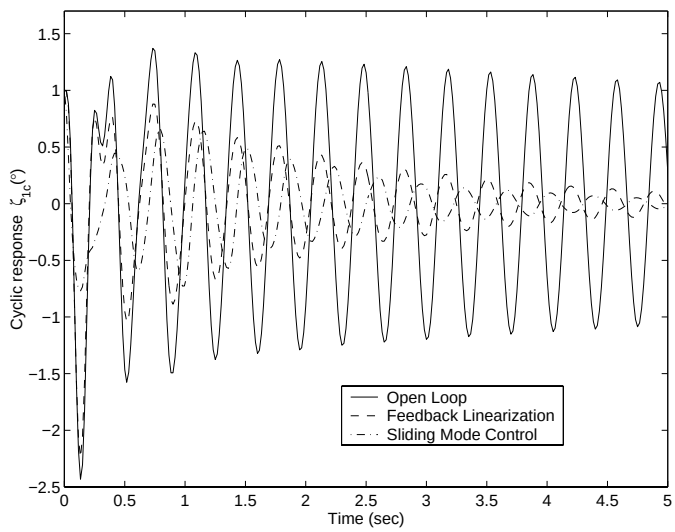

Figure 2.16: Result of damping augmentation: cyclic response

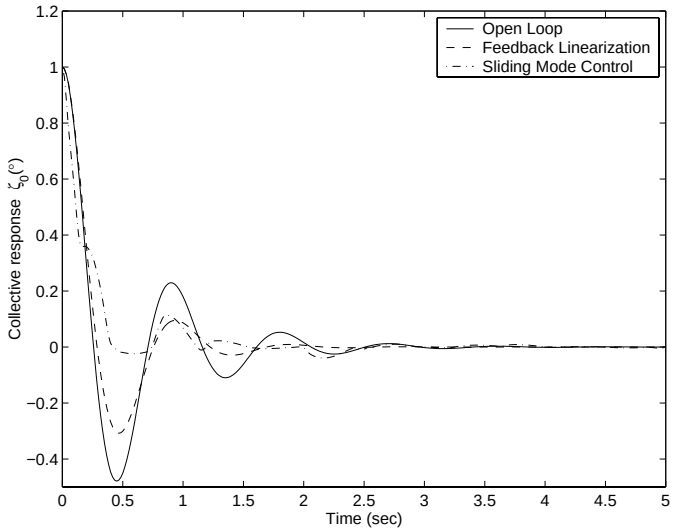

Figure 2.17: Result of damping augmentation: collective response

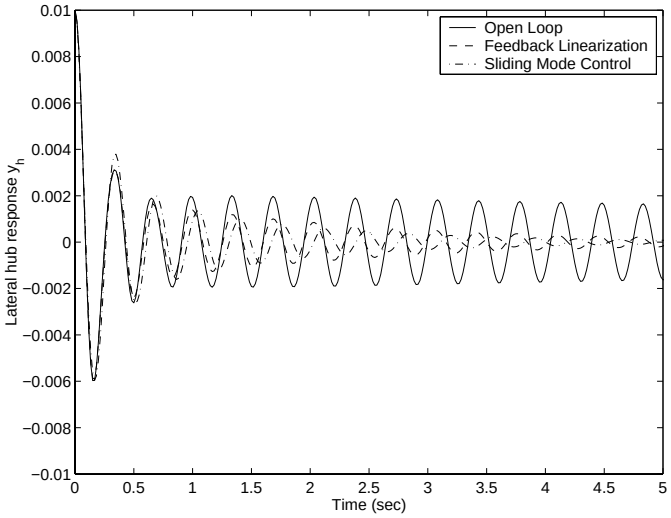

Figure 2.18: Result of damping augmentation: lateral hub response

Chapter 3

Robustness to Damper Degradation

In the previous chapter, we stabilized an unstable rotor system using MR lag dampers. Clearly, a rotor that was inherently passively unstable to ground resonance in the absence of applied field to the MR dampers is undesirable because of the catastrophic consequences of this instability. If, for any reasons, power to the MR dampers is lost, stability margins could not be maintained. Let us consider another MR damper application.

We consider a stable rotor when all lag dampers are fully operational and MR dampers are Off, where we assume two lag dampers per blade. Damper degradations are assumed to occur in the system, which can lead to an unstable rotor. MR dampers are activated to recover stability. In this section, we will consider only the feedback linearization controller, because, unlike in the case of sliding mode control, modal damping diagrams can be computed. This study assumes three cases of damping degradation and for each of them, the benefits of MR dampers are investigated. The three cases are: (1) one blade losses 50% of its lag damping, (2) one blade is assumed to lose all the damping, and (3) two blades lose 50% of their damping (with consideration of the symmetric and

asymmetric cases).

3.1 Dissimilar Dampers and Anisotropic Rotor Model

In the case of dissimilar dampers on each blade, the underlying physical model changes. In order to assess stability robustness, we apply the same feedback linearization strategy as in the previous section in the absence of failure. This leads to an anisotropic rotor model, which is a time periodic linear model, as the equations described below:

$$[M]\left\{\overset{\star\star}{q}\right\} + [C(\psi)]\left\{\overset{\star}{q}\right\} + [K(\psi)]\{q\} = 0 \tag{3.1}$$

where the damping matrix $[C]$ and the stiffness matrix $[K]$ are periodic with a period of 2π. Matrices $[C]$, and $[K]$ have the following expressions:

$$[C(\psi)] = \begin{bmatrix} C_{11} & C_{12} & C_{13}(\psi) & C_{14}(\psi) & 0 & 0 \\ C_{21} & C_{22} & C_{23}(\psi) & C_{24}(\psi) & 0 & 0 \\ C_{31}(\psi) & C_{32}(\psi) & C_{33}(\psi) & C_{34}(\psi) & 0 & 0 \\ C_{41}(\psi) & C_{42}(\psi) & C_{43}(\psi) & C_{44}(\psi) & 0 & 0 \\ 0 & 0 & 0 & 0 & \bar{C}_x & 0 \\ 0 & 0 & 0 & 0 & 0 & \bar{C}_y \end{bmatrix} \tag{3.2}$$

The coefficients of the matrix C are:

$$
\begin{aligned}
C_{11} &= \frac{1}{4}\sum_{i=1}^{4}\bar{c}_i \\
C_{21} &= C_{12} = \frac{1}{4}\sum_{i=1}^{4}(-1)^i\bar{c}_i \\
C_{22} &= \frac{1}{4}\sum_{i=1}^{4}(-1)^{2i}\bar{c}_i \\
C_{13}(\psi) &= \frac{1}{2}C_{31}(\psi) = \frac{1}{4}\sum_{i=1}^{4}\bar{c}_i\cos\psi_i \\
C_{23}(\psi) &= \frac{1}{2}C_{32}(\psi) = \frac{1}{4}\sum_{i=1}^{4}(-1)^i\bar{c}_i\cos\psi_i \\
C_{14}(\psi) &= \frac{1}{2}C_{41}(\psi) = \frac{1}{4}\sum_{i=1}^{4}\bar{c}_i\sin\psi_i \\
C_{24}(\psi) &= \frac{1}{2}C_{42}(\psi) = \frac{1}{4}\sum_{i=1}^{4}(-1)^i\bar{c}_i\sin\psi_i \\
C_{33}(\psi) &= \frac{2}{4}\sum_{i=1}^{4}\bar{c}_i\cos^2\psi_i \\
C_{34}(\psi) &= C_{43} = \frac{2}{4}\sum_{i=1}^{4}\bar{c}_i\cos\psi_i\sin\psi_i \\
C_{44}(\psi) &= \frac{2}{4}\sum_{i=1}^{4}\bar{c}_i\sin^2\psi_i
\end{aligned}
\tag{3.3}
$$

$$
K(\psi) = \begin{bmatrix}
\nu_\zeta^2 & 0 & K_{13}(\psi) & K_{14}(\psi) & 0 & 0 \\
0 & \nu_\zeta^2 & K_{23}(\psi) & K_{24}(\psi) & 0 & 0 \\
0 & 0 & K_{33}(\psi) & K_{34}(\psi) & 0 & 0 \\
0 & 0 & K_{43}(\psi) & K_{44}(\psi) & 0 & 0 \\
0 & 0 & 0 & 0 & \frac{\omega_x^2}{\Omega^2} & 0 \\
0 & 0 & 0 & 0 & 0 & \frac{\omega_y^2}{\Omega^2}
\end{bmatrix}
\tag{3.4}
$$

The coefficients of the matrix K are:

$$
\begin{aligned}
K_{13}(\psi) &= -\frac{1}{4}\sum_{i=1}^{4}\bar{c}_i \sin\psi_i \\
K_{14}(\psi) &= \frac{1}{4}\sum_{i=1}^{4}\bar{c}_i \cos\psi_i \\
K_{23}(\psi) &= -\frac{1}{4}\sum_{i=1}^{4}(-1)^i\bar{c}_i \sin\psi_i \\
K_{24}(\psi) &= \frac{1}{4}\sum_{i=1}^{4}(-1)^i\bar{c}_i \cos\psi_i \\
K_{33}(\psi) &= \nu_\zeta^2 - 1 - \frac{2}{4}\sum_{i=1}^{4}\bar{c}_i \sin\psi_i \cos\psi_i \\
K_{34}(\psi) &= \frac{2}{4}\sum_{i=1}^{4}\bar{c}_i \cos^2\psi_i \\
K_{43}(\psi) &= -\frac{2}{4}\sum_{i=1}^{4}\bar{c}_i \sin^2\psi_i \\
K_{44}(\psi) &= \nu_\zeta^2 - 1 + \frac{2}{4}\sum_{i=1}^{4}\bar{c}_i \cos\psi_i \sin\psi_i
\end{aligned}
\tag{3.5}
$$

In the equations, the damping on blade i is represented by the equation below:

$$
\bar{c}_i = \begin{cases}
\bar{c} & \text{if} \quad \text{No} \quad \text{damper} \quad \text{degradation} \\
0.5\bar{c} & \text{if} \quad 50\% \quad \text{damping} \quad \text{lost} \\
0 & \text{if} \quad 100\% \quad \text{damping} \quad \text{lost}
\end{cases}
\tag{3.6}
$$

Because the analysis needs to support different lag damping coefficients for each blade (assumption of a anisotropic rotor), all results will be computed using this anisotropic rotor model. Since the model is a linear time periodic model, the Floquet theory is used for modal frequency and modal damping analysis[102]. A state vector with 6 components is required for the analysis and, therefore, the

collective and differential rotor modes are added to other system modes in the following modal damping diagrams.

Fig. 3.1 characterizes the rotor/fuselage system which will support the present study. Fuselage and rotor properties are taken from Table 2.1. Fuselage damping coefficients are still set to $\bar{C}_x = 0.1450$ and $\bar{C}_y = 0.1664$ at the operational rotor speed Ω_0. The post-yield damping coefficient is assumed to be $\bar{C}_{po} = 0.15$, so that the rotor/fuselage system is stable and has similar damping levels in the rotor and the fuselage. The Coleman diagram and modal damping diagram in Fig. 3.1 demonstrate that the system is stable because coalescences do not generate positive values of modal damping. This figure considers the rotor to be isotropic (no damper damage has yet occurred) and therefore collective, ζ_0, and differential, ζ_2, modes are uncoupled from other system modes (constant modal damping versus RPM).

3.2 50% Damping Lost on One Blade

The previous rotor is now assumed to have lost 50% of the damping on one blade or one damper of the two mounted on one blade is inoperative. This assumption is transferred into the analysis by halving the damper force of the blade with the damaged damper. The Coleman diagram and the modal damping diagram of this damaged system is shown in Fig. 3.2. The stability margin of the system decreases during each coalescence. However, both coalescences do not correspond to system instability (modal damping always below zero). In a general sense, losing half of the lag damping on one blade tends to destabilize the rotor, however, it remains stable in ground resonance.

MR dampers are now activated with the goal of increasing the stability of the system to recover stability margins comparable to the undamaged rotor. The damping constant $\bar{C}$ applied by the damaged MR damper is half that applied on the others. An increase of the damping constant in the MR damper allows to introduce more damping into the rotor/fuselage system and thus to increase the stability of the system.

The feedback linearization strategy described in previous section is used to control the yield force of MR damper. Targets of the controller are the stability margins of the undamaged system. The modal damping diagram of the system is given in Fig. 3.3. The modal damping of the low frequency mode is only controlled during coalescences. It allows to keep it constant at the desired value. The MR damper actuation also generates an decrease of modal damping of all system modes coupled. Regaining of stability margin lost because of the deficient damper is possible via MR dampers.

3.3 100% Damping Lost on One Blade

More severe damage is now considered. Indeed, the second case assumes that both lag dampers on a single blade are fully inoperative. The modal damping diagram of such a system is given in Figure 3.5. Due to the lack of damping in a blade, the low frequency mode has almost zero damping. This mode exhibits three resonances over the RPM range considered. First and second coalescence (Point A and B) can be identified. The third resonance (Point C) occurs at lower RPM than two previous ones. Coalescences of low frequency/lateral modes and low frequency/longitudinal modes provoke instability of the low frequency mode

during the second coalescence.

A time analysis was carried out to identify the nature of resonance B and C. It showed that Point B is originated by a standard resonance of the low frequency mode and the longitudinal fuselage mode. Thus, it is a standard ground resonance instability due to a lack of damping in the system. The time analysis at the RPM of Point C reveals that all the blades and fuselages motions are well damped, except for the blade with the inoperative damper. Hence, it was concluded that this resonance is a pure blade motion resonance due to the undamped blade.

Effects of MR damper on the differential mode are shown in Fig. 3.6. Increasing of damping force is very efficient at stabilizing the first coalescence (Point A). Whereas the second coalescence sees its maximum modal damping decreases by a small amounts but not enough to regain the stability of the system. The system remains unstable, even with the increased damping using MR dampers.

3.4 50% Damping Lost on Two Blades

Finally, the third case of the study assumes a 50% loss of damping at two locations in the four bladed rotor. Two configurations can be considered: the symmetric configuration where the blades with deficient dampers are 180° out of phase at opposite locations, and the asymmetric where the dampers are 90° out of phase.

Fig. 3.7 is the modal damping diagram of the system with two dampers inoperative at 50% in the symmetric configuration. Due to the rotor symmetry, collective and differential modes are uncoupled with other system modes. The

stability margin is well reduced compared to the undamaged rotor and the damping is insufficient to prevent the rotor/fuselage system from instability during the second coalescence. This instability is mild but it could be catastrophic and thus it cannot be tolerated. MR damper actuation appears to be very efficient in this case to increase the damping of the system. The feedback linearization strategy is applied and its results are plotted in Fig. 3.8. The increase of the damping force during coalescence allows maintains the modal damping of the low frequency mode at the design stability margins. The system has been stabilized even though two dampers have been severely degraded.

Fig. 3.9 shows the modal damping diagram of the system with two dampers inoperative at 50% in the asymmetric configuration. In this case, due to the asymmetric damper degradation, the more severe instability is caused. From Fig 3.9 we can see that the first and second coalescences exhibit higher maximum modal damping than the previous case. MR dampers are actuated using feedback linearization control strategy to increase the damping of the system. The stability margins are maintained at the design stability margins at both first and second coalescences as shown in Fig. 3.10. Again, the system has been stabilized even though two dampers have been severely degraded.

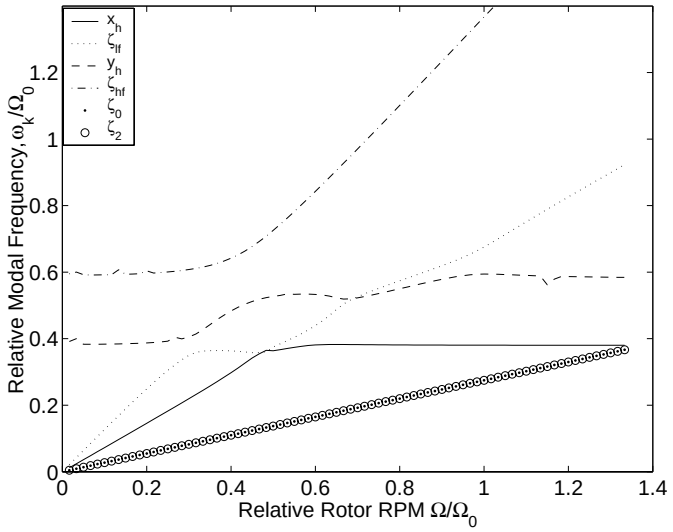

(a) Coleman diagram

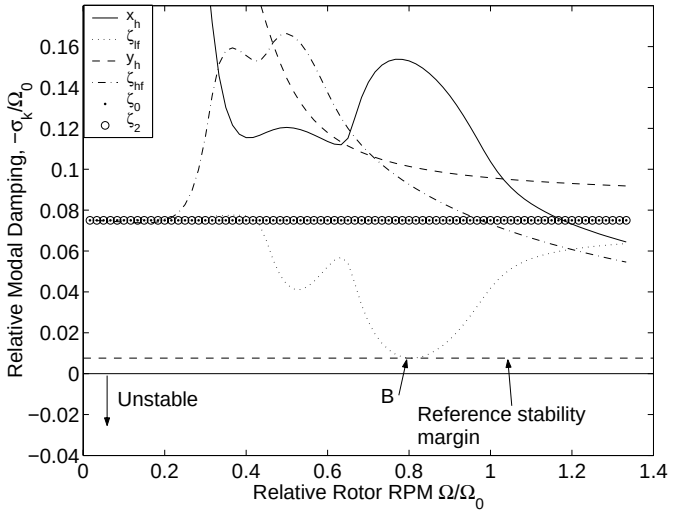

(b) Modal damping diagram

Figure 3.1: Coleman and modal damping diagram of the baseline stable system for damper degradation

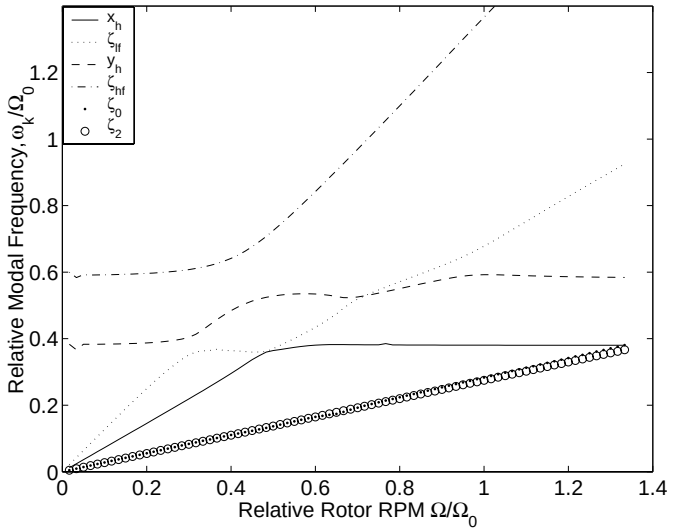

(a) Coleman diagram

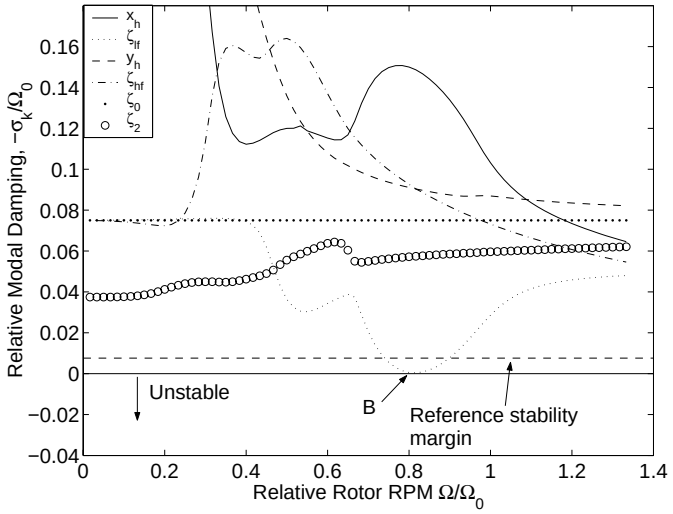

(b) Modal damping diagram

Figure 3.2: Coleman and modal damping diagram of the rotor system with lag damping in one blade degraded by 50%

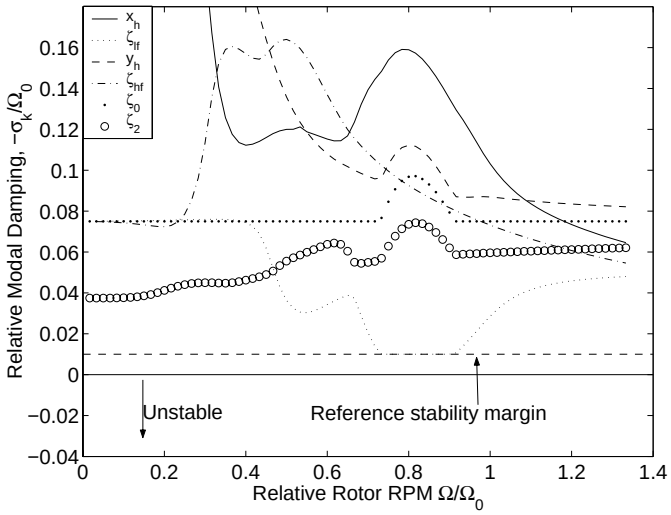

Figure 3.3: Modal damping diagram of the rotor system with lag damping in one blade degraded by 50% with damping control

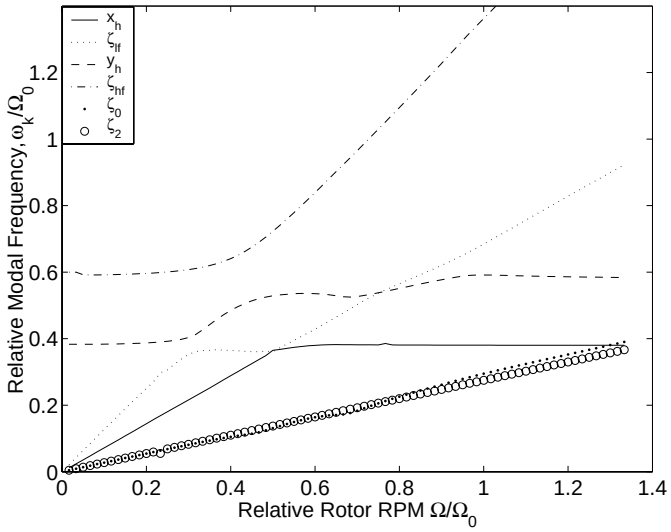

Figure 3.4: Coleman diagram of the system with lag dampers in one blade inoperative at 100%

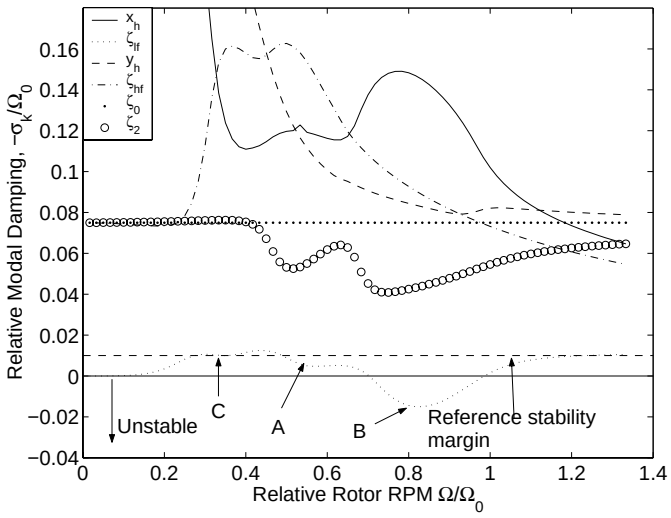

Figure 3.5: Modal damping diagram of the system with inoperative lag dampers on one blade

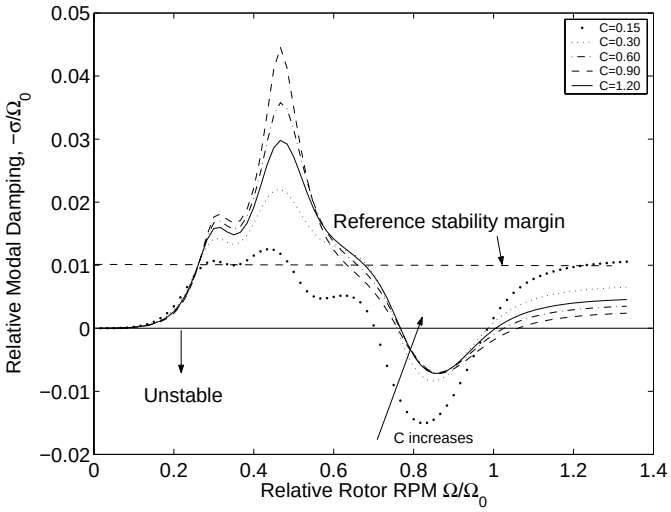

Figure 3.6: Effects of the controllable damping constant $\bar{c}$ on the undamped mode

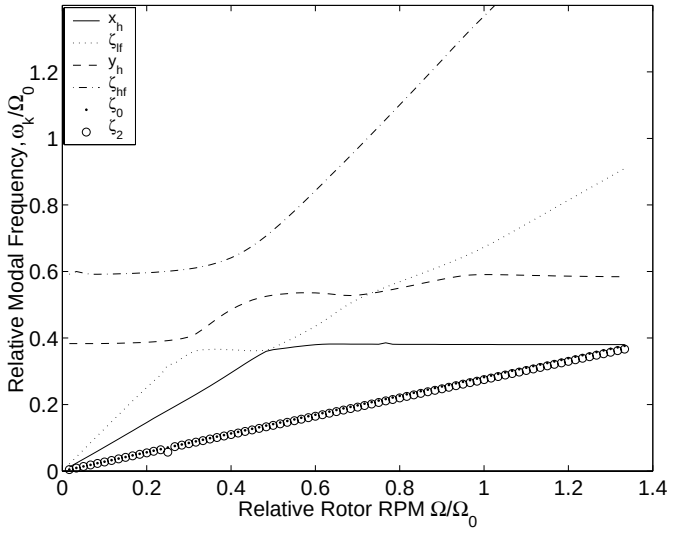

(a) Coleman diagram

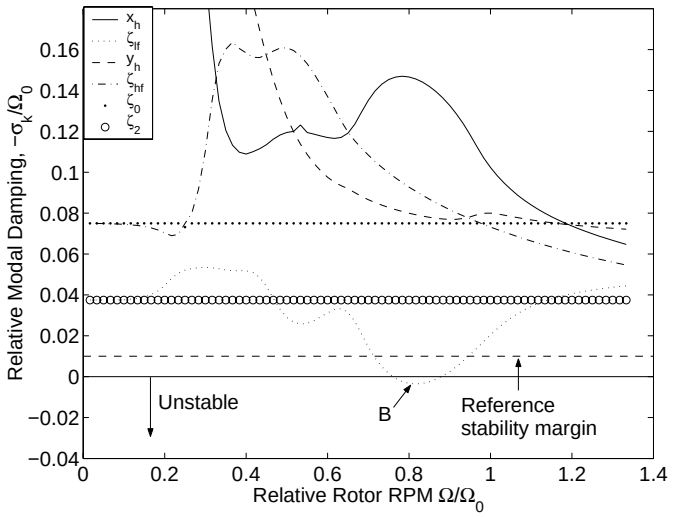

(b) Modal damping diagram

Figure 3.7: Colemand and modal damping diagram of the four bladed rotor with lag dampers inoperative at 50% on opposite blades (symmetric)

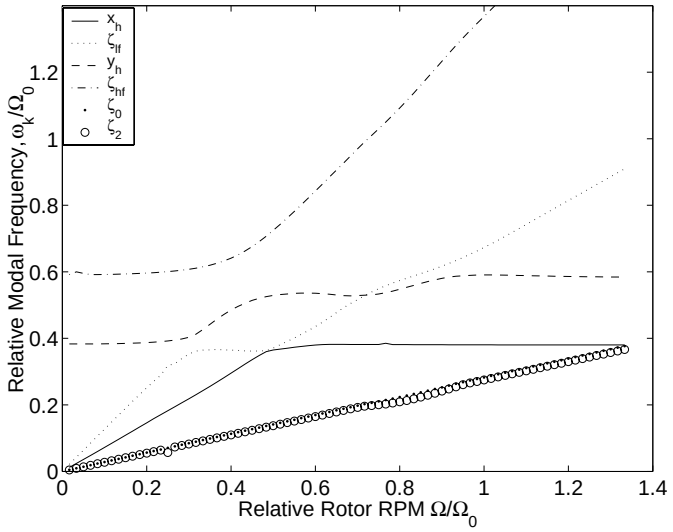

(a) Coleman diagram

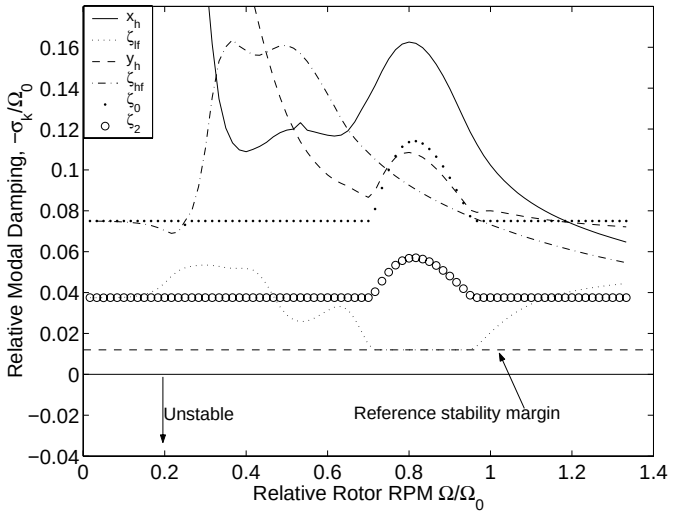

(b) Modal damping diagram

Figure 3.8: Coleman and modal damping diagram of the four bladed rotor with lag dampers inoperative at 50% on opposite blades (symmetric) with damping control

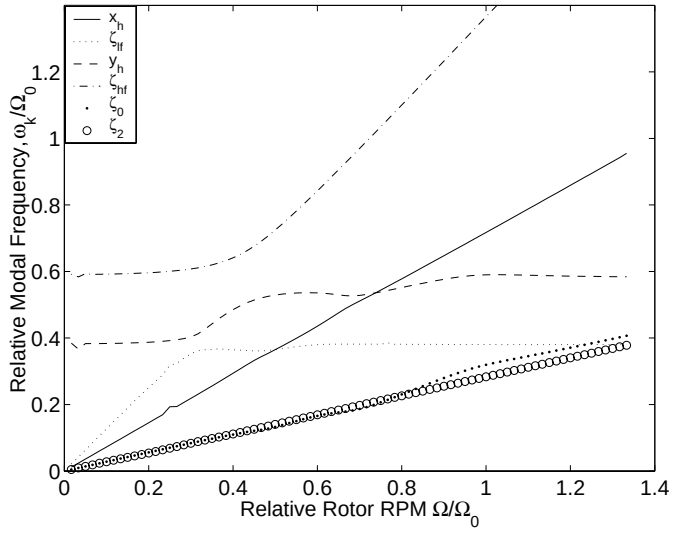

(a) Coleman diagram

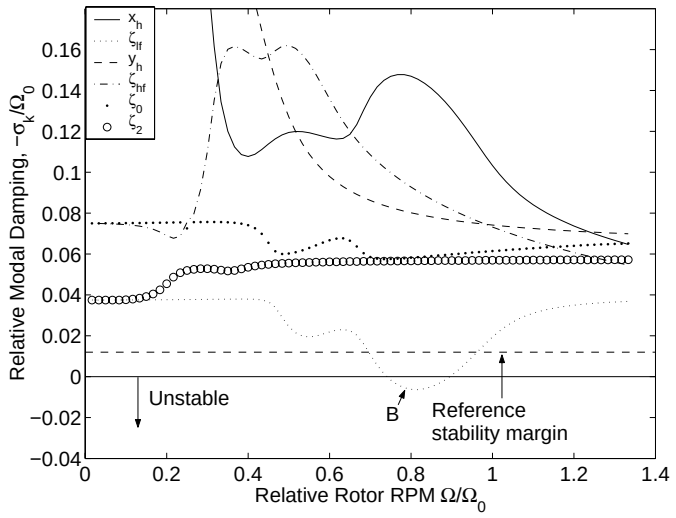

(b) Modal damping diagram

Figure 3.9: Coleman and modal damping diagram of the four bladed rotor with lag dampers inoperative at 50% on neighboring blades (asymmetric)

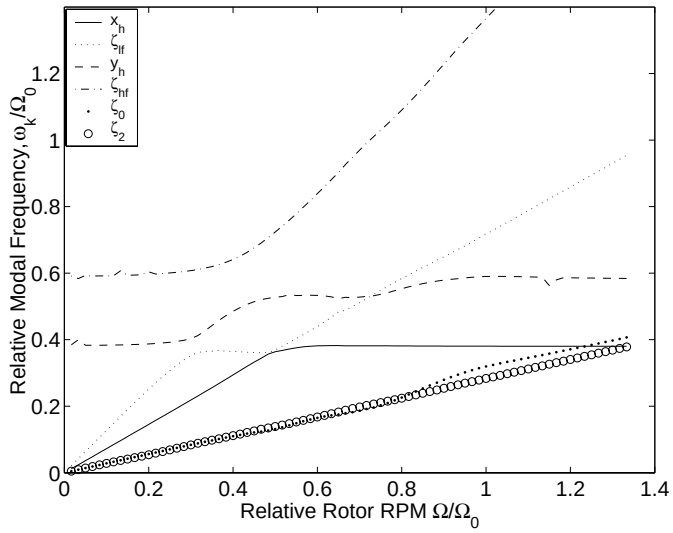

(a) Coleman diagram

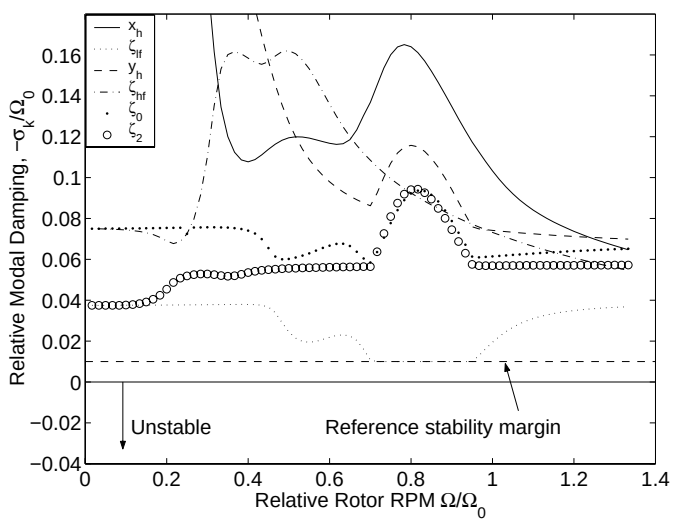

(b) Modal damping diagram

Figure 3.10: Coleman and modal damping diagram of the four bladed rotor with lag dampers inoperative at 50% on neighboring blades (asymmetric) with damping control

Chapter 4

Robustness to Model Error

In the last two chapters, we examined control strategies for MR dampers, and investigated robustness in case of damper damage. We will consider robustness to modeling error in this chapter. In an engineering environment, the nominal model differs from the physical system because high order modes are neglected and because of linearization. The parameters for nominal models are estimated and are assumed constant. However, this may not accurately represent the physical situation. The parameters may vary over a range, so that the model may not be accurate. The designed control strategies not only need to perform well for the nominal model, but also need to perform well for the physical system. Thus, research on control strategy robustness is necessary.

The uncertainties of a nonlinear system can be grouped into three classes[119]. The first is the parametric uncertainty, that is, the model structure is very well known but the parameters may have some uncertainties. The second is unstructured uncertainty, that is, the model itself presents some uncertainties. The third is unmodeled dynamics. In this kind of uncertainty, the modeling process involves model simplification and order reduction based on the assumption that

certain high frequency modes can be neglected. The result is that these neglected modes becomes unmodeled dynamics in the system.

Robust control methodologies designed to deal with system uncertainties have been researched for more than one decades. It has been shown [120, 121] that feedback linearization and adaptive control techniques can deal with parametric uncertainties. The sliding mode control and Gaussian Networks [122, 123] can be used for systems with unstructured uncertainties. Some robust control system design techniques based on Lyapunov stability theory and singular perturbation techniques have been shown to be effective in handling unmodeled dynamics. For the system with more than one kind of uncertainty, the structured singular value approach is effective[124].

The above robust control methodologies, though effective, require advanced mathematics and will result in very complex control algorithms. It was shown that damping augmentation and damping control can not only increase the stability of a system, but also increase the stability robustness [125]. In previous research the damping controls we developed focused on augmenting stability of the system. In this chapter, we will examine if the control strategies are robust and how to improve the robustness of the controllers. We will concentrate on the robustness of the ground resonance control system to parameter perturbations. The parameters perturbed will include mass, damping, and stiffness variables.

Next, The two control strategies, sliding mode control and feedback linearization will be examined under parameter perturbations. The robustness of the control strategies will be assessed and compared. A method to improve the robustness will be proposed.

4.1 Perturbation of Mass

The mass of the helicopters is assumed to be constant in previous chapter. However, it may change due to varying payload and fuel consumption. There are three parameters in the mass matrix of the equation, namely the longitudinal mass $\bar{M}_x$, the lateral mass $\bar{M}_y$, and the first moment of mass about lag hinge S_ζ. We will perturb each of these parameters by as much as $\pm 20\%$. For example, $\bar{M}_x = (1 + \Delta)\bar{M}_x^0$, in order to study the performance of control strategies. Here, $\bar{M}_x^0$ is the nominal longitudinal mass and $\bar{M}_x$ is the perturbed mass, and $\Delta = \pm 20\%$. Both M_y and $\bar{S}_\zeta$ are treated in a similar way.

4.1.1 Perturbation of $\bar{M}_x$

We first assess robustness of the feedback linearization control strategy. The control input is calculated without perturbation. Then the $\pm 20\%$ perturbation is added. The modal damping is calculated for the RPM from 0 to 300 and the modal damping diagrams are drawn. The results are shown in Fig. 4.1 a) and 4.1 b). When $\bar{M}_x$ increases, the modal damping increases too. When M_x decreases, the modal damping decreases. However, since we pre-set the stability margin, the decrease of the modal damping will not cause the instability. The system is still stable. In other words, the feedback linearization control strategy is robust to the perturbation of $\bar{M}_x$.

For the sliding mode control, the modal damping diagram is not available. We can only show the time response for each RPM. We only show the result of one RPM frequency. The results of other RPMs are similar. Figure 4.2 a) and 4.4b) are the results of $\pm 20\%$ perturbation of $\bar{M}_x$ at RPM 240. The system is

still stable under the perturbation. Hence, the sliding mode control is robust to the perturbation of $\bar{M}_x$.

4.1.2 Perturbation of $\bar{M}_y$

Similar to the perturbation of M_x, we add $\pm 20\%$ perturbation to M_y. First, the feedback linearization control strategy is used. The modal damping diagrams are shown in Fig. 4.3 a) and 4.3 b). A conclusion similar to that reached for $\bar{M}_x$ is found. Alhough decreasing the $\bar{M}_y$ decreases the modal damping, the stability margin of nominal plant prevents system instability. The feedback linearization control strategy is robust to the perturbation in $\bar{M}_y$.

Figure Fig. 4.4 a) and 4.4 b) are the results of $\pm 20\%$ perturbation of $\bar{M}_y$ at RPM 240, when using sliding mode control as well. The system is stable under the perturbation.

4.1.3 Perturbation of $\bar{S}_\zeta$

The results of $\bar{S}_\zeta$ are slightly different from the above. For feedback linearization control, the increase of $\bar{S}_\zeta$ will cause a decrease in the modal damping. The helicopter system can tolerate at most a perturbation of $\Delta = 14\%$ of the perturbation. The results are shown in Fig. 4.5 a) and 4.5 b). The system is stable under the perturbation though the marginal stability is reached.

For sliding mode control, the $\pm 20\%$ perturbation of $\bar{S}_\zeta$ added. The results of sliding mode control are shown in Fig. 4.6 a) and 4.6 b).

4.1.4 Robustness to Mass Perturbation

The robustness of the two control strategies to mass perturbation was investigated. It was found that both control strategies are robust to perturbations of $\bar{M}_x$ and $\bar{M}_y$. For $\bar{S}_\zeta$, the sliding mode control showed more robustness than the feedback linearization control.

4.2 Perturbation of Damping Matrix

In the damping matrix, the parameters $\bar{C}_x$ and $\bar{C}_y$ are the effective damping of landing gear. We assume that the damping of landing gear can be mesured accurately. We perturbed them at $\pm 20\%$ to evaluate the robustness.

4.2.1 Perturbation of $\bar{C}_x$

For the feedback linearization control, the $\pm 20\%$ perturbation of $\bar{C}_x$ only results in slight changes to the modal damping diagram and does not make the system unstable. Results are shown in Fig. 4.7 a) and Fig. 4.7 b).

The results of sliding mode control are shown in Fig. 4.8 a) and Fig. 4.8 b). Sliding mode control also shows robustness to perturbations in $\bar{C}_x$

4.2.2 Perturbation of $\bar{C}_y$

The same results are obtained for the $\pm 20\%$ perturbation of $\bar{C}_y$. The results of feedback linearization control and sliding mode control are shown in Fig. 4.9 a), Fig. 4.9 b), Fig. 4.10 a), and Fig. 4.10 b).

4.2.3 Robustness to Damping Parameters

Both control strategies show the robustness to damping parameters $\bar{C}_x$,$\bar{C}_y$. The $\pm 20\%$ perturbation does not cause instability in the system.

4.3 Perturbation of Stiffness Matrix

In the stiffness matrix, the parameters we will perturb are nondimensional lag frequency ν_ζ, effective longitudinal frequency ω_x, and effective lateral frequency ω_y.

4.3.1 Perturbation of ν_ζ

The results of perturbation of ν_ζ are shown in Fig. 4.11 and Fig. 4.12. The feedback linearization control is sensitive to the ν_ζ. The $\pm 20\%$ perturbation will cause system unstable. However, it can still tolerate $\pm 5\%$ perturbation. For sliding mode control, with $\pm 20\%$ perturbation, the system remains stable.

4.3.2 Perturbation of ω_x

The $\pm 10\%$ perturbation is added to ω_x. The results of feedback linearization control are shown in Fig. 4.13 a) and Fig. 4.13 b). The system remain stable though the stability margin requirement is not satisfied.

The $\pm 10\%$ perturbation is added to ω_x for sliding mode control. The results of sliding mode control are shown in Fig. 4.14 a) and Fig. 4.14 b).

4.3.3 Perturbation of ω_y

For the perturbation of ω_y, the results of feedback linearization control are shown in Fig. 4.15 a) and Fig. 4.15 b). According to the results the feedback linearization control can tolerate about $\pm 5\%$ perturbation.

For sliding mode control, the results are shown in Fig. 4.16 a) and Fig. 4.16 b). The sliding mode control shows the more robustness to feedback linearization control. With $\pm 20\%$ perturbation, the system remain stable.

4.4 Comparison of robustness of two controls and Improvement of the Robustness

In the last section, the sliding mode control exhibites stronger robustness characterstics than the feedback linearization control. The sliding mode control is not sensitive to any of parameters perturbations. However, feedback linearization control is sensitive to some parameters. In this section, we will deeply explore the reason and how to improve the robustness of feedback linearization. We choose the perturbation of ω_y as an example. The frequency we choose is RPM 180. From Fig. 4.18, we can see that the system will become unstable if the perturbation become large. A $\Delta = -20\%$ perturbation is added and the time responses of system are researched. The cyclic response and the control input at first blade by using feedback linearization and sliding mode control are shown in Fig. 4.17 a) to Fig. 4.17 b) respectively. The feedback linearization control has an unstable response and the sliding mode control has a stable response. By comparing the control inputs of the two control strategies, we found that the control inputs of sliding mode control is almost twice as large as that of feedback

linearization control. The small control input may be the reason that the feedback linearization is less robust. Then we double the desired stability margin of the system and use Eqn. 2.31 to recalculate the control gain. The control gain of feedback linearization control is increased. The system is stabilized even under the -20% of the perturbation with enough control input. Results are shown in Fig. 4.19 a) and Fig. 4.19 b). The robustness of the feedback linearization control is increased.

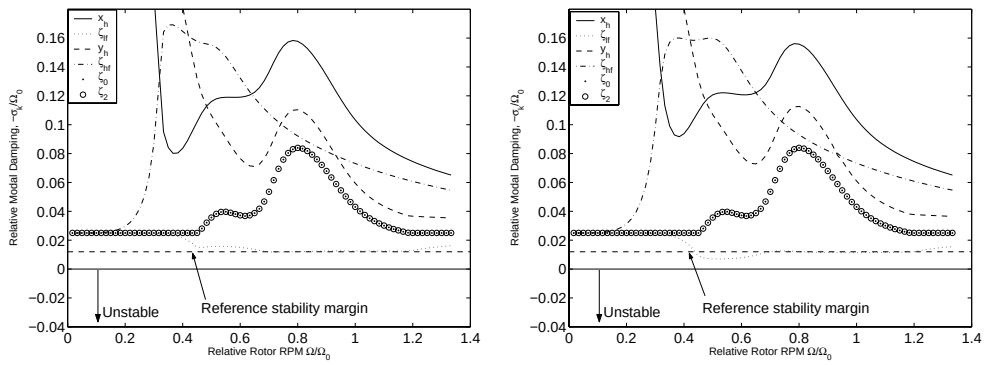

(a) 20% perturbation (b) -20% perturbation

Figure 4.1: The modal damping diagram for the ±20% perturbation of $\bar{M}_x$

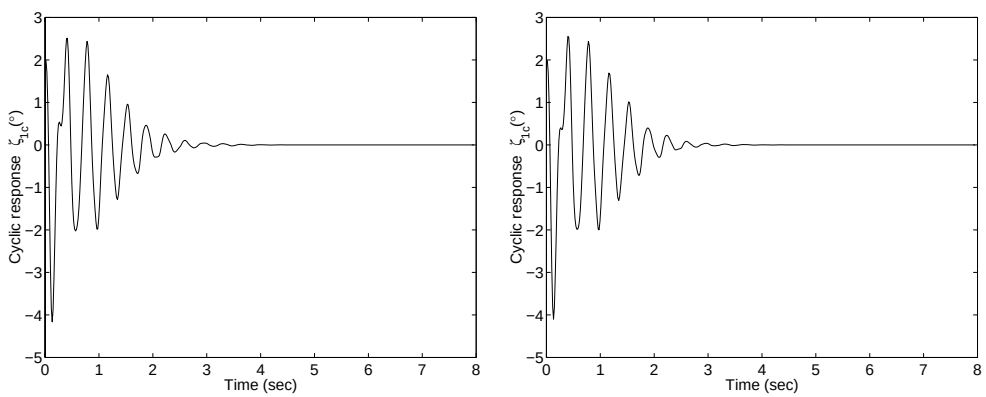

(a) 20% perturbation (b) -20% perturbation

Figure 4.2: The cyclic response of sliding mode control for the ±20% perturbation of $\bar{M}_x$

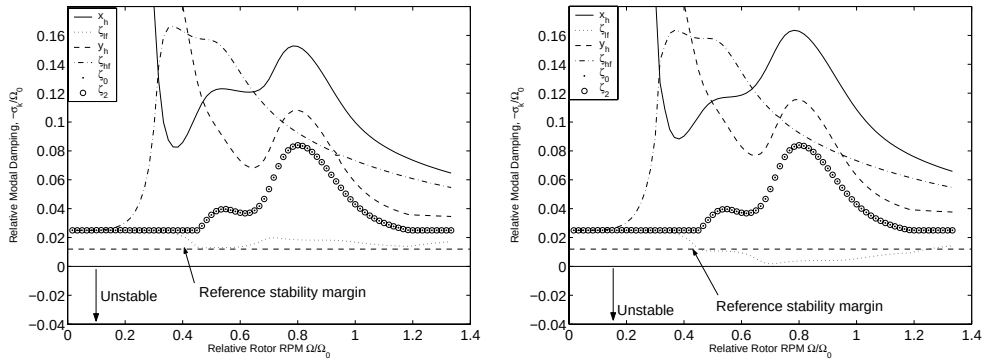

(a) 20% perturbation (b) -20% perturbation

Figure 4.3: The modal damping diagram for the ±20% perturbation of $\bar{M}_y$

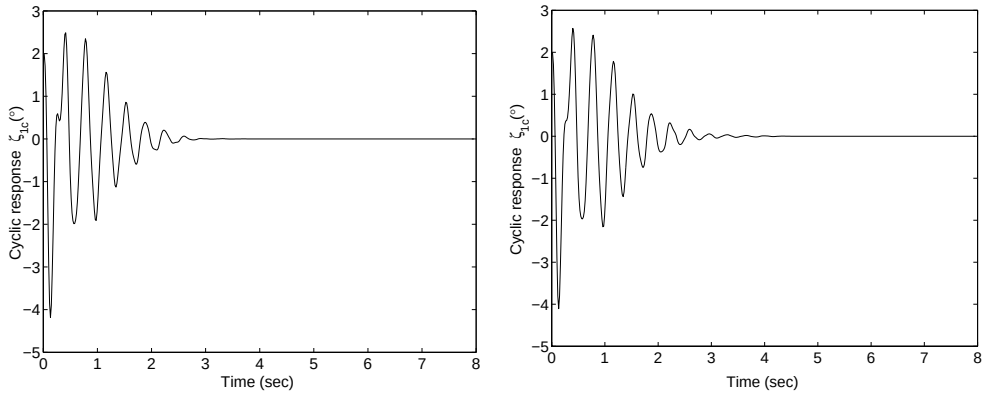

(a) 20% perturbation (b) -20% perturbation

Figure 4.4: The cyclic response of sliding mode control for the ±20% perturbation of $\bar{M}_y$

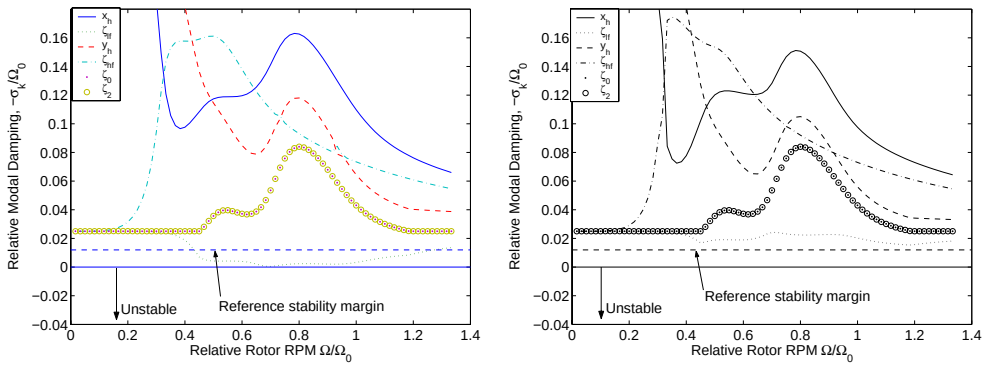

(a) 14% perturbation (b) -14% perturbation

Figure 4.5: The modal damping diagram for the ±14% perturbation of $\bar{S}_\zeta$

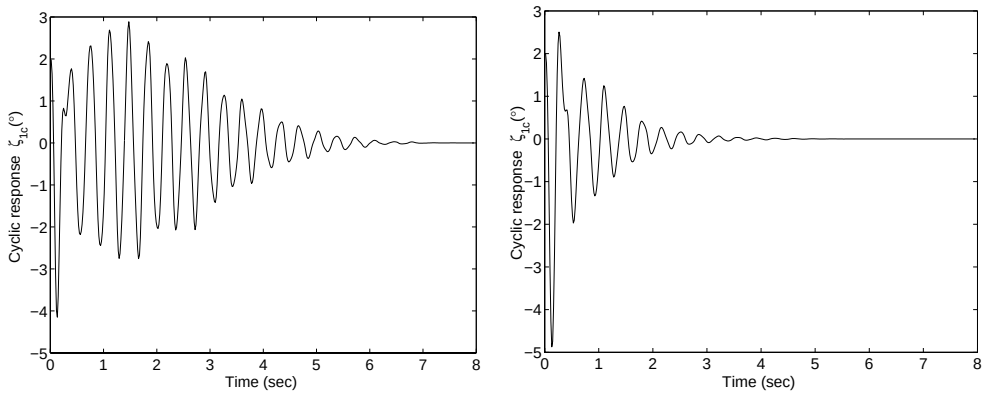

(a) 20% perturbation (b) -20% perturbation

Figure 4.6: The cyclic response of sliding mode control for the ±14% perturbation of $\bar{S}_\zeta$

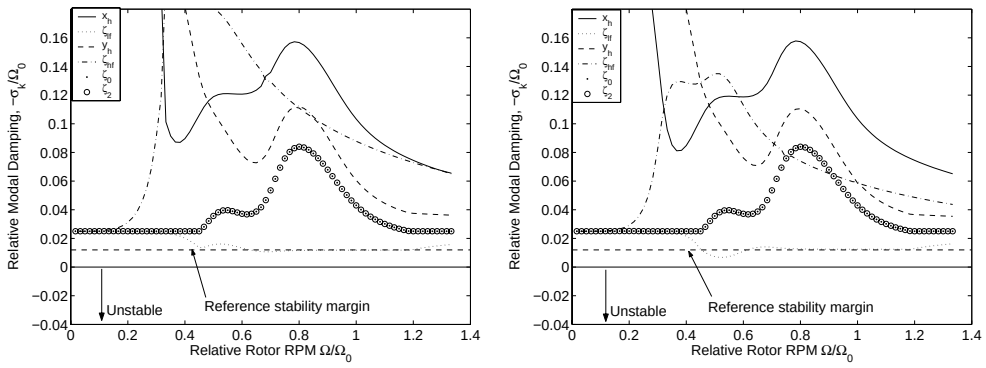

(a) 20% perturbation (b) -20% perturbation

Figure 4.7: The modal damping diagram for the ±20% perturbation of $\bar{C}_x$

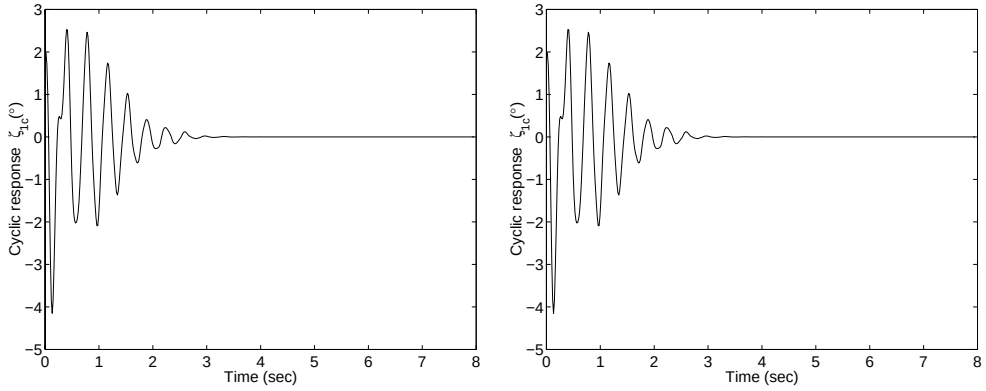

(a) 20% perturbation (b) -20% perturbation

Figure 4.8: The cyclic response of sliding mode control for the ±20% perturbation of $\bar{C}_x$

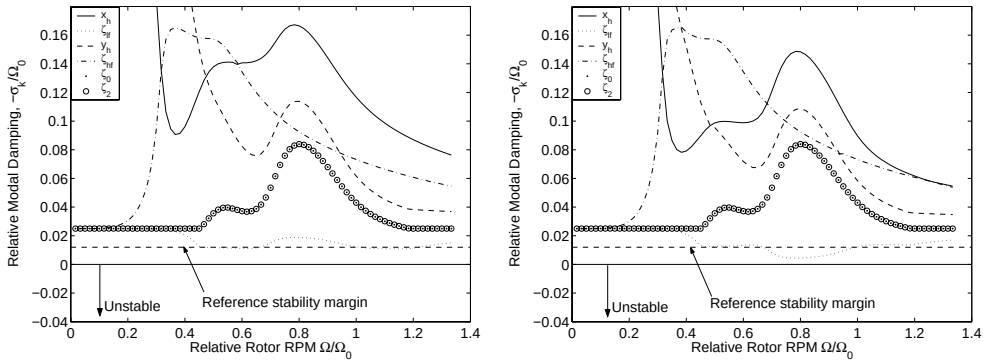

(a) 20% perturbation (b) -20% perturbation

Figure 4.9: The modal damping diagram for the ±20% perturbation of $\bar{C}_y$

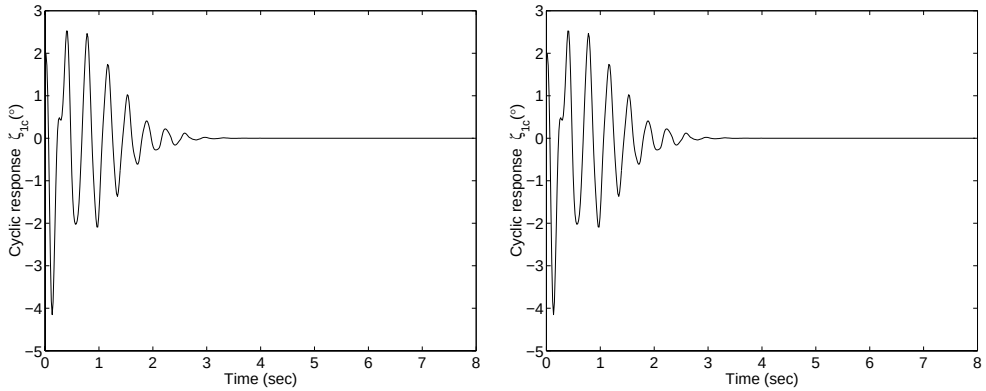

(a) 20% perturbation (b) -20% perturbation

Figure 4.10: The cyclic response of sliding mode control for the ±20% perturbation of $\bar{C}_y$

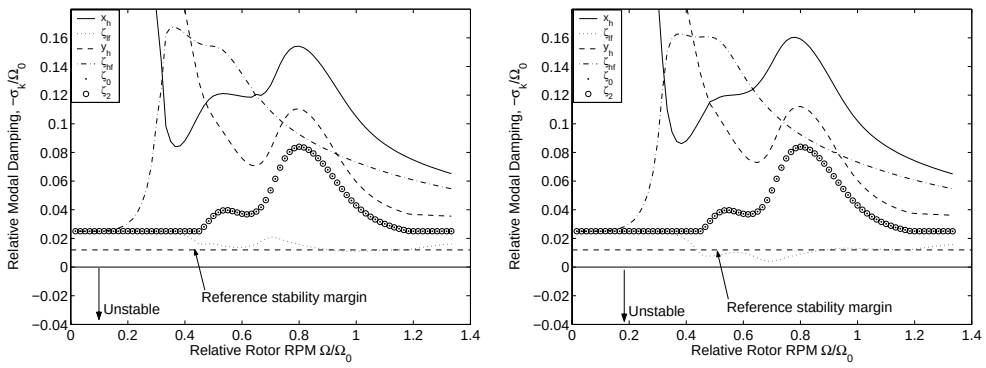

(a) 5% perturbation (b) -5% perturbation

Figure 4.11: The modal damping diagram for the ±5% perturbation of ν_ζ

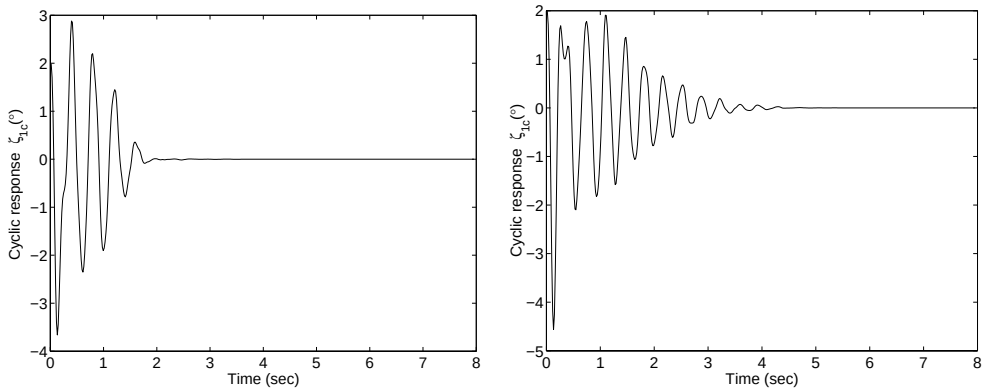

(a) 20% perturbation (b) -20% perturbation

Figure 4.12: The cyclic response of sliding mode control for the ±20% perturbation of ν_ζ

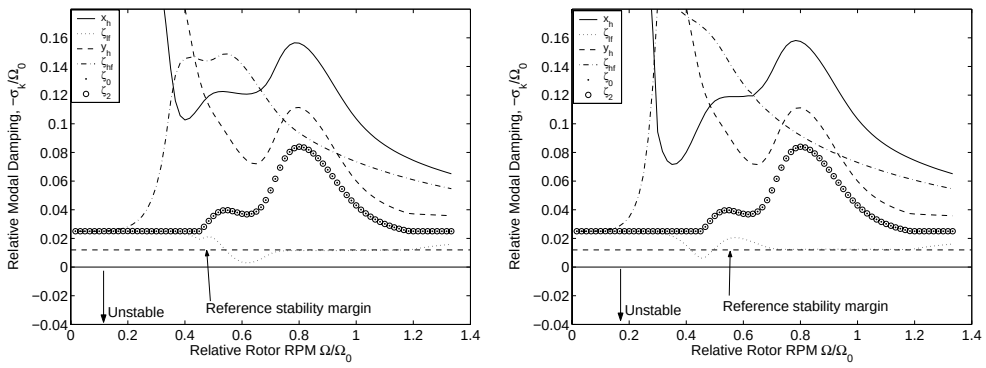

(a) 10% perturbation (b) -5% perturbation

Figure 4.13: The modal damping diagram for the ±5% perturbation of ω_x

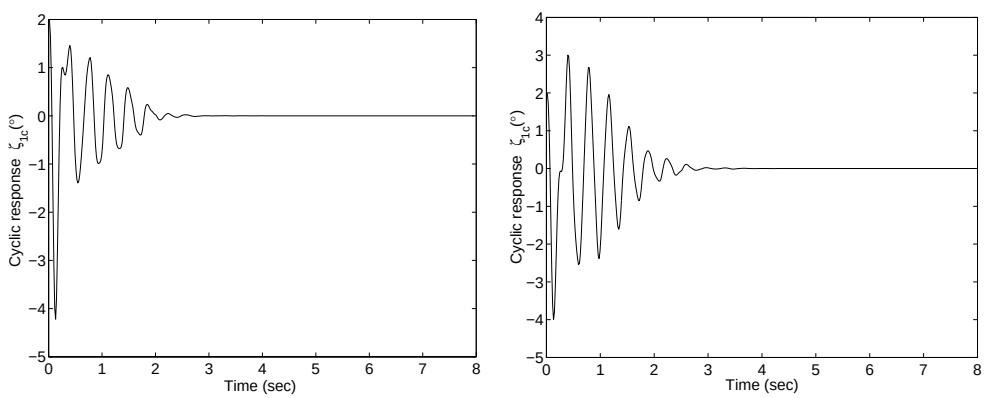

(a) 20% perturbation (b) -20% perturbation

Figure 4.14: The cyclic response of sliding mode control for the ±20% perturbation of ω_x

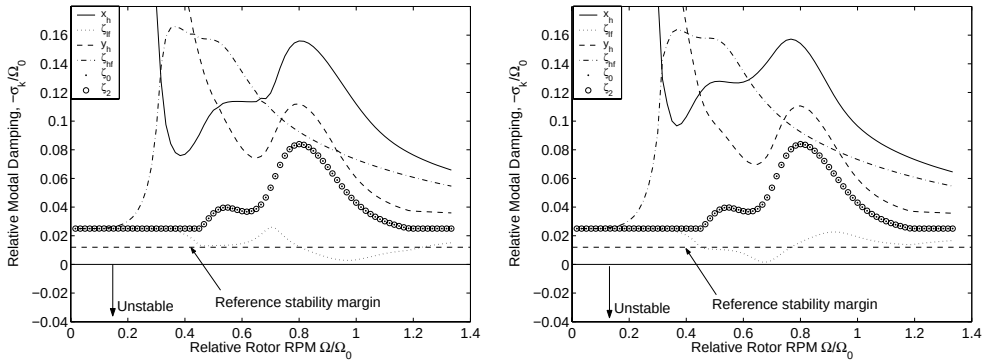

(a) 5% perturbation (b) -5% perturbation

Figure 4.15: The modal damping diagram for the ±5% perturbation of ω_y

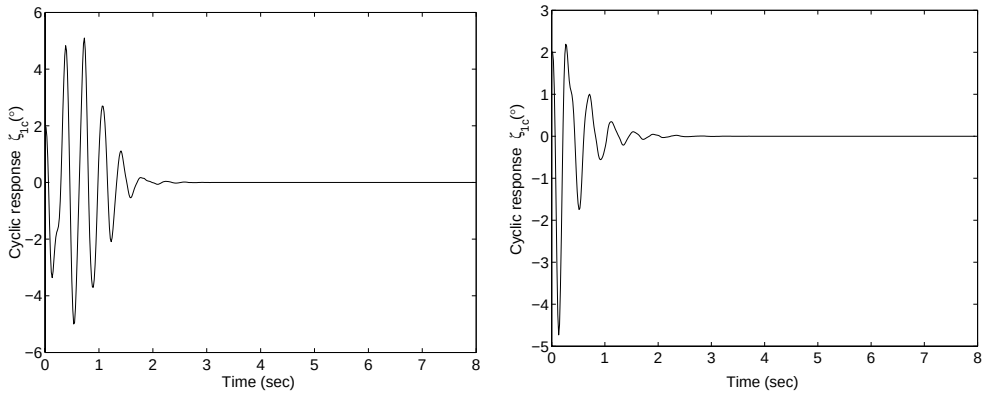

(a) 20% perturbation (b) -20% perturbation

Figure 4.16: The cyclic response of sliding mode control for the ±20% perturbation of ω_y

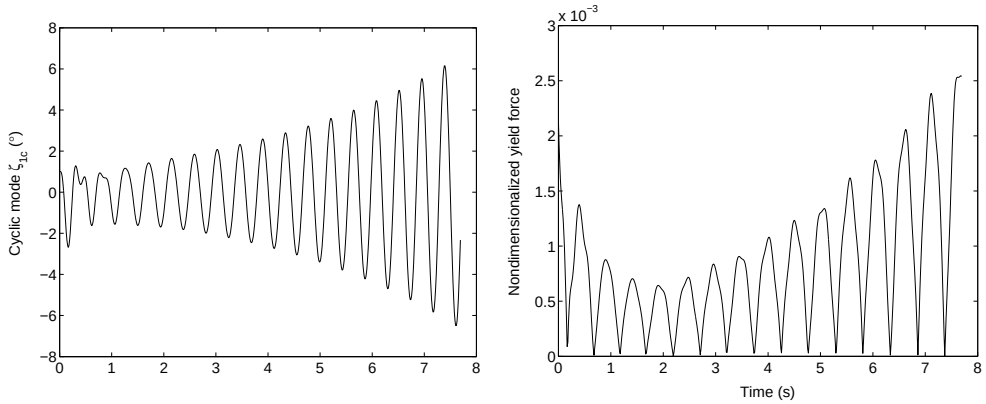

(a) Cyclic response (b) Control input

Figure 4.17: The time response of feedback linearization control for the -20% perturbation of ω_y

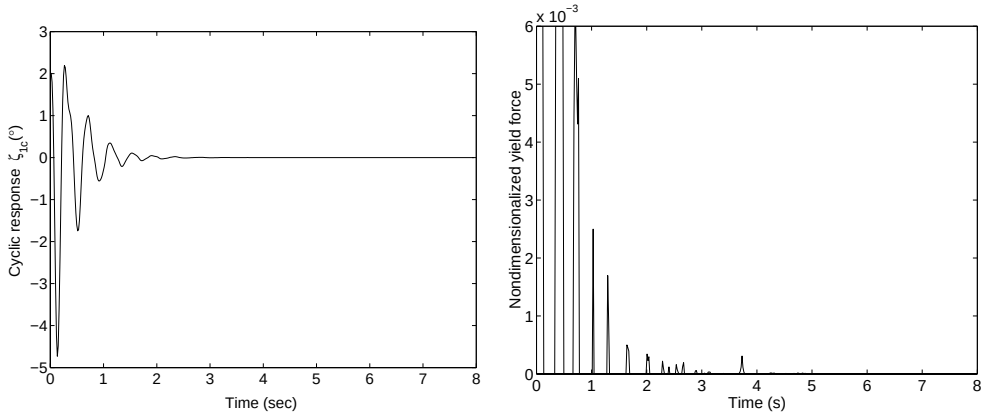

(a) Cyclic response (b) Control input

Figure 4.18: The time response of sliding mode control for the -20% perturbation of ω_y

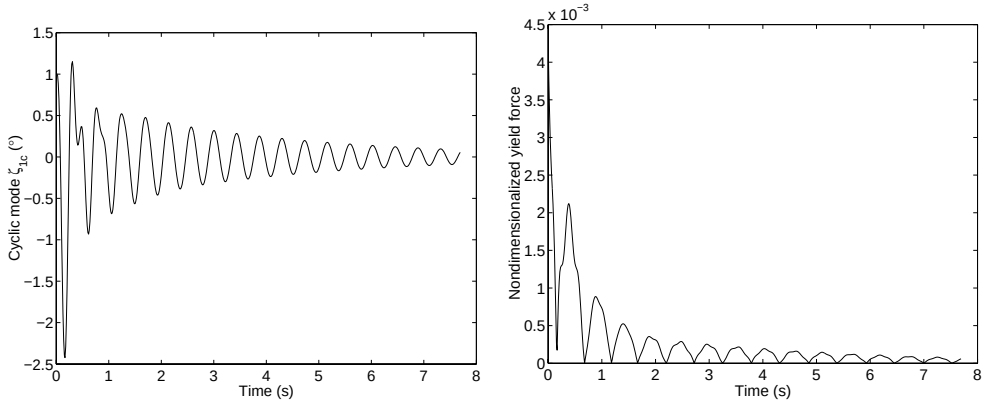

(a) Cyclic response

(b) Control input

Figure 4.19: The time response of feedback linearization control for the -20% perturbation of ω_y when control increased

Chapter 5

Linear Damping Identification in Helicopter Rotor Systems

Having the control algorithms of MR dampers, experimentation should be undertaken to evaluate the damping level provided by MR dampers. An accurate damping identification techique is needed to estimate damping level from test data. Traditionally, the lead-lag damping is evaluated by using rotor stability test. The rotor is first trimmed and the modes of the interest are excited through the rotor control mechanism called the swash plate. The excitation is then terminated at peak amplitude and the ensuing transient response acquired. In addition, the peak amplitude of each transient is determined, and when the maximum amplitude of the transient drops below a specified value, the data set is truncated for analysis. In this chapter, the identification viscous damping from the transient response is examined. Three methods to identify the modal damping from the transient response are considered: (1) Hilbert transform, (2) Fourier series based moving block method, (3) wavelet transform. The critical step of the three methods is the identification of the envelope signal. The damping mechanism can be classified by the shape of the envelope signal. The decay

rate of the envelope signal and the natural frequency are then used to determine the damping level.

5.1 Viscous Damping Identification

Classic viscous damping is commonly associated with the damping of fluid-filled dashpot dampers. The characteristic equation for a viscously damped single degree of freedom (SDOF) system is:

$$\ddot{y} + 2\zeta\omega_n\dot{y} + \omega_n^2 y = 0 \tag{5.1}$$

and the normalized envelope signal of the transient response is given analytically as

$$a = e^{-\zeta\omega_n t} \tag{5.2}$$

Then the damping can be given as

$$\zeta = \frac{-\ln a(t)}{\omega_n t} \tag{5.3}$$

In general, the critical step in damping analysis from transient response is the identification of the envelope signal $\hat{a}(t)$. After identifying the envelope signal of the experimental response, $\hat{a}(t)$, an estimate for the experimental damping ratio, $\hat{\zeta}(t)$, can be determined. To obtain this estimate, a cost function was defined as the least mean square (LMS) error between the natural log of the analytical and identified envelope signals.

$$\begin{aligned} \hat{\zeta}(t) &= argmin J_\nu(\zeta) \\ &= argmin \sum [\ln a(t_k) - \ln \hat{a}(t_k)]^2 \end{aligned} \tag{5.4}$$

For the multi degree of freedom system, we would like to isolate the mode of interests, by either isolating the transient signal then calculating the envelope signal or isolating the envelope signal directly. The damping of the mode if interest can then be estimated from the envelope signal.

The modal frequency of interest is an important element of damping identification. The general approach to identify the modal frequency is to take the FFT for the measured signal. The frequency resolution to determined by the time span of the original signal and can be improved by zero padding technique for multi-mode systems. The second method is a standard state frequency response function measurement, using a sine sweep focused around the mode of interest, ensuring high frequency resolution. It is routine to achieve frequency resolution of $\Delta f = 0.1$ Hz to $\Delta f = 0.01$ Hz using excitation signal duration of from T=10 sec to T=100 sec.

5.2 Rotor Stability Test Data

Helicopter rotor stability test data typically consists of lag/rev mode transient data: after the lag mode is excited in the spinning rotor at the lag mode frequency or lag/rev, the excitation is terminated and the lag response is measured. This data is characterized by high noise levels, the lag/rev is corrupted by persistent excitation at the rotor speed or 1/rev that is typically higher than the lag mode response in amplitude and is spectrally close to the lag mode. Based on this characteristic, the canonical form of test data can be written as

$$y(t) = Y_{lag} e^{-\zeta \Omega_{lag} t} \cos(\Omega_{lag} t) + Y_1 e^{-\zeta_1 \Omega t} \cos(\Omega t + \phi) \tag{5.5}$$

where we assume that Ω_{lag} is the natural frequency of the first lag mode, and Ω is 1/rev rotor frequency. Actually,Ω_{lag} is spectrally close to and but less than Ω, so that we may express $\Omega_{lag} = \alpha\Omega$ where $\alpha < 1$. Y_{lag} and Y_1 are their initial amplitude respectively. In hover stand test data, the Y_1 is much less than Y_{lag}. However, in forward flight test data, Y_1 is usually comparable to Y_{lag}. ζ is the damping of the first lag mode and ζ_1 is the damping of the 1/rev persistent excitation and usually is 0.

The problem considered in this chapter is that how to identify the lag/rev damping ζ from the total transient test record $y(t)$.

5.3 Damping Identification Technologies

5.3.1 Hilbert Transform

The Hilbert transformation of a one-dimensional real signal (function) $y(t)$ is defined by the integral

$$\tilde{y}(t) = \frac{-1}{\pi} \int_{-\infty}^{\infty} \frac{y(\tau)}{\tau - t} d\tau \tag{5.6}$$

Hilbert transform is a typical envelope estimator with wide applications. Its application to damping identification of SDOF system is simple and straightforward. Suppose that the decaying transient is given by

$$y(t) = a(t)\cos(\omega_d t + \phi) \tag{5.7}$$

The Hilbert transform is then the signal, phase shifted by 90°, as here:

$$\tilde{y}(t) = a(t)\sin(\omega_d t + \phi) \tag{5.8}$$

The most useful interpretation of the Hilbert transform is as the imaginary part of an analytic signal. We define the analytic signal

$$z(t) = y(t) + j\tilde{y}(t) \tag{5.9}$$

as the sum of the real signal, y(t), plus an imaginary Hilbert transform signal, $\tilde{y}(t)$. The phase form is:

$$z(t) = a(t)e^{j\theta(t)} \tag{5.10}$$

where $a(t)$ is the envelope signal of y(t), and $\theta(t)$ is the instantaneous phase signal of y(t). Using the signal y(t), and its Hilbert transform, $\tilde{y}(t)$ the envelope signal is given by

$$\tilde{a}(t) = \sqrt{y^2(t) + \tilde{y}^2(t)} \tag{5.11}$$

Then we can apply Eqn. 5.4 to estimate the damping ratio.

The computation of Hilbert transform can be gotten as following[126]: Suppose $Z(\omega)$ is the Fourier transform of z(t), then

$$Z(\omega) = Y(\omega) + j\tilde{Y}(\omega) \tag{5.12}$$

where $Y(\omega)$ and $\tilde{Y}(\omega)$ are Fourier transform of $y(t)$ and $\tilde{y}(t)$ respectively.

According to the properties of Hilbert Transform:

$$\tilde{Y}(\omega) = (-jsgn(\omega))Y(\omega) \tag{5.13}$$

then

$$Z(\omega) = (1 + sgn(\omega))Y(\omega) \tag{5.14}$$

The diagram of the Hilbert transform is shown in Fig. 5.1 (b). To apply Hilbert transform to MDOF system, isolation of the mode of interesting by prefiltering is required.

5.3.2 Fourier Series Based Moving Block (FSMB)

Moving block analyzes are based on short time Fourier transform and widely used in the rotorcraft industry to identify damping of rotor modes such as blade flap, lag and torsion modes. A brief derivation of the moving block method is given below. The more comprehensive derivation is in [72]

The finite Fourier transform of damped sinusoidal signal is given by

$$F(\omega, \tau) = \int_{\tau}^{T+\tau} Ae^{-\zeta\omega_n t} sin(\omega_d t + \theta) e^{-i\omega t} dt \tag{5.15}$$

where ζ is viscous damping ratio, ω_n is the natural frequency, ω_d is the damped natural frequency, τ is the time origin of the transform and T is the block length. By assuming $\omega = \omega_n \approx \omega_d$, $\zeta << 1$ and T is an integral multiple of the basic period of oscillation, the natural log of the magnitude can be written as

$$ln|F(\omega)| = -\zeta\omega\tau + \frac{1}{2} sin2(\omega\tau + \theta) + C \tag{5.16}$$

where C is a constant given by

$$C = ln\frac{A}{2\omega} + ln(\omega T) - \frac{\zeta\omega T}{2} \tag{5.17}$$

Thus the plot of $ln|F(\omega)|$ against τ would be a straight line of slope $-\zeta\omega$ with a superimposed oscillatory part of frequency $2\omega_n$. The damping ratio can be extracted from the slope of such curves using linear least square fit.

There are several variations of calculation of moving block method function $|F(\omega)|$. Smith et al studied the FFT based moving block in detail and made the

conclusion that the frequency resolution of FFT based moving block is dependent on the block length. For accurate damping level estimation, especially for the nonlinear damping, the short block length is necessary. However, in a spectrally dense environment, a necessary feature of the damping analysis must be excellent frequency resolution in order to differentiate between spectrally close modes. It is not impossible to obtain both excellent frequency resolution and accurate damping identification using FFT-based moving block. Another method is Fourier series based moving block (FSMB). In this method the frequency resolution is not dependent on the block length, hence the difficulty of FFT-based moving block is mitigated. In this chapter, FSMB is used.

Calculation of Moving Block Function

In this method, suppose the motion equation is Eqn. 5.5, then the envelope of the lag/rev mode can be approximately expressed as

$$\hat{a}(t_k) = \sqrt{A_1(t_k)^2 + B_1(t_k)^2} \tag{5.18}$$

where the Fourier coefficients $A_1(t_k)$ and $B_1(t_k)$ are given by:

$$A_1(t_k) = \frac{\Omega_{lag}}{\pi N_c} \int_{t_k}^{t_k + \frac{2\pi N_c}{\Omega_{lag}}} y(t) \cos(\Omega_{lag} t) \mathrm{d}t \tag{5.19}$$

$$B_1(t_k) = \frac{\Omega_{lag}}{\pi N_c} \int_{t_k}^{t_k + \frac{2\pi N_c}{\Omega_{lag}}} y(t) \sin(\Omega_{lag} t) \mathrm{d}t \tag{5.20}$$

with N_c = block length in number of cycles of data where each cycle corresponds to a period of duration $2\pi/\Omega$, and then the window of data is moved forward one data point and coefficients are recalculated. This process is repeated for the number of iterations desired, $(k = 1, 2, 3, \cdots, N_i ter)$, and the envelope is then estimated using Eqn. 5.18

Once the envelope signal has been determined, Eqn. 5.4 can be applied to estimate the damping ratio.

Leakage and Windowing

When the FSMB method is applied to the two mode problem, spectral leakage is a major concern. Leakage is caused by the finite length of the transformed signal. This is equivalent to multiplying a signal of infinite length with a boxcar window. This multiplication corresponds to the convolution of the spectra of the boxcar window and of the infinite signal which leads to the generation of higher amplitude at frequencies other than those constrained in the original data. Energy is said to have leaked from the frequency of interest to other frequencies.

For reducing leakage effects two approaches may be followed[73, 78]: (1) increasing the length of the signal within the transform window and (2) using appropriate window function.

The window length (in seconds) can be increased either by increasing the transform size or by increasing Δt. Increasing transform size is limited by the available length of the transient signal and is by frequency separation between close modes. Increasing Δt is limited by the tolerable bandwidth and makes the constraint of aliasing become more important.

The finite length Fourier transform normally assumes a boxcar window function. It is well known that the use of other window functions, such as Hanning window causes a reduction in leakage. Ref[73] has demonstrated that the beat frequency become less severe when a Hanning window is used in the analysis. It was also concluded that the use of the Hanning window offers significant improvements in the estimation of the damping of close modes by the moving block

Table 5.1: Comparison of Hanning and Hamming Window

Window	Function	Width of main beam	Peak Sidelobe Amplitude (Relative To Main Beam Peak)
Hanning	$g(t) = \begin{cases} \cos^2(\frac{\pi t}{T_0}) & \lvert t\rvert \leq \frac{T_0}{2} \\ 0 & \lvert t\rvert \geq \frac{T_0}{2} \end{cases}$	$\frac{T_0}{4}$	0.028
Hamming	$g(t) = \begin{cases} 0.54 + 0.46\cos(\frac{\pi t}{T_0}) & \lvert t\rvert \leq \frac{T_0}{2} \\ 0 & \lvert t\rvert \geq \frac{T_0}{2} \end{cases}$	$\frac{T_0}{4}$	0.0089

method.

In this study we use a Hamming window instead of a Hanning Window. By changing the coefficient of Hanning window, the Hamming window reduces the sidelobe amplitude significantly without any change in the width of main beam. Table 1 shows the difference between two windowing functions. The diagram of the FSMB with Hamming window is shown in Fig. 5.1 (a).

5.3.3 Wavelet Transform

The continuous wavelet transform is defined as follows[82]:

$$W_g(a,b) = \frac{1}{\sqrt{a}} \int_{-\infty}^{\infty} x(t) g^* \left(\frac{t-b}{a} \right) dt \tag{5.21}$$

where a is dilation parameter, b is translation parameter, and $g^*(t)$ is the complex conjugate of the analyzing wavelet $g(t)$. Here, Morlet's wavelet:

$$g(t) = e^{j\omega_0 t} e^{-t^2/2} \tag{5.22}$$

is selected. In the equation, ω_0 is the wavelet frequency.

If we express the wavelet transform in frequency domain, the frequency localization is clearly seen,

$$W_g(a,b) = \sqrt{a}\int_{-\infty}^{\infty} X(\omega)G^*(a\omega)e^{j\omega b}d\omega \tag{5.23}$$

where $X(\omega)$ is the Fourier transform of $x(t)$ and $G(a\omega)$ is dilated Morlet wavelet in frequency domain:

$$G(a\omega) = e^{-(a\omega-\omega_0)^2} \tag{5.24}$$

The maximum of this function is reached when

$$a = \frac{\omega_0}{\omega} \tag{5.25}$$

The local resolution of the wavelet transform in time and frequency is determined by the dilation a and duration δt_g and bandwidth δf_g[83]:

$$\delta t = a\delta t_g \quad \delta f = \delta f_g/a \tag{5.26}$$

To apply the wavelet transform to damping identification, first a SDOF system is considered. Suppose the free response of the system is:

$$x(t) = A(t)\cos(\phi(t)t) \tag{5.27}$$

in which $A(t)$ and $\phi(t)$ are the time varying envelope and phase function. Assuming $A(t)$ is slowly varying, for the Morlet wavelet given in Eqn. 5.22, the wavelet transform of $x(t)$ can be approximated as:

$$W_g(a,b) = \sqrt{a}A(b)e^{(a_t\phi(b)-w_0)^2}e^{j\phi(b)b} \tag{5.28}$$

If the dilation parameter is fixed as $a = a_i$, which means for a fixed frequency, the modules of W_g is given by

$$|W_g(a_i, b)| = \sqrt{a_i} A(b) e^{(a_t \phi(b) - w_0)^2} \tag{5.29}$$

And the phase of W_g is

$$\angle W_g(a_i, b) = \phi(b) b \tag{5.30}$$

Using Eqn. 5.29 and 5.30, the time varying envelope $A(t)$ and $\phi(t)$ can be effectively determined, hence the damping ratio and natural frequency are identified.

For a MDOF system, the wavelet transform can isolate the decay of each mode of the structure separately from the others by selecting the right frequency value corresponding to the mode of interest, which requires a previous choice of the frequency of interest from the signal spectrum.

5.4 Error Analysis

5.4.1 Hilbert Transform

As we metioned early, the helicopter rotor stability test data can be written as:

$$y(t) = A_1 e^{-\zeta \omega_n t} \cos(\omega_n t + \phi_1) + A_2 \cos(\omega_2 t) \tag{5.31}$$

Its Hilbert transform is

$$\tilde{y}(t) = A_1 e^{-\zeta \omega_n t} \sin(\omega_n t + \phi_1) + A_2 \sin(\omega_2 t) \tag{5.32}$$

Thus the square of the envelope function estimated is:

$$\begin{aligned} z^2(t) &= y^2(t) + \tilde{y}^2(t) \\ &= (A_1 e^{-\zeta\omega_n t})^2 + A_2^2 + 2A_1A_2e^{-\zeta\omega_n t}\cos[(\omega_1 - \omega_2)t + \phi_1] \end{aligned} \tag{5.33}$$

However, the envelope we desired is the decaying lag mode envelope, which is

$$a^2(t) = (A_1 e^{-\zeta\omega_n t})^2 \tag{5.34}$$

So the error of envelope can be written as:

$$\epsilon[a^2(t)] = |a^2(t) - z^2(t)| = A_2^2 + 2A_1A_2e^{-\zeta\omega_n t}\cos[(\omega_1 - \omega_2)t + \phi_1] \tag{5.35}$$

The error normalized with respect to A_1 is

$$\bar{\epsilon}(t) = \frac{\epsilon[a^2(t)]}{A_1^2} = \left(\frac{A_2}{A_1}\right)^2 + 2\frac{A_2}{A_1}e^{-\zeta\omega_n t}\cos[(\omega_1 - \omega_2)t + \phi_1] \tag{5.36}$$

So the main effect to determine the envelope error is the amplitude ratio

$$\bar{\epsilon}(t) \to 0 \text{ as } \frac{A_2}{A_1} \to 0 \tag{5.37}$$

5.4.2 Moving Block Method

To use the moving block method, we write the helicopter rotor stability test data in another form:

$$y(t) = \alpha e^{-\zeta\omega_n t}\cos(\omega_n t) + \beta e^{-\zeta\omega_n t}\sin(\omega_n t) + A_2\cos(\omega_2 t) \tag{5.38}$$

Using moving block method, we can get

$$\begin{aligned}
\hat{A}(t) &= \int_t^{t+T} y(t)\cos(\omega_n t)dt = \int_t^{t+T} \alpha e^{-\zeta\omega_n t}\cos(\omega_n t)\cos(\omega_n t)dt \\
&+ \int_t^{t+T} \beta e^{-\zeta\omega_n t}\sin(\omega_n t)\cos(\omega_n t)dt + \int_t^{t+T} A_2\cos(\omega_2 t)\cos(\omega_n t)dt \\
&\approx \alpha e^{-\zeta\omega_n t} + \int_t^{t+T} A_2\cos(\omega_2 t)\cos(\omega_n t)dt \qquad (5.39)
\end{aligned}$$

The desired value of A(t) is

$$A(t) = \alpha e^{-\zeta\omega_n t} \qquad (5.40)$$

The error of estimation of A(t) is defined as

$$\epsilon_1 = \epsilon(A(t)) = \int_t^{t+T} A_2\cos(\omega_2 t)\cos(\omega_n t)dt \qquad (5.41)$$

Normalized it with respect with A_1: The error of estimation of A(t) is defined as

$$\bar{\epsilon}_1 = \frac{\epsilon(A(t))}{A_1} = \int_t^{t+T} \frac{A_2}{A_1}\cos(\omega_2 t)\cos(\omega_n t)dt \qquad (5.42)$$

Similarly, we have

$$\begin{aligned}
\hat{B}(t) &= \int_t^{t+T} y(t)\sin(\omega_n t)dt = \int_t^{t+T} \alpha e^{-\zeta\omega_n t}\cos(\omega_n t)\sin(\omega_n t)dt \\
&+ \int_t^{t+T} \beta e^{-\zeta\omega_n t}\sin(\omega_n t)\sin(\omega_n t)dt + \int_t^{t+T} A_2\cos(\omega_2 t)\sin(\omega_n t)dt \\
&\approx \beta e^{-\zeta\omega_n t} + \int_t^{t+T} A_2\cos(\omega_2 t)\sin(\omega_n t)dt \qquad (5.43)
\end{aligned}$$

The desired value of B(t) is

$$B(t) = \beta e^{-\zeta\omega_n t} \qquad (5.44)$$

The error of estimation of B(t) is defined as

$$\epsilon_2 = \epsilon(B(t)) = \int_t^{t+T} A_2\cos(\omega_2 t)\sin(\omega_n t)dt \qquad (5.45)$$

Normalized it with respect to A_1: The error of estimation of A(t) is defined as

$$\bar{\epsilon}_2 = \frac{\epsilon(B(t))}{A_1} = \int_t^{t+T} \frac{A_2}{A_1} \cos(\omega_2 t) \sin(\omega_n t) dt \tag{5.46}$$

There are two ways to make ϵ_1 and ϵ_2 approach zero. The first is

$$\bar{\epsilon}_1, \bar{\epsilon}_2 \to 0 \text{ as } \frac{A_2}{A_1} \to 0 \tag{5.47}$$

According to the principles of the moving block method, if ω_n, ω_2 are well separated and block length is properly chosen, then we have $\bar{\epsilon}_1$, $\bar{\epsilon}_2 \approx 0$.

For ω_n, ω_2 are very close, $\bar{\epsilon}_1$ and $\bar{\epsilon}_2$ cannot be ignored, so that damping identification is not accurate.

5.4.3 Wavelet Transform

The rotor stability test data is again

$$y(t) = A_1 e^{-\zeta\omega_n t} \cos(\omega_n t + \phi_1) + A_2 \cos(\omega_2 t) \tag{5.48}$$

The wavelet transform of $y(t)$ is

$$W_y(a_1, b) = \sqrt{a_1} A_1 e^{-\zeta\omega_n t} e^{(-a_1\omega_n - \omega_0)^2} e^{j\omega_n b} + \sqrt{a_1} A_2 e^{(-a_1\omega_2 - \omega_0)^2} e^{j\omega_2 b} \tag{5.49}$$

If ω_n, ω_2 are well separated, we can choose $a_1 = \frac{\omega_n}{\omega}$ then $e^{(-a_1\omega_n - \omega_0)^2} = 1$ and $e^{(-a_1\omega_2 - \omega_0)^2} \approx 0$

So the desired transform is

$$W(a_1, b) = \sqrt{a_1} A_1 e^{-\zeta\omega_n t} e^{-a_1\omega_n - \omega_0)^2} e^{j\omega_n b} \tag{5.50}$$

The error is defined as

$$\epsilon(W) = \sqrt{a_1} A_2 e^{(-a_1\omega_2 - \omega_0)^2} e^{j\omega_2 b} \tag{5.51}$$

The normalized error with respect to A_1 is

$$\bar{\epsilon}(W) = \sqrt{a_1}\frac{A_2}{A_1}e^{-a_1\omega_2-\omega_0)^2}e^{j\omega_2 b} \tag{5.52}$$

The conditions to make $\bar{\epsilon}(W) \to 0$ are $\frac{A_2}{A_1} \to 0$ or $e^{(-a_1\omega_2-\omega_0)^2} \to 0$

From the error analysis we made above, we can see that there are two conditions which influence the envelop estimation error: the amplitude ratio and the frequency separation. Since it is difficult to estimate the errors analytically, we will use numerical methods to estimate the influences of the two conditions. In the next section, we will assess the effects of the two factors using simulation data.

The other error sources are noises. We use least square curve fitting to reduce the effect of noise.

5.5 Linear Damping Identification in Helicopter Rotors Using the Three Methods

In this section, we will evaluate the three damping identification algorithms using simulated rotor stability test data. Two effects are considered here: effect of amplitude ratio between 1/rev excitation and initial amplitude of lag/rev and the effect of frequency separation between 1/rev and lag/rev.

5.5.1 Effect of Amplitude Ratio

Since in hover stand test the amplitude ratio between 1/rev excitation and initial amplitude of lag/rev is low, however, in forward flight test the amplitude ratio is high, we need evaluate the effect of changing of the amplitude ratio to the

damping identification accuracy. In the simulation, we set lag damping is varied as 1%, 2%, and 5% in order to evaluate the ability to identify the high damping level($\zeta \geq 5\%$ damping) as well as low damping level($\zeta \leq 2\%$). The lag/rev frequency is set to 3.5 Hz and 1/rev frequency 5 Hz. The amplitude ratio is changing from 0 to 5. And in simulation data the sampling frequency is 256 Hz, and the data length is 10 seconds.

In addition, 5% and 10% noise is added to the signal to simulate the lag mode response in actual engineering environments and to evaluate the effect of noise. The noise is considered as Gaussian white noise. In this study, 5% noise implies that the variance of the noise is 5% of the initial amplitude of the transient being studied. We only include in our analysis that part of the transient response that exceeds a cutoff threshold, such that the low SNR tail of the transient response is not considered. Introducing cutoff keeps the high SNR part of signal and gets rid of the low SNR part of signal, therefore the influence of noise is minimized. It is important to note, however, that sufficient the signal must be used to accurately identify the envelope geometry. We typically use a threshold of between $20-30\%$ of the initial amplitude

The results of effect of amplitude ratio are show in Fig. 5.2 to Fig. 5.4. From the figures, we can see that the accuracy of the Hilbert damping estimates decrease as the amplitude ratio increases. At low damping levels, where the amplitude ratio is greater than 20%, the Hilbert algorithm cannot produce accurate estimates. At high damping levels, the Hilbert algorithm can accurately estimate damping only if at the amplitude ratio equals zero, i.e., the isolated mode case. FSMB/Hamming algorithm can accurately estimate damping at low damping levels. But at high damping levels, estimation error of FSMB/Hamming

algorithm becomes unacceptable. The wavelet transform gives consistent and accurate results for this case.

5.5.2 Effect of Frequency Separation

Another factor to consider is the effect of frequency separation between 1/rev and lag/rev on damping identification results. To evaluate the effect of spectral separation and damping level on the three algorithms, the difference between the frequencies of the lag/rev and 1/rev, expressed in nondimensional form, $\frac{\Delta\omega}{\Omega} = \frac{\Omega - \Omega_{lag}}{\Omega}$ is varied from 0.02 to 0.5. The damping of 1/rev is still set to zero since 1/rev signal is persistent excitation. The frequency of the 1/rev is set to 5 Hz, and the amplitude ratio is set to 1.

The results are shown in Fig. 5.5 and Fig. 5.6. Since the Hilbert transform is not suitable for this case, we only show the results of the FSMB and the wavelet transform. The results of the FSMB and wavelet transform are shown in Fig. 5.5 and Fig. 5.6. For FSMB, we can see when damping is low and the frequency difference ratio is greater than 0.1, the estimation results are accurate. But when damping is high, the result of FSMB is not satisfied. The estimation error is quite large when $\frac{\Delta\omega}{\Omega} < 0.2$. Compared to FSMB, the wavelet transform reaches a comparable results in low damping cases and better results on high damping case. When damping is high, as long as the frequency difference ratio is larger than 0.12, the estimated dampings are accurate and consistent.

The problem is that when the lag/rev response and 1/rev excitation signal are spectrally very close, say, the difference ratio less than 0.2, both the FSMB method and wavelet transform method are not stable as damping level changes. To solve this problem, a new method called the hybrid method is developed in

next section.

5.6 Hybrid Methods

In last section we show that for hover stand test data, i.e., when the amplitude of 1/rev signal is much less than the amplitude of lag/rev response, all of the three method work well. For forward flight test data, because the amplitude of 1/rev is comparable to the amplitude of 1/rev, the Hilbert transform fails, and both the FSMB method and wavelet transform work only if the 1/rev and lag/rev are well separated, and the performance of FSMB is not good for high damping case. A more robust damping identification algorithm called the hybrid algorithm is developed. Instead of identify lag/rev damping directly from the total response, such as what is done when using FSMB and wavelet transforms, the hybrid method removes the 1/rev persistent excitation first, creates a the residual signal containing only the lag/rev response, so that the damping identification is straightfroward.

The undamped signal is determined by its natural frequency, amplitude and natural frequency. For 1/rev excitation, its natural frequency is known. If we can identify its amplitude and initial phase, we can reconstruct the signal and remove it from the original signal.

The FSMB method is suitable to this work. If the signal is undamped, the FSMB is not approximate any more. It is the exact calculation. If the signal is undamped, say

$$y(t) = A\cos\Omega t + B\sin\Omega t \tag{5.53}$$

where A and B are constant. then

$$A = A_1(t_k) = \frac{\Omega}{\pi N_c} \int_{t_k}^{t_k + \frac{2\pi N_c}{\Omega}} x(t) \cos(\Omega t) \mathrm{d}t \tag{5.54}$$

$$B = B_1(t_k) = \frac{\Omega}{\pi N_c} \int_{t_k}^{t_k + \frac{2\pi N_c}{\Omega}} x(t) \sin(\Omega t) \mathrm{d}t \tag{5.55}$$

the amplitude of y(t) is

$$a = \sqrt{A^2 + B^2} \tag{5.56}$$

the phase of y(t) is

$$\phi = \arctan\left(\frac{A}{B}\right) \tag{5.57}$$

A Hamming window is used in this procedure to reduce the leakage. To remove the effect of the Hamming window on the identified amplitude, a constant is multiplied to the amplitude. The detail proof is shown in [95].

By carefully choosing the block length and using Hamming window, the leakage can be reduced to an acceptable level as we discussed in last section. The amplitude and initial phase of the undamped signal can be identified using the FSMB method then. The undamped signal can be reconstructed with the identified amplitude and initial phase, and the known natural frequency. The damped signal can be extracted from the original signal. The damping of the signal then can be identified by any of the three methods we mentioned before. Here, we choose the Hilbert transform and wavelet transform for comparison.

5.6.1 Hybrid FSMB/Hilbert Algorithm

Considering the computation procedure of Hilbert damping analysis in frequency domain presented before, we can consider using the FSMB with Hamming Window as a filter, insert the filter to the frequency domain computation procedure

of Hilbert transform to remove the spurious 1/rev excitation and extract residual lag/rev mode. The diagram of the hybrid FSMB/Hilbert algorithm is shown in Fig. 5.7 (a).We can also insert a traditional band pass filter to remove the spurious modes and noise which are spectrally far from the lag/rev mode.

To explain the algorithm clearly, we use the generate a typical forward flight test data as an example. The procedure and results are shown in Fig. 5.8. Fig. 5.8 a) shows the raw data, which includes the lag/rev model response and the persistent excitation at 1/rev signal. Fig. 5.8 b) shows the FFT of the data. Fig. 5.8 c) is the extraction of the lag/rev mode. Using Hilbert transform, the envelope of the lag/rev mode can be computed, which is shown in Fig. 5.8 d).

Then we apply the hybrid FSMB/Hilbert algorithm to the set of the simulated test data in last section to evaluate the effect of the frequency difference and the damping level. The result is show in Fig. 5.9. The estimated damping results are consistent except when $\frac{\Delta\omega}{\Omega} = 0.02$. Compared to the corresponding results of FSMB and wavelet transform, much improvement is achieved when the frequency difference is small and the damping is high.

5.6.2 Hybrid FSMB/Wavelet Algorithm

Another hybrid approach can be developed is that use of wavelet transform to estimate damping of the residual lag/rev mode damping. The benefit of using wavelets is that if there are spurious modes and noise which are spectrally far from the lag/rev mode, the wavelet transform can isolate the lag/rev mode from them. The extra band pass filter is not necessary. The procedure of the hybrid FSMB/Wavelet algorithm is similar to the hybrid FSMB/Hilbert transform except that the Hilbert transform is replaced by the wavelet transform. The

diagram of hybrid FSMB/wavelet technique is shown in Fig. 5.7 (b).

The hybrid FSMB/wavelet algorithm is applied to the same simulated test data used in last section for the effect of frequency separation. The result is shown in Fig. 5.10. Again, we can see that performance achieved is better than that of using FSMB or wavelet transform alone. The frequency resolution is best at 4%, and the noise has little effect on the method. Compared to the result of hybrid FSMB/Hilbert method, the hybrid FSMB/wavelet method has better performance at high damping levels.

5.7 Application to Experimental Data

We applied the above methods to an experimental forward flight test data sample. The Hilbert transform is not suitable for forward flight test data, hence, is not considered. The data comes from NRTC wind tunnel test data. Sampling rate is 256 Hz. Data length is 2 seconds. Rotational speed is 660 RPM (11 Hz), and lag/rev frequency is 7.5 Hz. Before apply the algorithm to the data, we did some pre-process. The data is not symmetric about zero, we need to remove the steady state offset and reset the new steady state of the response to zero, i.e., remove the DC offset.

A representative transient signal (after pre-processing) is shown in Fig. 5.11 and the corresponding FFT is shown in Fig. 5.12. It can be seen from the transient and FFT that the signal contain both noise and a spectrally close mode as well as other modes, which are small and can be neglected. The amplitude of the 1/rev mode signal is compatible to the lag/rev mode in amplitude. The separation of the two modes is 3.5 Hz. These parameters are all well within

Table 5.2: Results for Experimental Forward Flight Test Data

	Lag/rev Damping
FSMB	1.55%
Wavelet Transform	1.55%
Hybrid FSMB/Wavelet Method	1.58%

the acceptable range for application of the hybrid damping identification algorithms developed in this paper as well as FSMB method and wavelet transform method. We use the FSMB with Hamming window, wavelet transform, and hybrid FSMB/Wavelet method to identify the lag damping from the data set. Fig. 5.11 also shows the identified and fitted envelope from the three algorithms. The decay tendency of the three envelope is almost same. The three methods give consistent results, which are shown in Table 4. This example verifies that the hybrid method can get accurate damping estimates from forward flight test data.

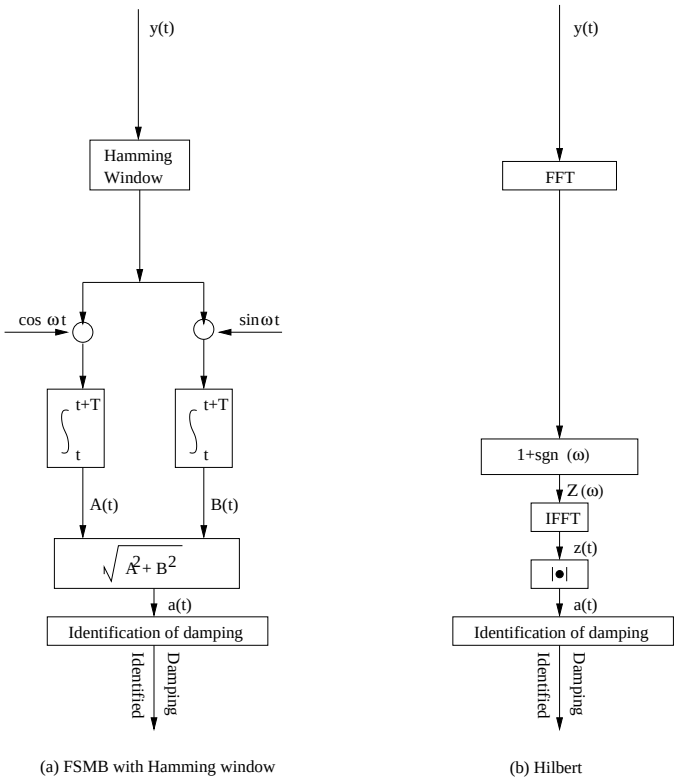

Figure 5.1: Diagram of FSMB with Hamming window and Hilbert transform

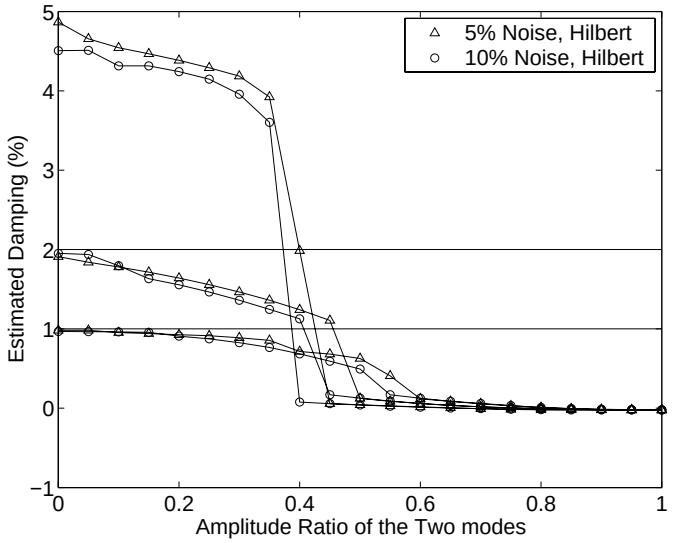

Figure 5.2: Effect of amplitude ratio on Hilbert transform

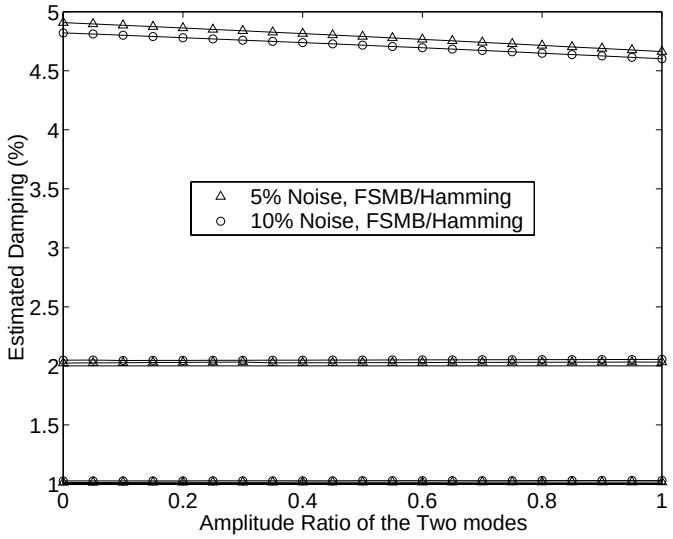

Figure 5.3: Effect of amplitude ratio on FSMB with Hamming window

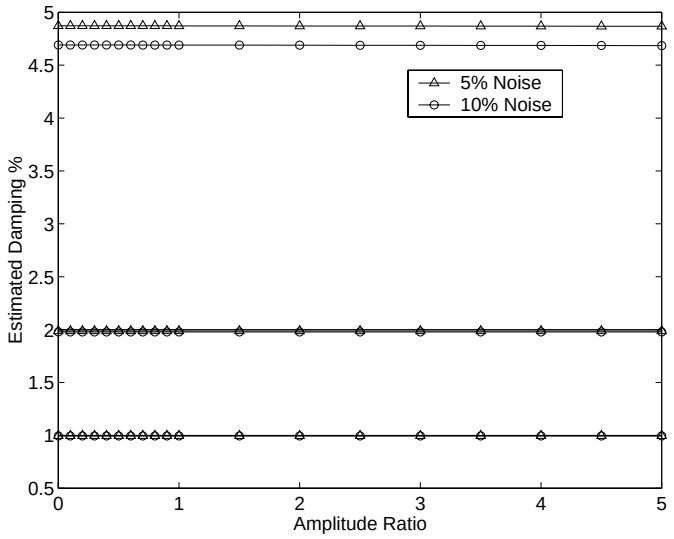

Figure 5.4: Effect of amplitude ratio on wavelet transform

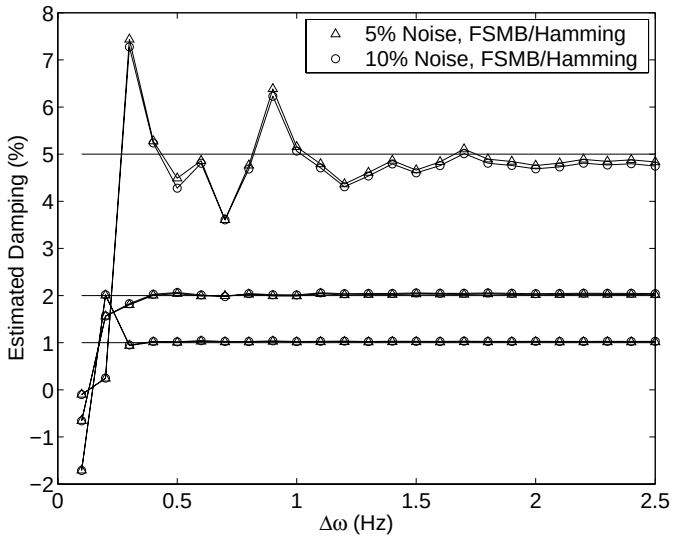

Figure 5.5: Effect of frequency difference on FSMB with Hamming window

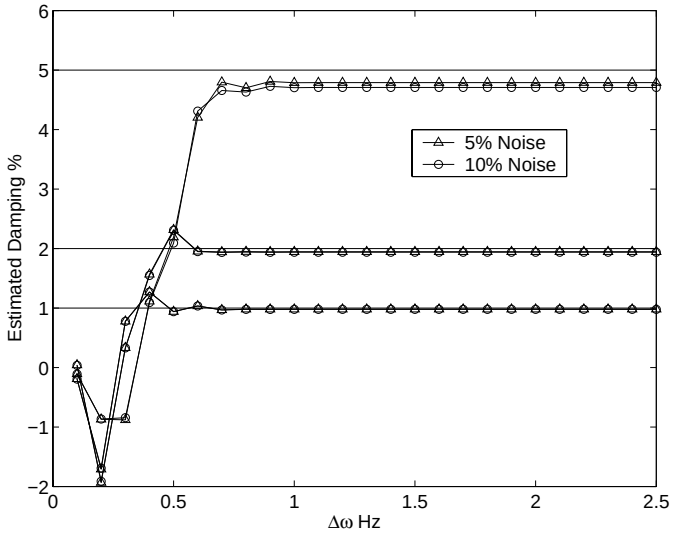

Figure 5.6: Effect of frequency difference on wavelet transform

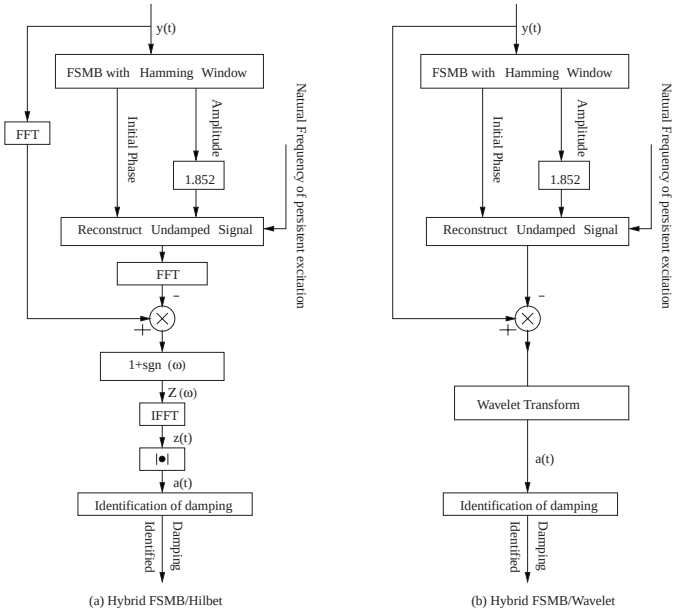

Figure 5.7: Diagram of hybrid methods

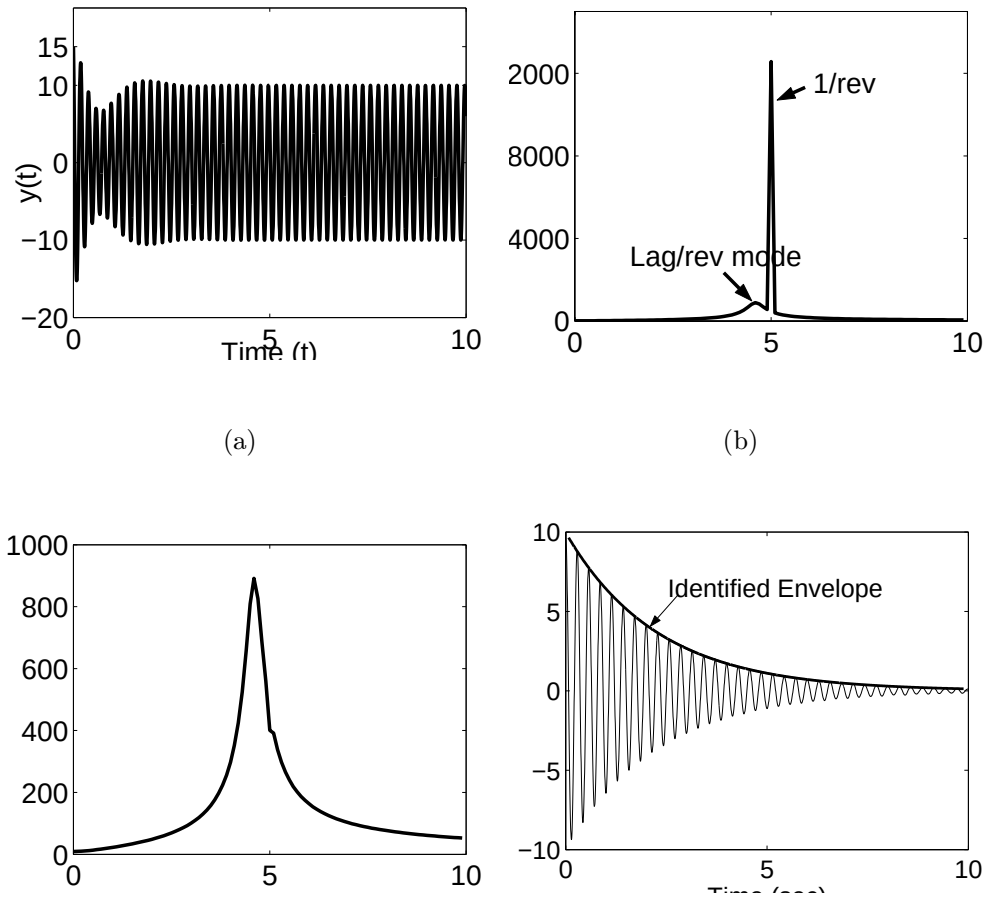

(a) (b)

(c) (d)

Figure 5.8: Applying hybrid method to forward flight test data

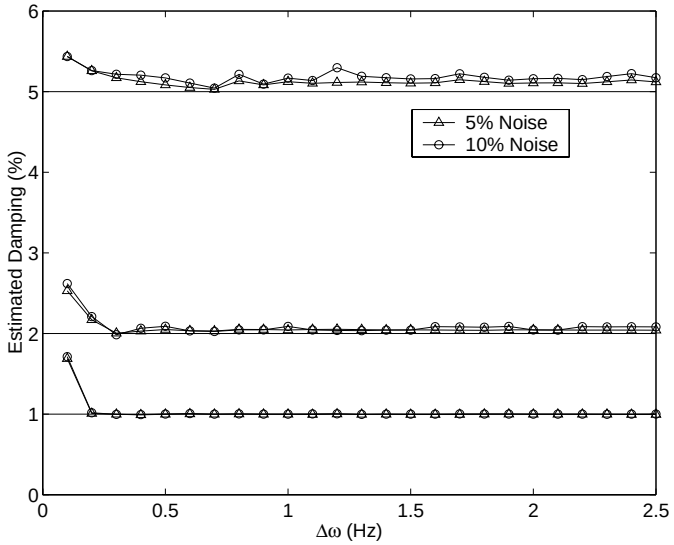

Figure 5.9: Effect of frequency difference on hybrid FSMB/Hilbert algorithm

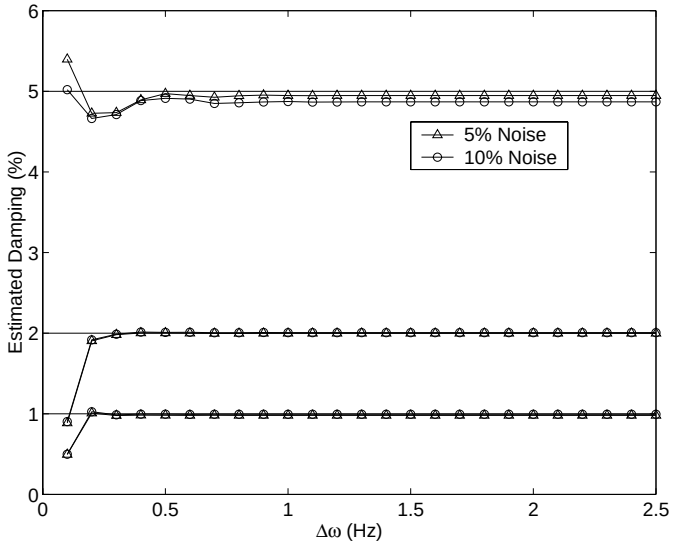

Figure 5.10: Effect of frequency difference on hybrid FSMB/Wavelet algorithm

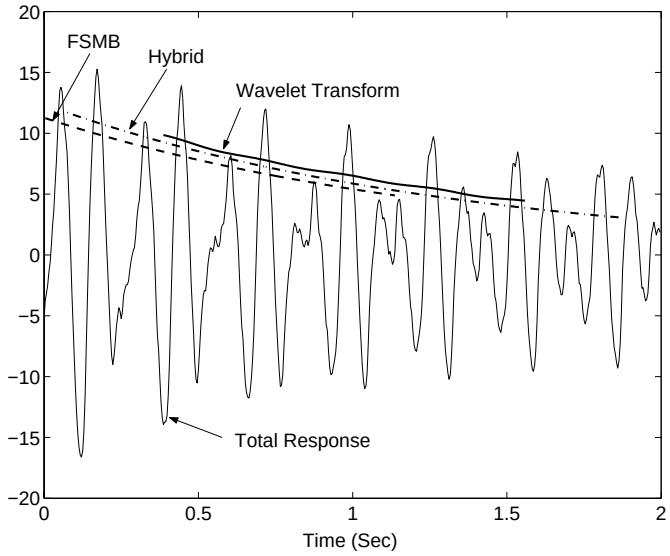

Figure 5.11: Sample Data from Forward Flight Test

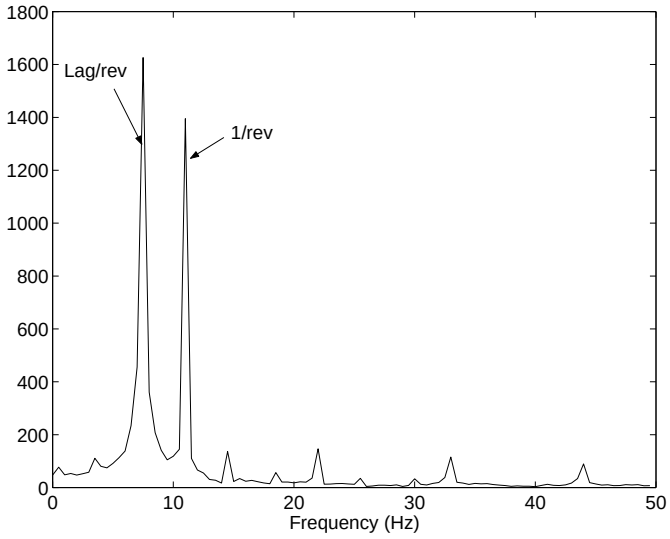

Figure 5.12: FFT analysis of the Forward Flight Test Data

Chapter 6

Nonlinear Damping Identification for Systems Using ER/MR Dampers

Smart materials are widely applied in aerospace industries because of their ability to change the properties of structures such as stiffness and damping by applied fields. Electrorheological (ER) and magnetorheological (MR) fluids belong to the class of smart materials. They have unique ability to change the damping of systems when electric or magnetic field is applied. These controllable fluids have received considerable attention as components of engineering devices such as valves, clutches, brakes, suspensions, and dampers[87]. In helicopters, the MR based dampers have been proposed primarily for damping augmentation of the rotor systems[76]. These smart structural systems present nonlinear behaviors when the field is applied in the damper. Recent studies on MR and ER dampers suggested that a combined viscous and Coulomb damping characteristic is manifested as the field applied to the MR fluid is maximized[18]. An accurate and reliable method for identifying nonlinear damping mechanisms is needed to evaluate the damping performance of these systems.

Previous research into ER and MR dampers has shown many methods of

modeling the fluid characteristics and the resulting damping forces. The most widely applied model is the Bingham plastic model. At the fluid level, the Bingham plastic model assumes a Newtonion fluid with a non-zero yield stress. At the damper level, the damper force becomes essentially a yield or Coulomb force added to a linear viscous damping force, which can be viewed as combined viscous and Coulomb damping.

Several studies have focused on identifying the combined viscous and Coulomb damping[89, 90, 91]. The proposed method used in these papers is similar to the logarithmic decrement method and is called the decrement method[91]. The exact solution of the free vibration was used in this method. The relationship between peak and valley points of the free vibration was determined from the exact solution. The viscous and Coulomb damping can then be calculated from this relationship. Unfortunately, the decrement method suffers greatly from the measurement error and noise.

In this chapter, we develop another approach which identifies the combined viscous and Coulomb damping simultaneously from the envelope of the transient data record. First we derive the envelope of the free response of the system with combined viscous/Coulomb damping and show that the viscous and Coulomb damping ratio can be identified simultaneous from the envelope. Then the envelope estimators, including Hilbert transform, FSMB, and wavelet transform, are presented and applied. A SDOF mass-spring-damper system is simulated and the three methods are evaluated using this system by varying the viscous and Coulomb damping ratio.

6.1 Bingham Plastic Model of ER and MR Dampers

ER and MR dampers are typically modeled using an idealized Bingham plastic model [76]. When the force applied to the damper is below a threshold, called the yield force, F_y, the damper is rigid. However, once the force applied to the damper exceeds the yield force, the damper behaves as a Newtonian or viscous damper offset by this yield force. The Bingham plastic model can be expressed as

$$F(\dot{x}) = F_y \text{sign}\,(\dot{x}) + c\dot{x} \tag{6.1}$$

where F_y is the dynamic yield force and c is the post-yield damping. The Bingham plastic model can be viewed as the sum of a viscous force, $c\dot{x}$, and Coulomb force, F_y.

6.2 Equation of the Envelope

Consider a SDOF mass spring system with ER or MR damper. Without the external force, the equation of motion is

$$m\ddot{x} + c\dot{x} + F_y \text{sign}(x) + kx = 0 \tag{6.2}$$

Let $\omega_n^2 = k/m$, $2\zeta\omega_n = c/m$, and $\mu = F_y/m$. Eqn. 6.2 can be rewritten as

$$\ddot{x} + 2\zeta\omega_n\dot{x} + \omega_n^2 x + \mu \text{sign}(x) = 0 \tag{6.3}$$

To solve Eqn. 6.3, we apply the method of slowly varying parameters developed by Kryloff and Bogoliuboff, as presented by Nayfeh [96].

Suppose the solution can be written as

$$x(t) = a(t)\cos(\omega_n t + \phi) \tag{6.4}$$

where $a(t)$ and ϕ are slowly varying functions of time t.

Let

$$\omega_n t + \phi = \theta \tag{6.5}$$

Differentiating Eqn. 6.4 with respect to t

$$\dot{x}(t) = -\omega_n a(t)\sin\theta + \dot{a}(t)\cos\phi - a(t)\dot{\phi}\sin\theta \tag{6.6}$$

Since $a(t)$ and ϕ are slowly varying, we have that

$$\dot{a}(t)\cos\theta - a(t)\dot{\phi}\sin\theta = 0 \tag{6.7}$$

Differentiation Eqn. 6.6 with respect to t, we have

$$\ddot{x}(t) = -\omega_n^2 a(t)\cos\theta - \omega_n\dot{a}(t)\sin\theta - \omega_n a(t)\dot{\phi}\cos\theta \tag{6.8}$$

Substituting for $\dot{x}(t)$ and $\ddot{x}(t)$ into Eqn. 6.3 yields

$$\omega_n\dot{a}(t)\sin\theta + \omega_n a(t)\dot{\phi}\cos\theta = -2\zeta\omega_n^2 a(t)\sin\theta + \mu\text{sign}(\dot{x}) \tag{6.9}$$

Solving Eqn. 6.7 and 6.9 for $\dot{a}(t)$ and $\dot{\phi}$, we obtain

$$\dot{a}(t) = -\frac{1}{\omega_n}\sin\theta\left[-2\zeta\omega_n^2 a(t)\sin\theta + \mu\text{sign}(\dot{x})\right] \tag{6.10}$$

$$\dot{\phi} = -\frac{1}{\omega_n a(t)}\cos\theta\left[-2\zeta\omega_n^2 a(t)\sin\theta + \mu\text{sign}(\dot{x})\right] \tag{6.11}$$

Since $a(t)$ and ϕ are by assumption slowly varying, averaging Eqn. 6.10 and Eqn. 6.11 over one cycle of θ yields

$$\begin{aligned} \dot{a}(t) &= -\frac{1}{2\pi\omega_n}\int_0^{2\pi}\sin\theta f(\dot{x})d\theta \\ &= -\frac{2\mu}{\omega_n} - \zeta\omega_n a(t) \end{aligned} \tag{6.12}$$

$$\begin{aligned}\dot{\phi} &= -\frac{1}{\omega_n a(t)}\int_0^{2\pi}\cos\theta f(\dot{x})d\theta \\ &= 0\end{aligned} \tag{6.13}$$

where

$$f(\dot{x}) = -2\zeta\omega_n^2 a(t)\sin\theta + \mu\text{sign}(\dot{x}) \tag{6.14}$$

Solving Eqn. 6.13 and 6.14 with the initial condition $a(0) = a_0$ and $\phi(0) = \phi_0$, we obtain

$$a(t) = -\frac{2\mu}{\pi\omega_n^2\zeta} + \left(a_0 + \frac{2\mu}{\pi\omega_n^2\zeta}\right)e^{-\zeta\omega_n t} \tag{6.15}$$

and

$$\phi = \phi_0 \tag{6.16}$$

Then the solution of Eqn. 6.3, that is, the free response of the system, is

$$x(t) = a(t)\cos(\omega_n t + \phi_0) \tag{6.17}$$

The envelope of the free response is defined by Eqn. 6.15.

Having the envelope, we have several ways to solve for the viscous and Coulomb damping ratio. One way is to take the derivative of Eqn. 6.15

$$\dot{a}(t) = -\zeta\omega_n(a_0 + \frac{2\mu}{\pi\omega_n\zeta})e^{-\zeta\omega_n t} \tag{6.18}$$

$$ln|\dot{a}(t)| = -\zeta\omega_n t + A \tag{6.19}$$

where

$$A = ln[\zeta\omega_n(a_0 + \frac{2\mu}{\pi\omega_n^2\zeta})] \tag{6.20}$$

The slope of $ln|\dot{a}(t)| = -\zeta\omega_n t$, then

$$\zeta = \frac{slope}{-\omega_n t} \tag{6.21}$$

Having ζ, we obtain μ as

$$\mu = \frac{-a(t) + a_0 e^{-\zeta\omega_n t}}{2(1 - e^{-\zeta\omega_n t}} \pi\pi\omega_n^2\zeta \tag{6.22}$$

or as

$$\mu = \frac{\pi\omega_n^2\zeta}{2}\left[\frac{B}{\zeta\omega_n} - a_0\right] \tag{6.23}$$

where

$$B = e^A = \zeta\omega_n(a_0 + \frac{2\mu}{\pi\omega_n^2\zeta}) \tag{6.24}$$

The drawback of this method is that the derivative of $a(t)$ will introduce additional noise so that the result will be inaccurate.

Another way is using a parameter optimization method to estimate ζ and μ directly. In this paper we use parameter optimization to choose the optimal ζ and μ so that the error between estimated envelope and measured envelope is minimized in the sense of least square error.

Now the damping identification problem is reduced to an envelope identification problem.

Having identified viscous damping ζ and Coulomb damping μ, the equivalent viscous damping can be calculate as

$$\zeta_{eq}(t) = \zeta + \frac{2\mu}{\omega_n^2 a(t)} \tag{6.25}$$

where a(t) is the envelope described by Eqn. 6.15.

6.3 Numerical Analysis of Isolated Mode

To evaluate the methods proposed in this chapter, we generate a spring mass system with combined viscous and Coulomb damping as shown in Eqn. 6.3 with ω_n=3.5 Hz, $\zeta = 0.004$, and $\mu = 2$, as a low damping example, and $\zeta = 0.015$, $\mu = 16$ as a high damping example. The equation is solved numerically to get the free response by setting $x_0 = 10$ and $\dot{x}_0 = 0$. The sampling frequency is set to 1024 Hz. For the low damping example, the transiet response and its theoretical envelope are shown in Fig. 6.1. The envelope signals identified by each of the three methods (Hilbert, FSMB, and wavelet) are shown in Fig. 6.2. The identified envelopes are similar. The results of low damping case are show in Table 6.2 and Fig. 6.3 show the equavalent viscous damping calculated from Eqn. 6.25 for low damping case. Table 6.2 shows the identified damping for high damping case and Fig. 6.4 the equivalent viscous damping. The results are very satisfactory for these conditions.

We then evaluate the three methods by varying the viscous damping ratio ($0.1\% \leq \zeta \leq 2\%$) and Coulomb damping ratio ($1 \leq \mu \leq 40$). The percent error contour plots are shown in Fig. 6.5 to Fig. 6.7, in which the err_ζ and err_μ are relative error and defined as

$$err_\zeta = \frac{|\hat{\zeta} - \zeta|}{\zeta} \times 100\% \tag{6.26}$$

$$err_\mu = \frac{|\hat{\mu} - \mu|}{\mu} \times 100\% \tag{6.27}$$

From the figures, we can see for all cases within these ranges, all three methods have good performance. The relative estimation errors are below 10%.

The identified Coulomb damping ratio when $\mu = 6$, with the varying viscous damping, is shown in Fig. 6.8. We can see that the results of the three methods

are quite good, though a little different. The FSMB tends to overpredict the Coulomb damping.

In engineering environment, the measurement error and noise are important factors that influence the estimation accuracy. To evaluate the effect of measurement error and noise, we add 5% Gaussian white noise to the response signal. Here 5% mean that the variance of the noise is 5% of the initial amplitude of the response signal.

Since the FSMB and wavelet transform have the ability to choose the desired frequency, they are less sensitive to noise than the Hilbert transform. To make the results comparable, we add a low pass filter when Hilbert transform was applied. Even so, the noise has dramatic influence on the three methods. Fig. 6.9 is the same computation as what was done in Fig. 6.8, except that 5% noise was added to the transient response. The noise increases the error, especially for low viscous damping. However, the results are in an acceptable range. The largest error is less than 10%.

The error contour plots are shown in Fig. 6.10 to Fig. 6.12. We can see the wavelet transform produces the best results for the system with 5% noise added. In most cases, the viscous damping estimation errors and Coulomb damping estimation errors are below 10%. The Hilbert transform with a low pass filter and the FSMB method result in comparable results.

6.4 Numerical Analysis For the Response with Close Modes

When a helicopter in forward flight, the periodic aerodynamic enviroment at the rotor disk leads to the generation of the forces on the blade consisting of harmonics of the rotational frequency. The resulting undamped response can be simulated by the addition of an undamped sinusoid to transient response data. In order to investigate the effect of forced response, an undamped sinusoidal signal was added to the transient response of the system with ER/MR dampers. As in the viscous case in Chapter 5, we will assess the fluences of amplitude ratio (defined as the ratio between the amplitude of 1/rev and the initial amplitude of lag/rev) and frequency separation (the frequency difference between the 1/rev and lag/rev) on the damping identifications. The three traditional methods (Hilbert transform, FSMB, and wavelet transform) in last chapter as well as the new method (hybrid method) developed in last chapter are used.

6.4.1 The Effect of Amplitude Ratio

In this section, we set the parameters of the signal as follows: the frequency of the lag mode is still 3.5 Hz, the frequency of 1/rev persistent excitation is set to 5 Hz; three damping levels are considered in this section: 6% viscous damping plus 6 Coulomb damping, 1% viscous damping plus 10 Coulomb damping, and 1.5% viscous + 18 Coulomb damping; the data length is set to 10 seconds, and the sampling rate is 1024 Hz, the amplitude ratio are set from 0 to 5 with increasement of 0.2 from 0 to 1 and increasement of 0.5 from 1 to 5.

The results of Hilbert transform are shown in Fig. 6.13 and Fig. 6.14. The

results show that when using the Hilbert transform, the combined viscous and Coulomb damping can be identified only when the initial amplitude of the lag mode is much less than the amplitude of 1/rev excitation. When the amplitude ratio of the 1/rev excitation increases, the Hilbert transform can identify neither the viscous nor Coulomb lag damping.

The results of FSMB with Hamming window are shown in Fig. 6.15 and Fig. 6.16. For the low amplitude ratio, the FSMB with Hamming window can identify both viscous and Coulomb damping very well. However, for the high amplitude ratio, the FSMB with Hamming window cannot get the accurate results for both viscous and Coulomb damping, especially for high damping level.

The results of the wavelet transform are shown in Fig. 6.17 and Fig. 6.18. In these cases, the wavelet transform can accurately identify both the viscous and Coulomb damping levels.

6.4.2 Effect of Frequency Separation

Last section we evaluated the effect of amplitude ratio. At low amplitude ratio, all three methods work well, however, at high amplitude ratio, only the wavelet transform can identify both viscous and Coulomb damping accurately. In this section, we will evaluate the effect of frequency separation on the damping identification accuracy. The signal parameters are set almost same as that in last section except that the amplitude ratio is set as 1 and the frequency separation ration is defined as $\frac{\Delta\omega}{\Omega} = \frac{\Omega - \Omega_{lag}}{\Omega}$ is varied from 0.02 to 0.5.

Since we already know that at high amplitude ratio, the Hilbert transform cannot identify the lag damping from the total response corrupted by the 1/rev

persistent excitation, we only evaluate the FSMB with Hamming window and wavelet transform.

The results of FSMB with Hamming window are shown in Fig. 6.19 and Fig. 6.20. First we can see that at these cases, the FSMB with Hamming window cannot identify the high damping level accurately, especially for the Coulomb damping. This result is consistent with the result of the effect of amplitude ratio. Second, for the low damping level, the frequency separation ratio must be larger than 0.3 to identify the viscous and Coulomb damping accurately.

The results of the wavelet transform damping analysis are shown in Fig. 6.21 and Fig. 6.22. To identify both viscous and Coulomb damping accurately using the wavelet transform, the frequency separation must be larger than 0.2.

6.4.3 Hybrid Method

Above results showed that all three traditional methods have their individual drawbacks. To improve the damping identification accuracy for spectrally close modes, again, the hybrid method is used. Since in the single mode case, the wavelet method showed the superior performance, the hybrid FSMB/Wavelet method is used. Again, in this method, first the high energy 1/rev persistent excitation signal is identified using FSMB with Hamming window, then it is removed from the total response, leaving a residual signal which is lag mode damped response. Damping identification using wavelet transform is straight forward.

To assess the performance of hybrid method on combined viscous Coulomb damping identification, the effects of ampitude ratio and frequency separation are evaluated. The signal parameters are same as previous sections. The results

of amplitude ratio are shown in Fig. 6.23 to Fig. 6.26 for without noise and with 5% noise cases. We can see that the performance of hybrid method does not change with the amplitude ratio change and the noise does not have much effect on the hybrid method. The results of frequency separation are shown in Fig. 6.27 to Fig. 6.30. The hybrid method can identify combined viscous and Coulomb damping accurately as long as the frequency separation is larger than 0.04. The noise does not influence the results.

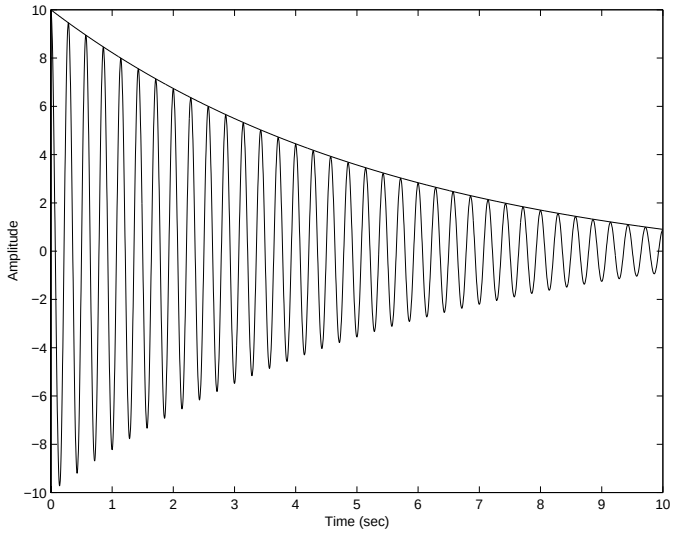

Figure 6.1: Free Response and Theoretic Envelope

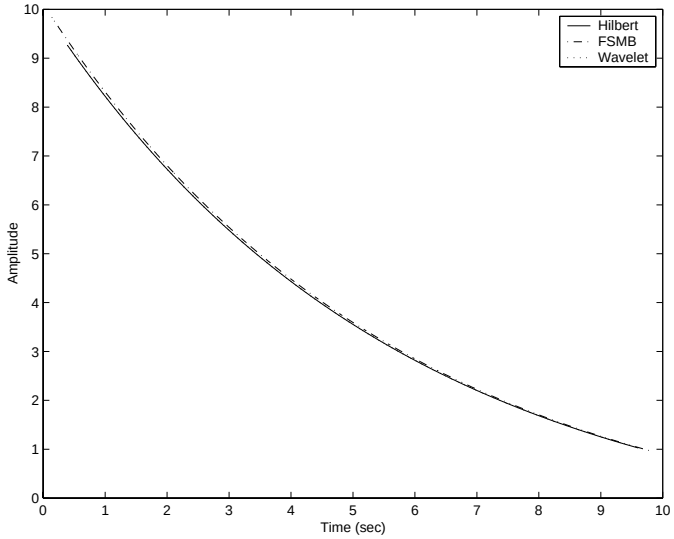

Figure 6.2: Envelope Identified By The Three Methods

Table 6.1: Damping Identification Results for Low Damping Case

	Viscous Damping	Coulomb Damping
Real Value	0.4%	2
HT	0.404%	1.98
FSMB	0.403%	2.03
WT	0.403%	2.03

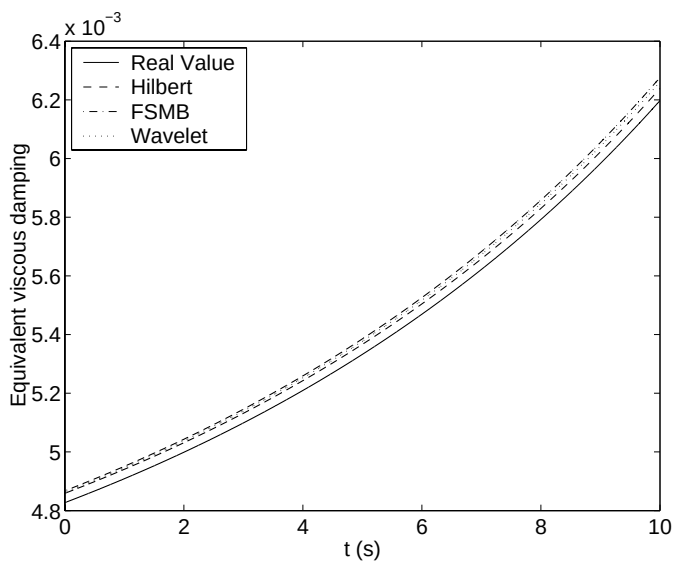

Figure 6.3: Equavalent viscous damping for low damping case

Table 6.2: Damping Identification Results for High Damping Case

	Viscous Damping	Coulomb Damping
Real Value	1.5%	16
HT	1.503%	16.04
FSMB	1.505%	15.95
WT	1.505%	15.95

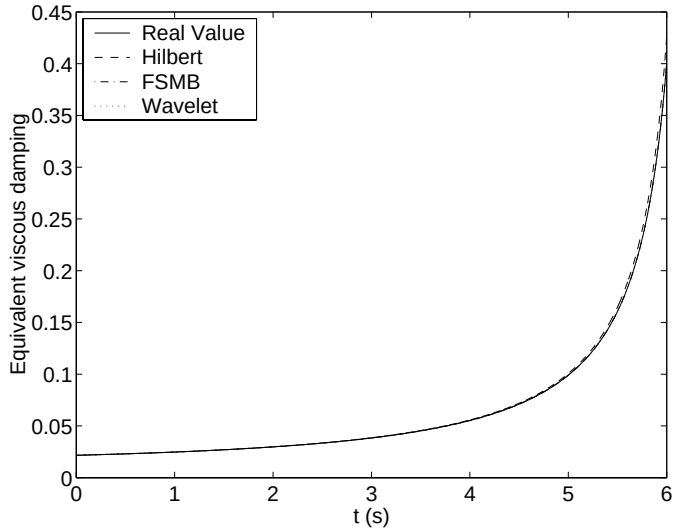

Figure 6.4: Equavalent viscous damping for low damping case

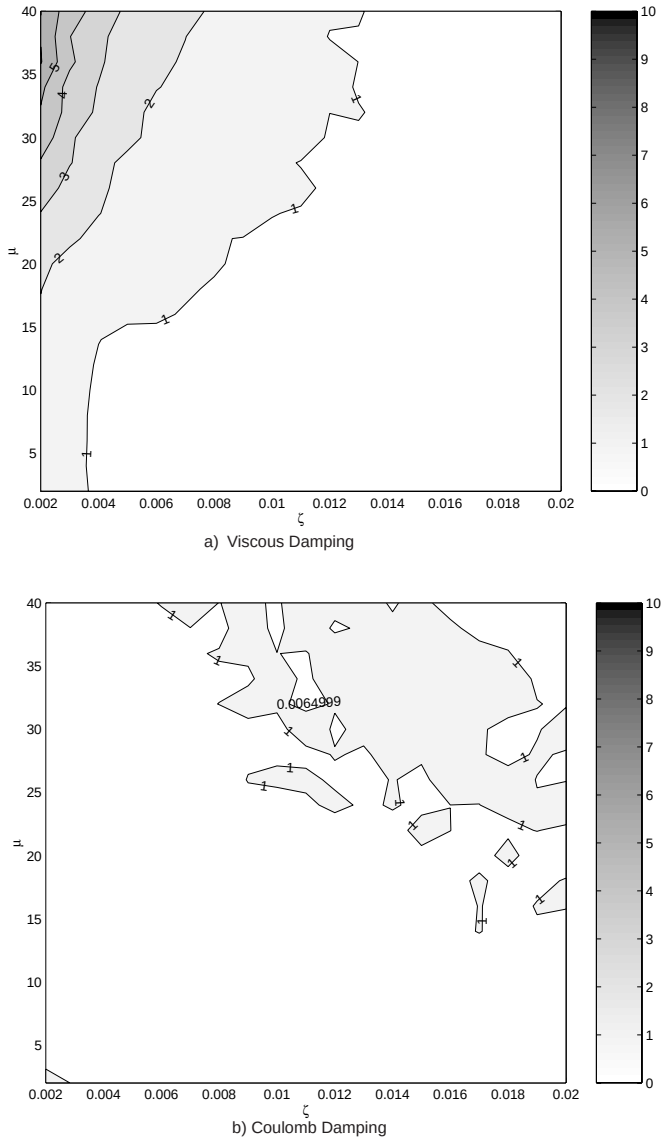

Figure 6.5: Damping Estimation Percentage Error Contour Using Hilbert Transform, No Noise Case

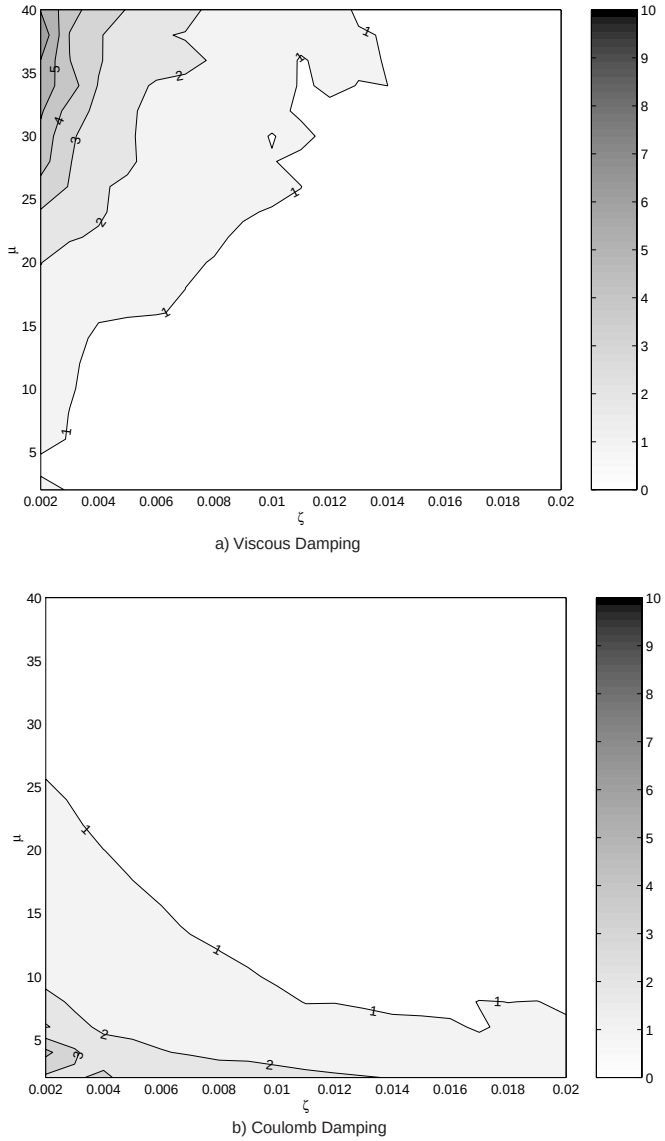

Figure 6.6: Damping Estimation Percentage Error Contour Using FSMB, No Noise Case

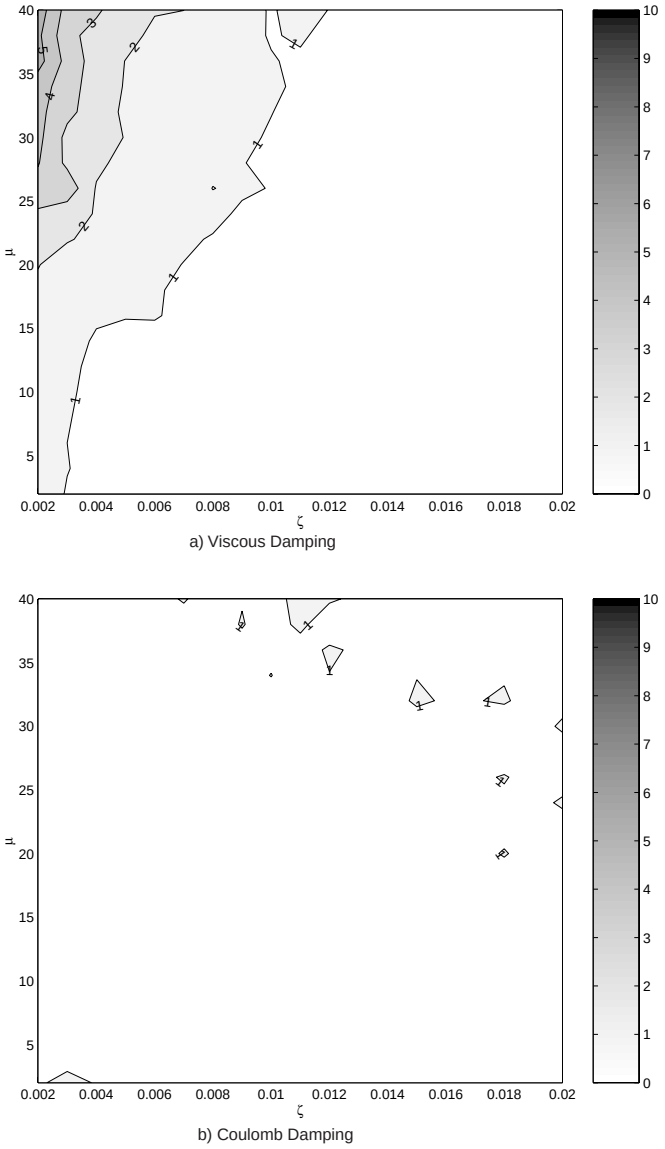

Figure 6.7: Damping Estimation Percentage Error Contour Using Wavelet Transform, No Noise Case

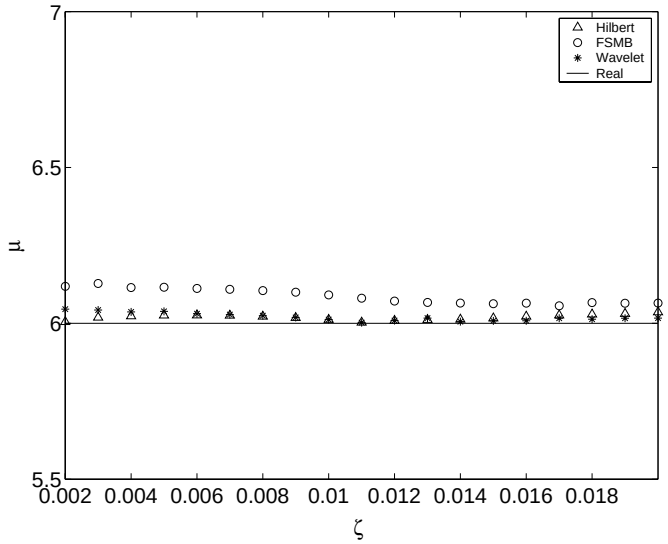

Figure 6.8: Coulomb Damping Estimation Result, No Noise Case

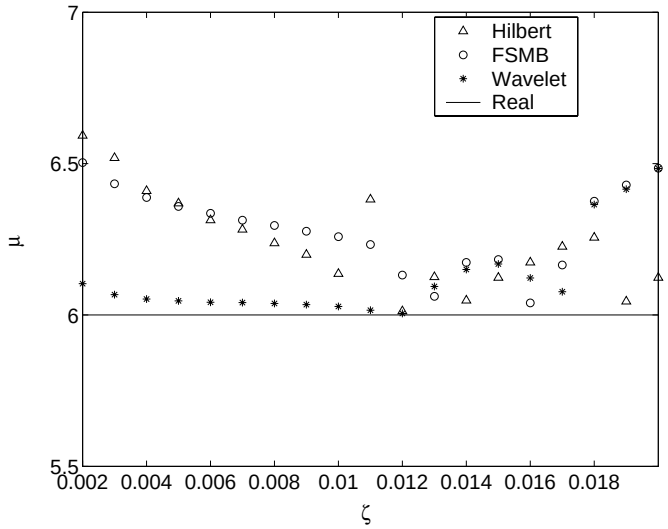

Figure 6.9: Coulomb Damping Estimation Result, with 5% Noise

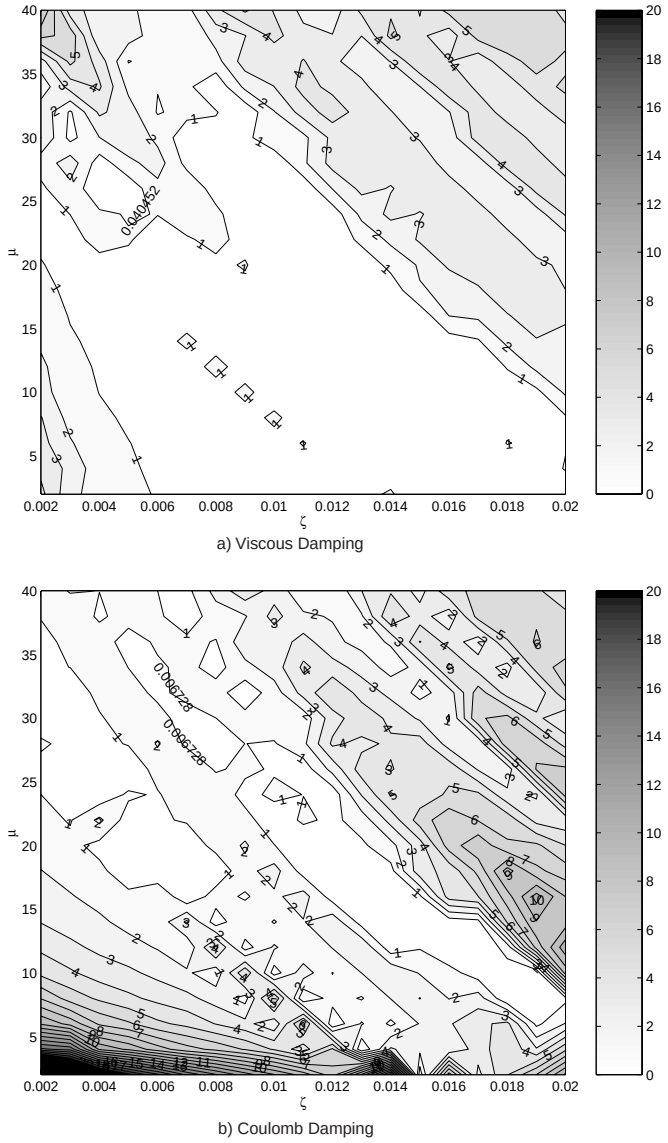

a) Viscous Damping

b) Coulomb Damping

Figure 6.10: Damping Estimation Percentage Error Contour Using Hilbert Transform, With 5% Noise Case

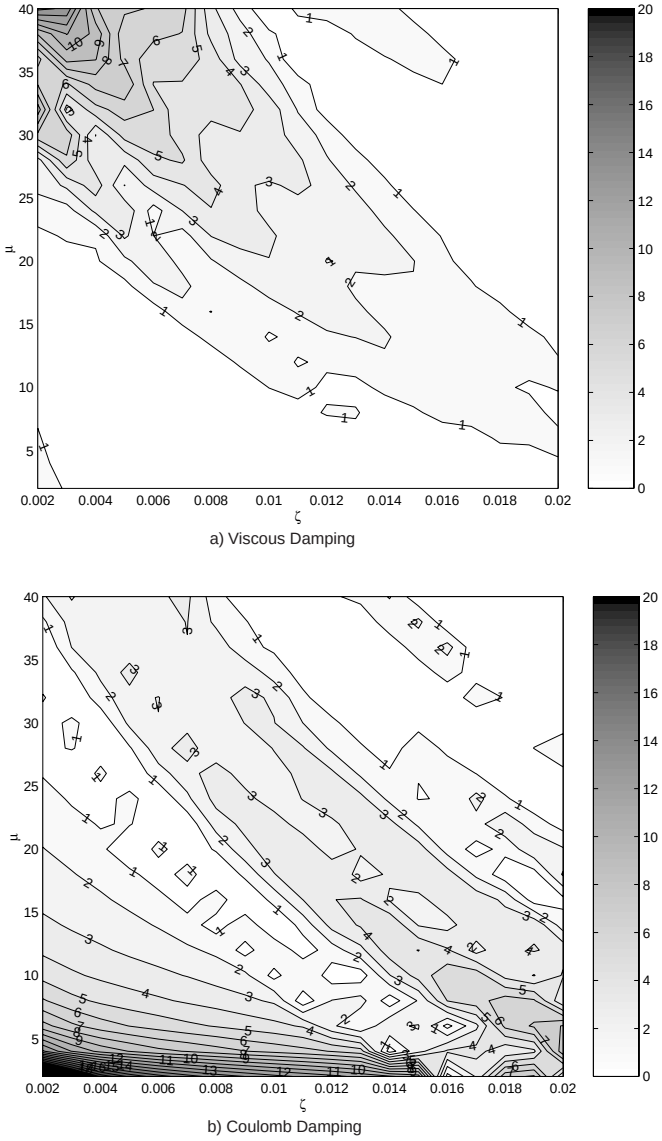

Figure 6.11: Damping Estimation Percentage Error Contour Using FSMB, With 5% Noise Case

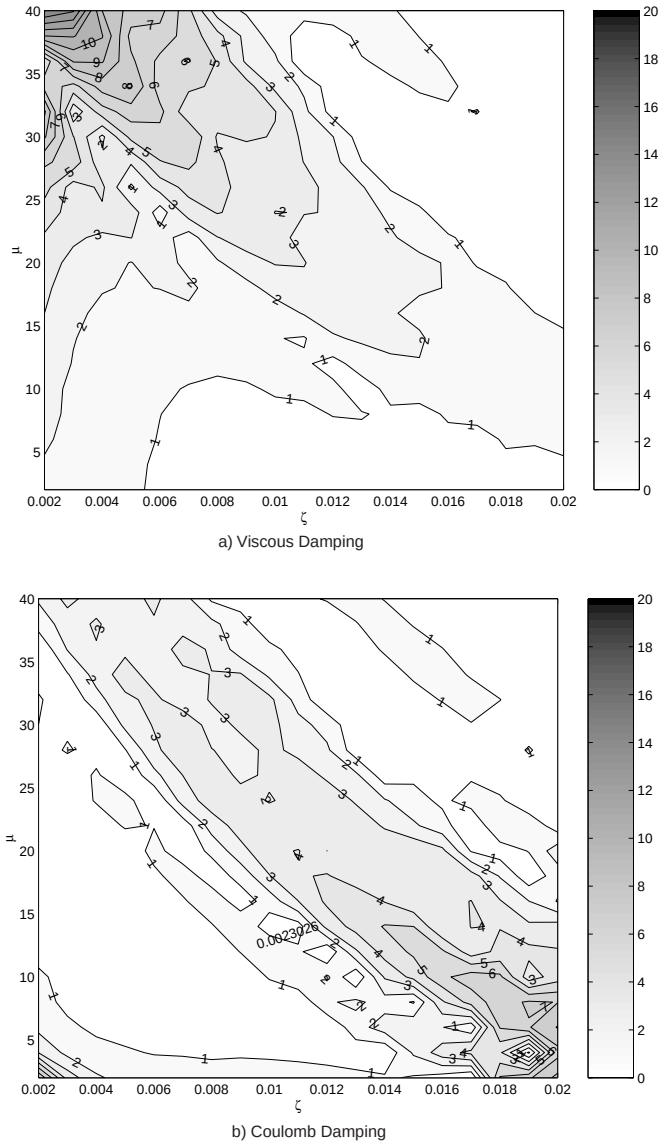

a) Viscous Damping

b) Coulomb Damping

Figure 6.12: Damping Estimation Percentage Error Contour Using Wavelet Transform, With 5% Noise Case

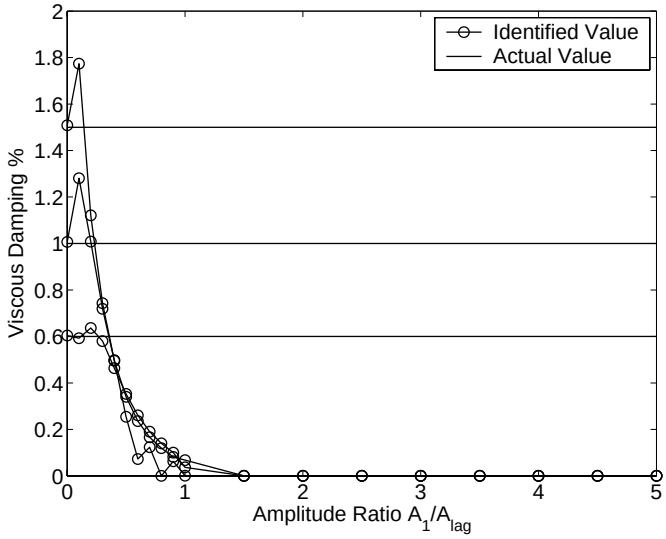

Figure 6.13: Effect of Amplitude Ratio on Viscous Damping Estimation Using Hilbert Transform

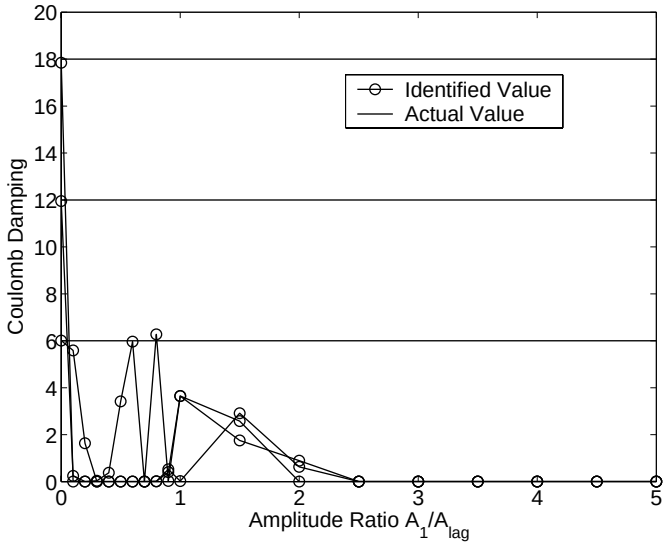

Figure 6.14: Effect of Amplitude Ratio on Coulomb Damping Estimation Using Hilbert Transform

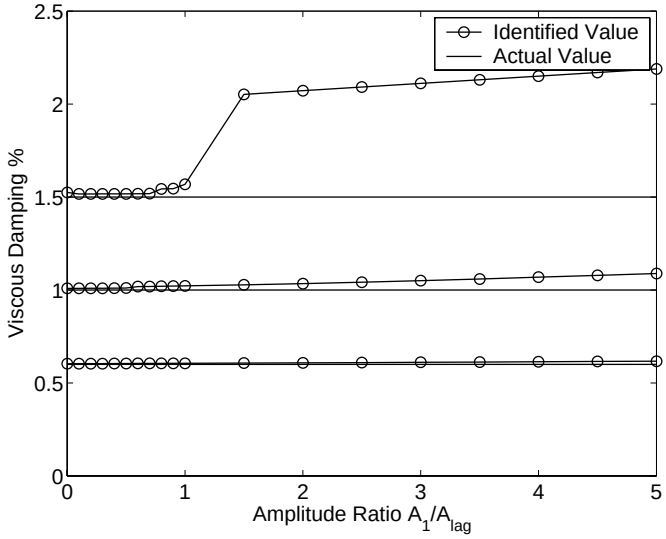

Figure 6.15: Effect of Amplitude Ratio on Viscous Damping Estimation Using FSMB

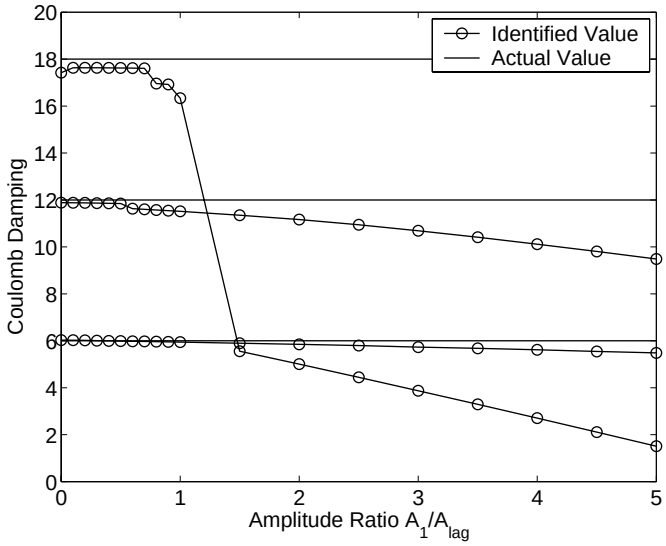

Figure 6.16: Effect of Amplitude Ratio on Coulomb Damping Estimation Using FSMB

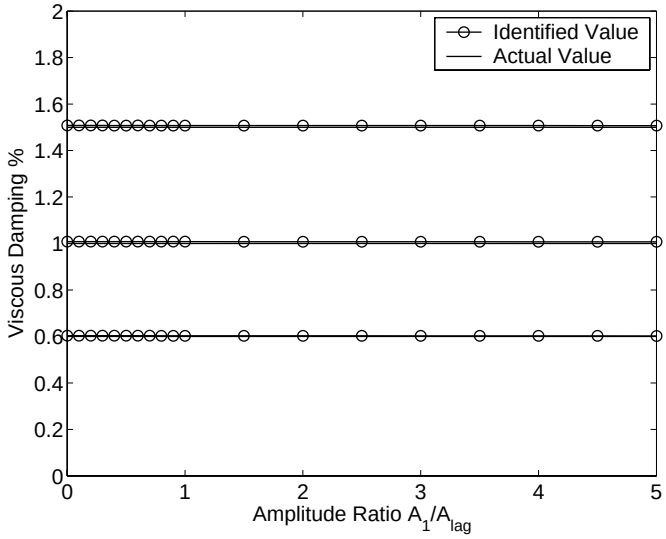

Figure 6.17: Effect of Amplitude Ratio on Viscous Damping Estimation Using Wavelet Transform

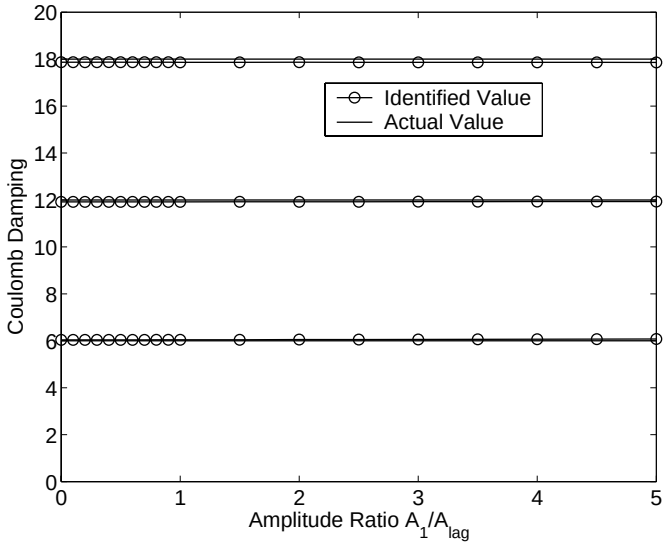

Figure 6.18: Effect of Amplitude Ratio on Coulomb Damping Estimation Using Wavelet Transform

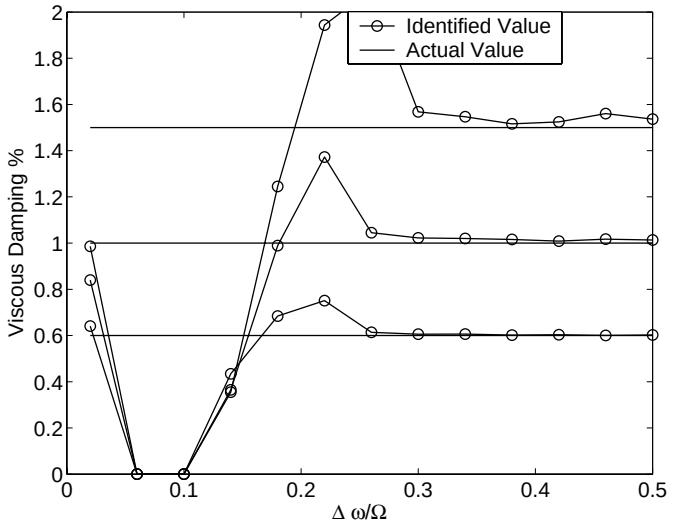

Figure 6.19: Effect of Frequency Separation on Viscous Damping Estimation Using FSMB

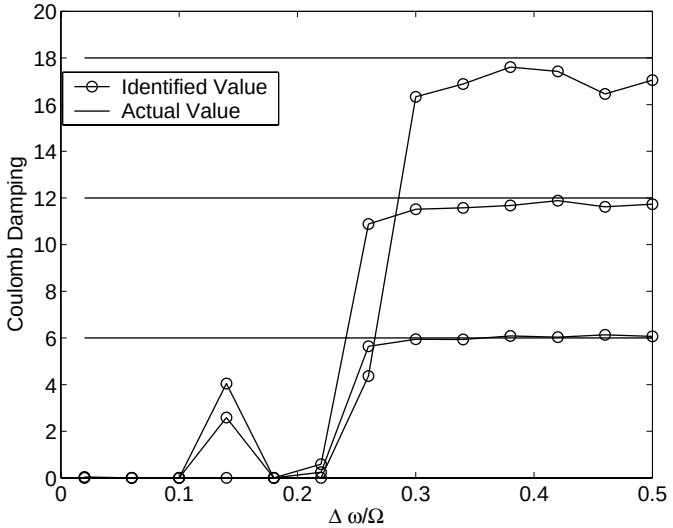

Figure 6.20: Effect of Frequency Separation on Coulomb Damping Estimation Using FSMB

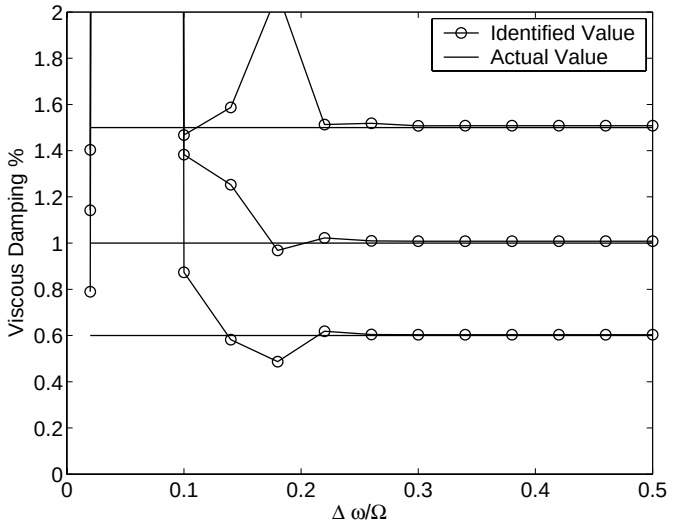

Figure 6.21: Effect of Frequency Separation on Viscous Damping Estimation Using Wavelet Transform

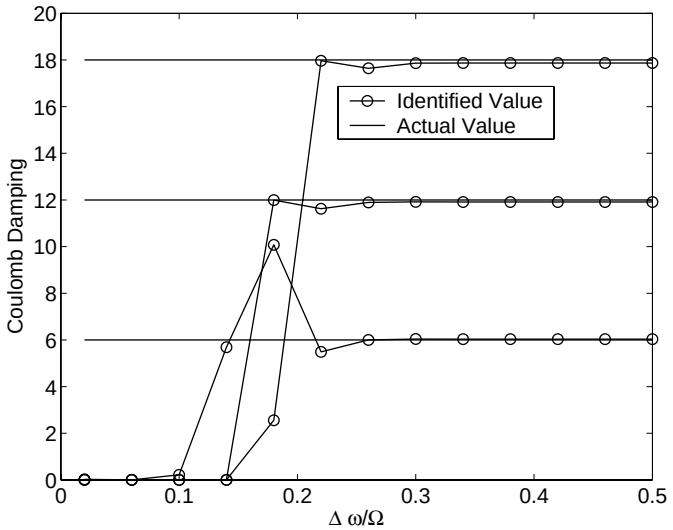

Figure 6.22: Effect of Frequency Separation on Coulomb Damping Estimation Using Wavelet Transform

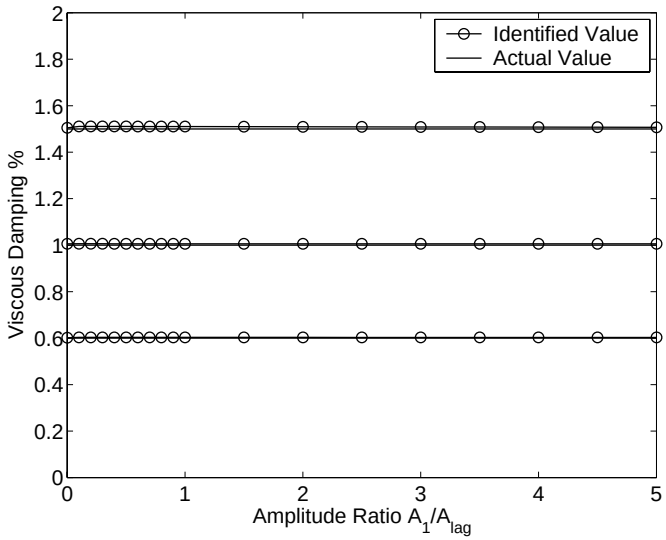

Figure 6.23: Effect of Amplitude Ratio on Viscous Damping Estimation Using Hybrid Method (Without Noise)

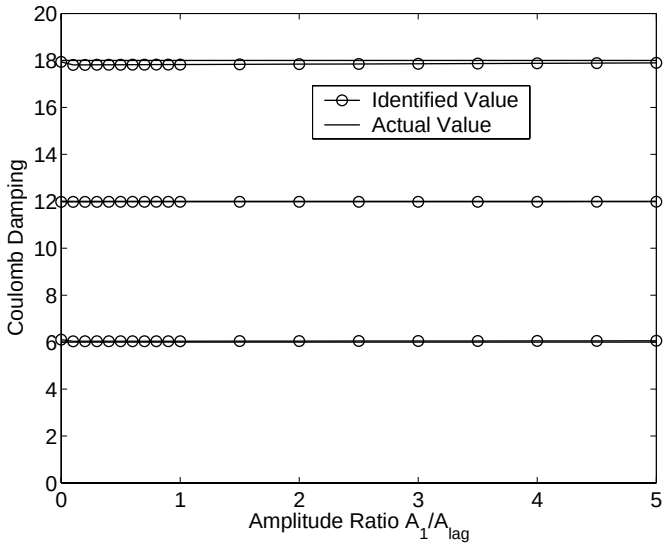

Figure 6.24: Effect of Amplitude Ratio on Coulomb Damping Estimation Using Hybrid Method (Without Noise)

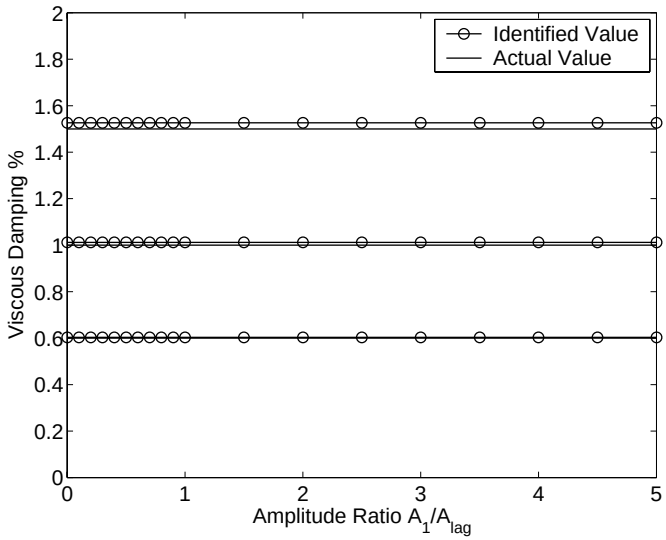

Figure 6.25: Effect of Amplitude Ratio on Viscous Damping Estimation Using Hybrid Method (With 5% Noise)

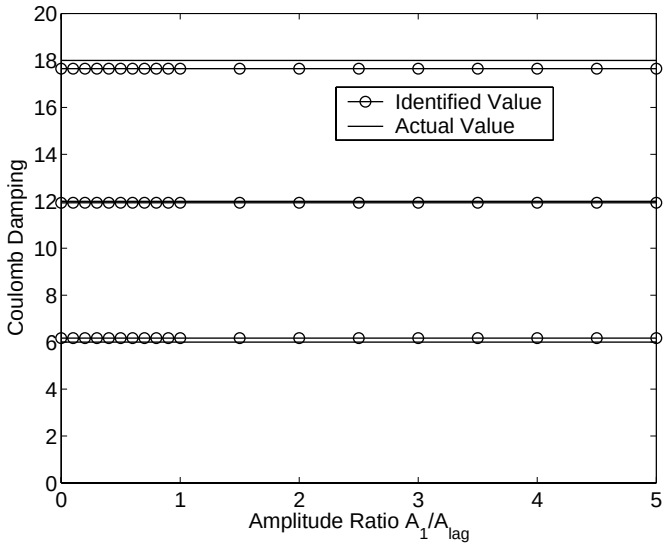

Figure 6.26: Effect of Amplitude Ratio on Coulomb Damping Estimation Using Hybrid Method (With 5% Noise)

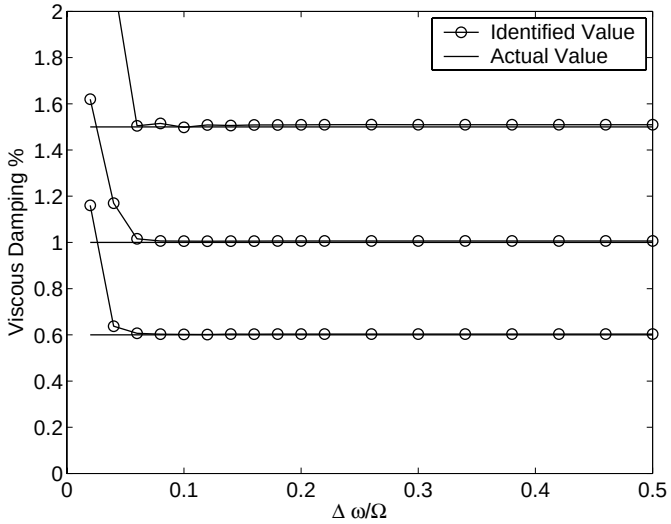

Figure 6.27: Effect of Frequency Separation on Viscous Damping Estimation Using Hybrid Method (Without Noise)

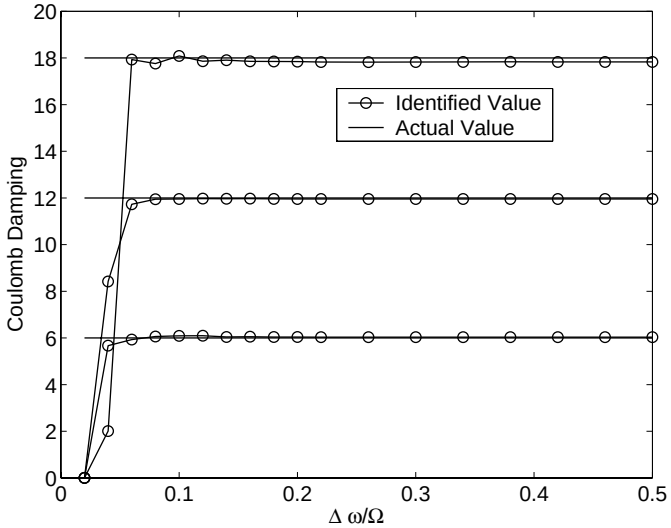

Figure 6.28: Effect of Frequency Separation on Coulomb Damping Estimation Using Hybrid Method (Without Noise)

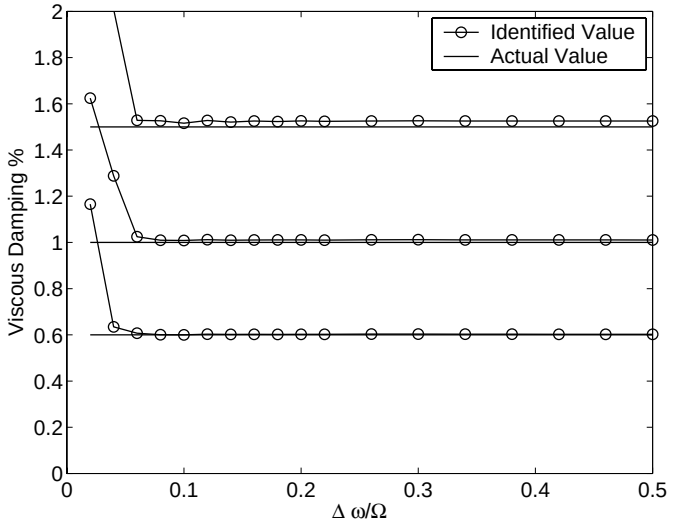

Figure 6.29: Effect of Frequency Separation on Viscous Damping Estimation Using Hybrid Method (With 5% Noise)

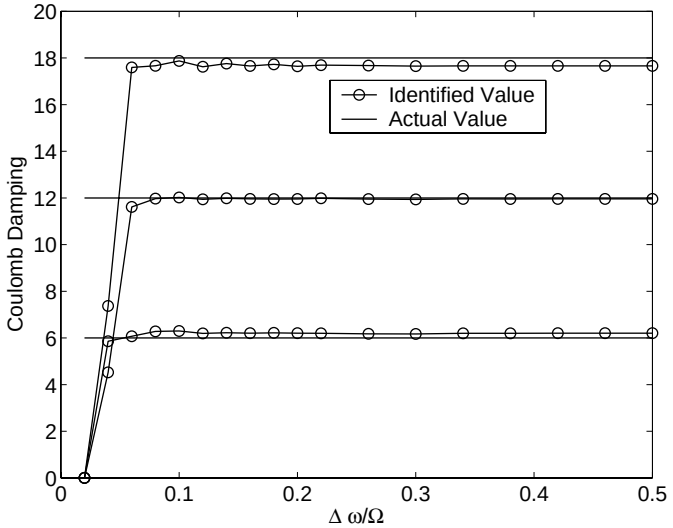

Figure 6.30: Effect of Amplitude Ratio on Coulomb Damping Estimation Using Hybrid Method (With 5% Noise)

Chapter 7

Conclusion and Future Works

7.1 Semi-Active Damping of Ground Resonance in Helicopters Using Magnetorheological Dampers

The feasibility of applying magnetorheological (MR) lag dampers to the mitigation of ground resonance instabilities was assessed. The influences of MR dampers on the aeromechnical instability of helicopter rotor systems were studied. The control schemes, open loop On-Off control and close loop feedback linearization control and sliding mode control, to integrate the MR dampers into ground resonance rotor model, were developed. The biviscous MR damper model was motivated by the extensive and ongoing program of design, and testing of MR dampers at University of Maryland. The following conclusions were made in this study:

1 It is feasible to stabilize an unstable rotor using MR dampers. In our initial feasibility study we showed that for a damper attachment point separation of 1.5 ft, the yield force of the MR damper is, $F_y = 3158lb$, indicating that the size and force level of MR dampers are in a proper and feasible range

to stabilize the ground resonance of the rotor system.

2 The stability of the rotor system is influenced only by the nondimensional yield force $\bar{F}_y$. The ratio of $\bar{C}_{po}/\bar{C}_{pr}$ has little effect on the stability. Therefore, the yield force controlled by applied magnetic field is the key control variable in MR dampers to mitigate ground resonance instability.

3 Advanced nonlinear control strategies, feedback linearization control and sliding mode control, were developed. The study showed that using MR dampers and a semi-active controller can stabilize an unstable rotor. The feedback linearization control strategy can be used maintain the design stability margin in the system, and the optimal damping levels was achieved. The sliding mode control, even though a stability diagram could not be computed, provides comparable results in the time domain to feedback linearization control.

7.2 Robustness to Damper Degradation

The control strategies are evaluated in the case damper when damage occurs. The anisotropic rotor model is developed due to the dissimilar dampers on each blade. The feedback linearization control is used to recover the unstability caused by damper degradation. The robustness study showed that the MR dampers actuated with a properly designed controller can recover stability when the rotor system loses stability due to damper degradation in most cases. The method failed only in the situation when 100% damping is lost on one blade. From the stand point of robustness to damper degradation, having two MR dampers per blade is better than having one damper per blade, because two MR dampers

per blade afford the opportunity to nearly recover the stability margins of the undamaged system when a single damper is lost.

7.3 Robustness to Parameter Perturbation

Both the feedback linearization control and sliding mode control can tolerate certain amount of parameter perturbations. However, the sliding mode control showed more robustness to parameter perturbation than feedback linearization control. For the perturbations of S_ζ, ν_ζ, ω_x, and ω_y, the sliding mode control showed that under at lease 20% perturbations, the control strategy can stabilize the rotor system. But for feedback linearization control, slight perturbation of these parameters (for exampe, 10% of ω_y) will make system unstable. By studying the time responses of sliding mode control and feedback linearization control, the way to improve the robustness of feedback linearization is suggested. The preset stability margin must be choosen enough large so that the control input can be enough to deal with the large parameter perturbations.

7.4 Linear Damping Identification in Helicopter Rotor Systems

Three damping identification algorithms are evaluated: Hilbert transform, Fourier Series Based Moving Block with Hamming window, and wavelet transform. The following conclusions are reached:

1. When the amplitude ratio is near zero, that is, for isolated mode case, all the three algorithms work well

2. When the amplitude ratio is high, Hilbert transform totally fails. If the lag/rev and 1/rev are well seperated, i.e. $\Delta\omega > 0.5Hz$, both FSMB and wavelet tranform can accurately identify the low damping level. If the damping is high, wavelet tranform achieves better results than FSMB method.

3. If the lag/rev and 1/rev are spectrally very close, both the FSMB and wavelet transform fail

Based on the evaluation, two hybrid algorithms for idenfying the lag/rev damping in helicopter rotor stability test data are developed that play to the strengths to the above three algorithms. We prefer the hybrid FSMB/wavelet algorithm because that using the wavelet transform, the extra filter is not necessary for spurious modes which spectrally far from lag mode. According to our results, we conclude that the hybrid FSMB/wavelet approach can

1. Identify high lag damping levels

2. Identify the damping level of the lag mode in the presence of a persistent 1/rev excitation, where the amplitude of the 1/rev excitation is comparable to the initial amplitude of the lag mode transient

3. Identify damping levels in signals with high noise levels (up to 10%). And it can get good results when the two modes are very close.

4. The method performed well when applied to actual experimental forward flight test data.

Hence, this method is shown to be a robust algorithm for identifying damping levels helicopter rotor stability test data.

7.5 Nonlinear Damping Identification in Systems Using ER/MR Dampers

The most widely used model for ER/MR dampers is Bingham-Plastic model. Using this model, when the ER/MR damper is on Off condition, the damper can be viewed as linear viscous damper, and when the ER/MR damper is On, the damper shows the combined viscous Coulomb damping characteristics. The method to identify the combined vicous Coulomb damping is developed.

1. The viscous damping and Coulomb damping of a MR damper can be identified simultaneously from the free response of the mass-damper-spring system with MR damper.

2. The damping identification is transfered to envelop identification so that the techniques researched in linear damping identification can applied.

3. For single degree of freedom system without noise, all the three methods studied, Hilbert transform, FSMB, and wavelet transform, work well .

4. For single degree of freedom system with noise, wavelet transform provides the best results.

5. For the system with persistent excitation such like rotor stability test data, hybrid FSMB/Wavelet method showed good performance. It is robust to amplitude ratio, robust to frequency separation, and robust to noise.

7.6 Recommendation for Future Work

1. To apply feedback control of MR dampers, more complex damper model needed. The hysteresis characteristics of MR damper should be included in the model. The effect of centrifugal force on MR dampers should be evaluated and modeled.

2. Since in flight condition, there are two excitation on MR dampers: the 1/rev and lag/rev, the effect of dual frequency excitation on MR dampers need to be evaluated.

3. To apply MR dampers on advanced soft in-plane rotors such as bearing less or hinge less rotors, the more complex ground resonance model need to be applied. The elastic blade as well as aerodynamics may be included. And effect of in-flow may also need to be modeled.

4. We claimed that by controling MR damper, the damper force on hub in forward flight condition could be reduced. This point need to be justified by calculating forward flight hub loads.

5. Other merits of MR dampers, such as insensitive to temperature, should also be explored.

Appendix A

The Source of Periodic Terms

Suppose the four rotor blades are identical, and the MR dampers and their yield forces on each blade are identical. Then the MR damper forces on each blade can be written as

$$\bar{F}_{(i)}(\overset{\star}{\zeta}_{(i)}) = \begin{cases} \bar{F}_y + \bar{C}_{po}\,\overset{\star}{\zeta}_{(i)} & \overset{\star}{\zeta}_{(i)} \geq \overset{\star}{\zeta}_y \\ \bar{C}_{pr}\,\overset{\star}{\zeta}_{(i)} & -\overset{\star}{\zeta}_y \leq \overset{\star}{\zeta}_{(i)} \leq \overset{\star}{\zeta}_y \\ -\bar{F}_y + \bar{C}_{po}\,\overset{\star}{\zeta}_{(i)} & \overset{\star}{\zeta}_{(i)} \leq -\overset{\star}{\zeta}_y \end{cases} \quad \text{for i} = 1,\ 2,\ 3,\ 4 \tag{7.1}$$

where i is blade number. The yield velocity, $\overset{\star}{\zeta}_y$, and the nondimensional preyield damping, $\bar{C}_{pr}$, are defined as:

$$\overset{\star}{\zeta}_y = \frac{\bar{F}_y}{\bar{C}_{pr} - \bar{C}_{po}} \tag{7.2}$$

$$\bar{C}_{pr} = \frac{C_{pr}}{I_b \Omega} \tag{7.3}$$

To transform the damper forces from rotating frame to fixed frame, Fourier Coordinate Transform (FCT) is used which result in $\{\bar{F}\}_{fixed} = [D(\psi)]\{\bar{F}\}$

where $[D(\psi)]$, is,

$$[D(\psi)] = \begin{bmatrix} \frac{1}{4} & \frac{1}{4} & \frac{1}{4} & \frac{1}{4} \\ -\frac{1}{4} & \frac{1}{4} & -\frac{1}{4} & \frac{1}{4} \\ \frac{1}{2}cos(\psi_{(1)}) & \frac{1}{2}cos(\psi_{(2)}) & \frac{1}{2}cos(\psi_{(3)}) & \frac{1}{2}sin(\psi_{(4)}) \\ \frac{1}{2}sin(\psi_{(1)}) & \frac{1}{2}sin(\psi_{(2)}) & \frac{1}{2}sin(\psi_{(3)}) & \frac{1}{2}sin(\psi_{(4)}) \\ 0 & 0 & 0 & 0 \\ 0 & 0 & 0 & 0 \end{bmatrix}$$

$$= \begin{bmatrix} \frac{1}{4} & \frac{1}{4} & \frac{1}{4} & \frac{1}{4} \\ -\frac{1}{4} & \frac{1}{4} & -\frac{1}{4} & \frac{1}{4} \\ \frac{1}{2}cos(\psi) & -\frac{1}{2}sin(\psi) & -\frac{1}{2}cos(\psi) & \frac{1}{2}sin(\psi) \\ \frac{1}{2}sin(\psi) & \frac{1}{2}cos(\psi) & -\frac{1}{2}sin(\psi) & -\frac{1}{2}cos(\psi) \\ 0 & 0 & 0 & 0 \\ 0 & 0 & 0 & 0 \end{bmatrix} \tag{7.4}$$

Where

$$\psi = \psi_{(1)} \tag{7.5}$$

The force vector are given as

$$\{\bar{F}\}^t = \left\{ \bar{F}_{(1)}(\overset{\star}{\zeta}_{(1)}), \bar{F}_{(2)}(\overset{\star}{\zeta}_{(2)}), \bar{F}_{(3)}(\overset{\star}{\zeta}_{(3)}), \bar{F}_{(4)}(\overset{\star}{\zeta}_{(4)}) \right\} \tag{7.6}$$

$\bar{F}_{(i)}(\overset{\star}{\zeta}_{(i)})$ for i=1,2,3,4, is the nondimensional damping force on each blade.

What we want to prove is that the periodic terms in $[D]\{\bar{F}\}$ can not be canceled due to the nonlinearity of $\bar{F}_{(i)}$.

Let's exam the cyclic lead lag angle rate $\overset{\star}{\zeta}_{1c}$ and $\overset{\star}{\zeta}_{1s}$

$$\overset{\star}{\zeta}_{(i)} = \left(\overset{\star}{\zeta}_{1c} + \zeta_{1s}\right) cos\psi_{(i)} + \left(\overset{\star}{\zeta}_{1s} - \zeta_{1c}\right) sin\psi_{(i)} \tag{7.7}$$

for i=1,2,3,4

let

$$\psi_{(1)} = \psi \tag{7.8}$$

then

$$\begin{aligned}
\psi_{(2)} &= \psi + \frac{\pi}{2} \\
\psi_{(3)} &= \psi + \pi \\
\psi_{(4)} &= \psi + \frac{3\pi}{2}
\end{aligned} \tag{7.9}$$

Then we have

$$\begin{aligned}
\overset{\star}{\zeta}_{(1)} &= \left(\overset{\star}{\zeta}_{1c} + \zeta_{1s}\right) cos\psi + \left(\overset{\star}{\zeta}_{1s} - \zeta_{1c}\right) sin\psi \\
\overset{\star}{\zeta}_{(2)} &= \left(\overset{\star}{\zeta}_{1c} + \zeta_{1s}\right) cos(\psi + \pi/2) + \left(\overset{\star}{\zeta}_{1s} - \zeta_{1c}\right) sin(\psi + \pi/2) \\
\overset{\star}{\zeta}_{(3)} &= \left(\overset{\star}{\zeta}_{1c} + \zeta_{1s}\right) cos(\psi + \pi) + \left(\overset{\star}{\zeta}_{1s} - \zeta_{1c}\right) sin(\psi + \pi) \\
\overset{\star}{\zeta}_{(4)} &= \left(\overset{\star}{\zeta}_{1c} + \zeta_{1s}\right) cos(\psi + 3\pi/2) + \left(\overset{\star}{\zeta}_{1s} - \zeta_{1c}\right) sin(\psi + 3\pi/2)
\end{aligned} \tag{7.10}$$

Which lead to

$$\begin{aligned}
\overset{\star}{\zeta}_{(3)} &= - \overset{\star}{\zeta}_{(1)} \\
\overset{\star}{\zeta}_{(4)} &= - \overset{\star}{\zeta}_{(2)}
\end{aligned} \tag{7.11}$$

If we have

$$\begin{aligned}
\overset{\star}{\zeta}_{(1)} &\geq \overset{\star}{\zeta}_{y} \\
\overset{\star}{\zeta}_{(2)} &\geq \overset{\star}{\zeta}_{y}
\end{aligned} \tag{7.12}$$

then

$$\begin{aligned} \overset{\star}{\zeta}_{(3)} &\leq -\overset{\star}{\zeta}_{y} \\ \overset{\star}{\zeta}_{(4)} &\leq -\overset{\star}{\zeta}_{y} \end{aligned} \tag{7.13}$$

According to Eqn.(7.1), we have

$$\begin{aligned} \bar{F}_{(1)} &= \bar{F}_y + \bar{C}_{po}\,\overset{\star}{\zeta}_{(1)} \\ \bar{F}_{(2)} &= \bar{F}_y + \bar{C}_{po}\,\overset{\star}{\zeta}_{(2)} \\ \bar{F}_{(3)} &= -\bar{F}_y + \bar{C}_{po}\,\overset{\star}{\zeta}_{(3)} \\ \bar{F}_{(4)} &= -\bar{F}_y + \bar{C}_{po}\,\overset{\star}{\zeta}_{(4)} \end{aligned} \tag{7.14}$$

Remember that the Fourier Coordinate Transform (FCT) for four blade rotor provides

$$\begin{aligned} \frac{1}{4}\sum_{i=1}^{4}\overset{\star}{\zeta}_{(i)} &= \overset{\star}{\zeta}_{0} \\ \frac{1}{4}\sum_{i=1}^{4}\overset{\star}{\zeta}_{(i)}\,(-1)^{i} &= \overset{\star}{\zeta}_{2} \\ \frac{2}{4}\sum_{i=1}^{4}\overset{\star}{\zeta}_{(i)}\,cos\psi_{(i)} &= \overset{\star}{\zeta}_{1c} + \zeta_{1s} \\ \frac{2}{4}\sum_{i=1}^{4}\overset{\star}{\zeta}_{(i)}\,sin\psi_{(i)} &= \overset{\star}{\zeta}_{1s} - \zeta_{1c} \end{aligned} \tag{7.15}$$

Then

$$
\begin{aligned}
[D(\psi)]\{\bar{F}\} &= \begin{bmatrix} \frac{1}{4} & \frac{1}{4} & \frac{1}{4} & \frac{1}{4} \\ -\frac{1}{4} & \frac{1}{4} & -\frac{1}{4} & \frac{1}{4} \\ \frac{1}{2}cos(\psi) & -\frac{1}{2}sin(\psi) & -\frac{1}{2}cos(\psi) & \frac{1}{2}sin(\psi) \\ \frac{1}{2}sin(\psi) & \frac{1}{2}cos(\psi) & -\frac{1}{2}sin(\psi) & -\frac{1}{2}cos(\psi) \\ 0 & 0 & 0 & 0 \\ 0 & 0 & 0 & 0 \end{bmatrix} \begin{bmatrix} \bar{F}_y + \bar{C}_{po}\,\overset{\star}{\zeta}_{(1)} \\ \bar{F}_y + \bar{C}_{po}\,\overset{\star}{\zeta}_{(2)} \\ -\bar{F}_y + \bar{C}_{po}\,\overset{\star}{\zeta}_{(3)} \\ -\bar{F}_y + \bar{C}_{po}\,\overset{\star}{\zeta}_{(4)} \end{bmatrix} \\
&= \begin{bmatrix} \bar{C}_{po}\,\overset{\star}{\zeta}_0 \\ \bar{C}_{po}\,\overset{\star}{\zeta}_2 \\ (cos(\psi) - sin(\psi))\bar{F}_y + \bar{C}_{po}(\overset{\star}{\zeta}_{1c} + \zeta_{1s}) \\ (cos(\psi) + sin(\psi))\bar{F}_y + \bar{C}_{po}(\overset{\star}{\zeta}_{1s} - \zeta_{1c}) \\ 0 \\ 0 \end{bmatrix} \qquad (7.16)
\end{aligned}
$$

Periodic terms cannot be canceled because of the nonlinearity of the damper force, even if the four blades are identical.

Appendix B

Controllability and Stability of the Rotor System With 100% Damping Lost On One Blade

Controllability Criteria for Periodic System

For the periodic system

$$\begin{aligned} \dot{x} &= A(t)x + B(t)u \\ y &= H(t)x \end{aligned} \tag{7.17}$$

with period T

It can be transfered to

$$\begin{aligned} \dot{w} &= Jw + F^{-1}(t)B(t)u \\ y &= H(t)F(t)w \end{aligned} \tag{7.18}$$

using Floquet theory, where $w = F^{-1}(t)x(t)$.

Then the system (7.17) is controllable iff

$$\begin{aligned} \eta F^{-1}(t)B(t) = 0 \\ \forall t \in [0, T] \\ \text{implies } \eta = 0 \end{aligned} \tag{7.19}$$

where η is left eigenvector of J, $\eta J = \kappa\eta$

Application to Ground Resonance Problem

For the ground resonance model

$$[M]\left\{\overset{\star\star}{q}\right\} + [C]\left\{\overset{\star}{q}\right\} + [K]\{q\} + [D(\psi)]\{\bar{u}\} = 0 \tag{7.20}$$

with one blade lose 100% damping

$$[D(\psi)] = \begin{bmatrix} \frac{1}{4} & \frac{1}{4} & \frac{1}{4} \\ -\frac{1}{4} & \frac{1}{4} & -\frac{1}{4} \\ \frac{1}{2}cos(\psi) & -\frac{1}{2}sin(\psi) & -\frac{1}{2}cos(\psi) \\ \frac{1}{2}sin(\psi) & \frac{1}{2}cos(\psi) & -\frac{1}{2}sin(\psi) \\ 0 & 0 & 0 \\ 0 & 0 & 0 \end{bmatrix}$$

is time periodic. The state vector and control vector are given as

$$\{\bar{u}\}^t = \left\{ \bar{F}_1(\overset{\star}{\zeta}_{(1)}), \bar{F}_2(\overset{\star}{\zeta}_{(2)}), \bar{F}_3(\overset{\star}{\zeta}_{(3)}) \right\}$$

$\bar{F}_i(\overset{\star}{\zeta}_{(i)})$ for i=1,2,3 is the nondimensional damping force on each blade.

Rewrite above system using state equation

$$\dot{x} = Ax + B(t)u \tag{7.21}$$

where

$$A = \begin{bmatrix} 0 & I \\ -[M]^{-1}[k] & -[M]^{-1}[C] \end{bmatrix} \tag{7.22}$$

$$B = \begin{bmatrix} 0 \\ -[M]^{-1}[D(\psi)] \end{bmatrix} \tag{7.23}$$

Then we can directly apply the controllability criteria (7.19) to above system. Notice that since the A matrice is constant, $F(t) = I$.

However, this criteria is for the active control system, which does not consider the constraint of semi active condition. The result is unfortunately the system is controllable.

Stability of Rotor System with 100% Damping Lost on One Blade

In this section we apply the feedback linearization control law first, then analyze the stability of the close loop system.

$$[M]\left\{\overset{\star\star}{q}\right\} + [C(\psi)]\left\{\overset{\star}{q}\right\} + [K(\psi)]\{q\} = 0 \tag{7.24}$$

Rewrite is as state equation

$$\dot{x} = A_1(\bar{c}, \psi)x \tag{7.25}$$

To analyze the stability of this system, the floquet theory must be applied. Numerical solution is needed.

We know that

$$\bar{c}_{po} \leq \bar{c} \leq \bar{c}_{pr} \tag{7.26}$$

If for largest $\bar{c} = \bar{c}_{pr}$, the system is unstable, the system can not be stabilized using MR dampers. Results are shown in Fig. (3.6).

BIBLIOGRAPHY

[1] Kamath, G.M., Wereley, N.M., and Jolly, M.R. "Characterization of Magnetorheological Helicopter Lag Dampers," *Journal of the American Helicopter Society.* Vol. 44, Number 3, July, 1999, pp. 234-248.

[2] Winslow W.M., "Method and Means for Translating Electrical Impulses Into Mechanical Force," US Patents 2,417,850, 1947.

[3] Winslow W.M., "Induced Fibration of Suspension," *Journal of Applied Physics*, Vol. 20, 1949, pp. 1137-1140.

[4] Carlson, J.D., and Weiss, K.D., "A Growing Attraction to Magnetic Fluids," *Machine Design*, August 8, 1994, pp. 61-64.

[5] Halsey, T.C, and Martin, J.E., "Electrorheological Fluids," *Scientific American*, Oct. 1993, pp. 58-64.

[6] Klingenberg, D.J., "Making Fluids into Solids with Magnets," *Scientific American*, Oct. 1993, pp. 112-113.

[7] Block, H., and Kelly, J.P., "Electro-rheology," *Journal of Physics D: Applied Physics*, Vol 21, 1998, pp. 1661-1667.

[8] Felt, D.W., Hagenbuchle, M., Liu, M., and Richard, J.,"Rheology of a Magnetorheological Fluid," *Journal of Intelligent Material System and Structures*, Vol. 7, No. 5, 1996, pp. 589-593.

[9] Kraynik, A.M., "Comments on ER Fluid Rheology," *Proceedings of the Second International Conference on ER Fluids*, Raleigh, NC, August 7-9, 1989, pp. 445-454.

[10] Coulter, J.P., and Duclos, T.G., "Applications of Electrorheological Materials in Vibration Control," *Proceedings of the Second International Conference on ER Fluids*, Raleigh, NC, August 7-9, 1989, pp. 384-391.

[11] Gamota, D.R., and Filisko, F.E., "Dynamic Mechanical Studies of Electrorheological Materials: Moderate Frequencies," *Journal of Rheology*, Vol. 35, No. 3, 1991, pp. 399-425.

[12] Gamota, D.R., and Filisko, F.E., "High Frequency Dynamic Mechanical Study of an Aluminosilicate Electrorheological Material," *Journal of Rheology*, Vol. 35, No. 7, 1991, pp. 1411-1426.

[13] Gamota, D.R., and Filisko, F.E., "Fourier Transform Analysis: Nonlinear Dynamic Response of an Electrorheological Material," *Journal of Rheology*, Vol. 37, No. 5, 1993, pp. 919-933.

[14] Kamath, G.M., and Wereley, N.M., "Nonlinear Viscoelastic Plastic Mechanisms Based Model of an Electrorheological Dampers," *Journal of Guidance, Control, and Dynamics*, Vol. 20, No. 6, 1997, pp. 1125-1132.

[15] Wang, X., and Gordaninejad, F., "Dynamic Modeling of Semi-Active ER/MR Fluid Dampers," *Proceedings of SPIE Symposium on Smart Structures and Materials*, Vol. 4331, 2001, pp. 82-91.

[16] Brooks, D.A., "Design and Development of Flow Based ER Devices," *International Journal of Modern Physics B*, Vol. 6, 1992, pp. 2705-2730.

[17] Carlson, J.D., Catanzarite, D.M., and St. Clair, K.A., "Commercial Magnetorheological Fluid Devices," *International Journal of Modern Physics B*, Vol. 10, No. 23-24, 1996, pp. 2857-2865.

[18] Gavin, H.P., *Electrorheological Damper for Structural Vibration Suppression*, Ph.D Dissertation, University of Michigan, 1994.

[19] Gordaninejad, F., Ray, A., and Bindu, R., "Control of Forced Vibration Using Multi Electrode Electro-rheological Fluid Dampers," *ASME Journal of Vibration and Acoustics*, Vol.119, No.4, Oct. 1997, pp. 527-531.

[20] Wereley, N.M., Pang, L., and Kamath G.M., "Idealized Hysteresis Modeling of ER and MR Dampers," *Journal of Intelligent Material Systems and Structures*, Vol. 9, No. 8, 1998, pp. 642-649.

[21] Lindler, J.E., and Wereley, N.M., "Double Adjustable Shock Absorbers Using ER Fluid," *Journal of Intelligent Material Systems And Structures*, Vol. 10, No. 8, August, 2000, pp. 652-657.

[22] Jeon, D., Park, C., and Park, K., "Vibration Suppression by Controlling an MR Damper," *International Journal of Modern Physics B*, Vol. 13, Nos 14, 15, & 16, 1999, pp. 2221-2228.

[23] Lam, H.F., and Liao W.H., "Semi-Active Control of Automotive Suspension Systems with Magnetorheological Dampers," *Proceedings of SPIE Symposium on Smart Structures and Materials*, Vol. 4327, 2001, pp. 125-136

[24] Miller, L.R., and Nobles, C.M. "The Design and Development of a Semi-active Suspension of a Military Tank," *SAE Technical Paper Series*, No. 881133, 1988.

[25] Kelso, S., and Shawn, P., "Experimental Characterization of Commercially Practical Magnetorheological Fluid Damper Technology," *Proceedings of SPIE Symposium on Smart Structures and Materials*, Vol 4332, 2001, pp. 292-299.

[26] Carlson, J.D., Matthis, W., and Toscano J.R., "Smart Prosthetics Based on Magnetorheological Fluids," *Proceedings of SPIE Symposium on Smart Structures and Materials*, Vol 4332, 2001, pp. 308-316.

[27] Jolly, M., "Pneumatic Motion Control Using Magnetorheological Technology," *Proceedings of SPIE Symposium on Smart Structures and Materials*, Vol 4332, 2001, pp. 300-307.

[28] Zhou C., Robb, D.A., and Ewins, D.J. "Effectiveness of a Disk-Type MR Fluid Damper for Rotor System Vibration Control," *Proceedings of SPIE Symposium on Smart Structures and Materials*, Vol 4331, 2001, pp. 379-385.

[29] Coleman R.P., and Feingold, A.M., "Theory of Self-Excited Mechanical Oscillations of Helicopter Rotors with Hinged Blades,"NACA TR-1351, 1956.

[30] Hooper, W.E., "Effect of Fuselage Dynamics on Helicopter Ground Resonance," *Aircraft Engineering*, Vol. 34, August, 1962, pp. 226-230.

[31] Gabel, R., "Exact Mechanical Instability Boundaries as Determined from the Coleman Equation," *Journal of the American Helicopter Society*, Vol. 7, No.1, January, 1962, pp. 17-21.

[32] Johnson, W., "Recent Developments in the Dynamics of Advanced Rotor Systems," NASA TM-96669, March 1985.

[33] Ormiston, R.A., "Investigations of Hingeless Rotor Stability," *Vertica*, Vol. 7, No.2, 1983, pp. 143-181.

[34] Freidmann, P.P., "Fundamental and Solution for Rotary Wing Aeroelatic Stability and Response Problems," *Vertica*, Vol. 17, No. 2, 1983, pp. 101-141.

[35] Lytwin, R.T., and Miao, W., "Airborne and Ground Resonance of Hingeless Rotors," *Journal of the American Helicopter Society*, Vol. 16, No. 2, April, 1971, pp. 2-9.

[36] Donham, R.E., Cardinale S.V., and Sachs I.B., "Ground and Air Resonance Characteristics of a Soft In-Plane Rigid-Rotor System," *Journal of the American Helicopter Society*, Vol. 14, No. 14, Oct., 1969, pp. 33-41.

[37] Straub, F.K., "Study to Eliminate Ground Resonance Using Active Controls," NASA CR-166609, Oct., 1985.

[38] Bousman, W.G., "An Experimental Investigation of the Effect of Aeroelastic Couplings on Aeromechnical Stability of a Hingeless Rotor Helicopter," *Journal of the American Helicopter Society*, Vol. 26, No. 1, Jan., 1981, pp. 46-54.

[39] Johnson, W., "Influence of Unsteady Aerodynamics on Hingeless Rotor Ground Resonance," *AIAA Journal of Aircraft*, Vol. 19, No. 8, Aug. 1982, pp. 668-673.

[40] Friedmann, P.P., and Venkatesan, C., "Influence of Unsteady Aerodynamic Models on the Aeromechanical Stability in Ground Resonance," *Journal of the American Helicopter Society*, Vol. 31, No. 1, Jan. 1986, pp. 65-74.

[41] Jang, J., and Chopra, I., "Ground and Air Resonance of an Advanced Bearingless Rotor in Hover," *Journal of the American Helicopter Society*, Vol. 33, No. 3, July 1988, pp. 20-29.

[42] Jang, J., and Chopra, I., "Air Resonance of an Advanced Bearingless Rotor in Forward Flight," *Proceedings of the 2nd International Conference on Rotorcraft Basic Research*, College Park, MD, Feb., 1988.

[43] Kunz, D. L., "Nonlinear Analysis of Helicopter Ground Resonance," *AIAA/ASME/ASCE/AHS/ASC Structures, Structural Dynamics and Materials Conference*, Vol. 1, No. 3, 2000, pp. 1897-1904.

[44] Jang, J., *Ground and Air Resonance of Bearingless Rotors in Hover and Hover Flight*, Ph.D. Thesis, Department of Aerospace Engineering, University of Maryland, 1988.

[45] McGuire, D.P., "The Application of Elastomeric Lead Lag Dampers to Helicopter Rotors," Lord Library, No. LL2133.

[46] Gandhi, F., and Chopra, I., "Analytical Model for A Nonlinear Elastomeric Lag Damper and Its Effect on Aeromechanical Stability in Hover," *Journal of the American Helicopter Society*, Vol. 39, No. 4, Oct, 1994, pp. 59-69.

[47] Hausman, G., and Gergley P., "Approximate Methods for Thermoviscoelastic Characterization and Analysis of Elatomeric Lead Lag Dampers," *Proceedings of the 18th European Rotorcraft Forum*, Sept., 1992.

[48] Nath, S., and Wereley, N.M., "Active Constrained Layer Damping for Rotorcraft Flex Beams," *Proceedings of the 36th AIAA/ASME/ASCE/AHS/ASC Structures, Structural Dynamics, and Materials Conference and AIAA/ASME Adaptive Structures Forum*, Part 5 (of 5), Apr 10-13 1995, New Orleans, LA, USA, pp. 2867-2875.

[49] Smith, E.C., and Chopra, I., "Air and Ground Resonance of Helicopters with Elastically Tailored Composite Rotor Blades," *Journal of the American Helicopter Society*, Vol. 38, No. 4, Oct, 1993, pp. 50-61.

[50] Zotto, R.G., and Loewy, R.G., "Influence of Pitch-Lag Coupling on Damping Requirements to Stabilize 'Ground/Air Resonance'," *Journal of the American Helicopter Society*, Vol. 37, No. 4, Oct, 1992, pp. 68-71.

[51] Gandhi, F., and Hathaway, E., "Optimized Aeroelastic Couplings for Alleviation of Helicopter Ground Resonance," *Journal of Aircraft*, Vol. 35, No. 4, July-August, 1998, pp. 582-590.

[52] Liu, Q., and Chattopadhyay, A., "Improved Helicopter Aeromechanical Stability Analysis Using Segmented Constrained Layer Damping and Hybrid Optimization," *Journal of Intelligent Material Systems and Structures*, Vol. 11, No. 6, June 2000, pp. 492-500.

[53] Straub, F.K., "Use Of Active Controls To Augment Rotor/Fuselage Stability," *Journal of the American Helicopter Society*, Vol. 30, No. 3, July, 1985, pp. 13-22.

[54] Gandi, F., and Weller, W., "Active Aeromechanical Stability Augmentation Using Fuselage State Feedback," *Proceedings of the 53rd Annual Forum of American Helicopter Society*, Part 2 (of 3), Apr. 29-May 1, 1997, Virginia Beach, VA, pp. 1350-1362.

[55] Hathaway, E., and Gandhi, F., "Individual Blade Control for Alleviation of Helicopter Ground Resonance," *Proceedings of the 39th AIAA/ASME/ASCE/AHS/ASC Structures, Structural Dynamics, and Materials Conference and Exhibit and AIAA/ASME/AHS Adaptive Structures Forum*, Part 4 (of 4), Apr. 20-23, 1998, Long Beach, CA, USA, pp. 2507-2517.

[56] Marathe, S., Gandhi, F., Wang, K.W., "Helicopter Blade Response And Aeromechanical Stability With a Magnetorheological Fluid Based Lag Damper," *Journal of Intelligent Material Systems and Structures*, Vol. 9, No. 4, Apr, 1998, pp. 272-282.

[57] Prasanth, R.K., Mehra, R.K., Bennett, R.L., Brown, R., "Energy to Peak Control of LPV Systems with Application to Rotorcraft Ground Resonance," *Proceedings of the 2001 American Control Conference*, Piscataway, NJ, USA, Vol. 2, 2001, pp. 1339-1344.

[58] Agneni, A., and Crema B. L., "Analytic Signal in The Damping Coefficient Estimation," *Proceedings of International Conference: Spacecraft Structures*

and Mechanical Testing, Noordwijk, The Netherlands, 19-21 Oct. 1989, pp. 133-139.

[59] Feldman, M., "Non-Linear System Vibration Analysis Using Hilbert Transform - I. Free Vibration Analysis Method 'Freevib'," *Mechanical Systems and Signal Processing*, Vol. 8, No. 2, 1994, pp. 119-127.

[60] Feldman, M., "Non-Linear System Vibration Analysis Using Hilbert Transform - II. Forced Vibration Analysis Method 'Forcevib'," *Mechanical Systems and Signal Processing*, Vol. 8, No. 3, 1994, pp. 309-318.

[61] Feldman, M., and Braun, S., "Time-Frequency Characteristic of Non-Linear Systems," *Mechanical Systems and Signal Processing*, Vol. 11, No. 4, 1997, pp. 611-620.

[62] Feldman, M., and Braun, S., "Non-Stationary Vibration Analysis By Using The Hilbert Transform," *Vibration and Noise*, 1995, pp. 465-475.

[63] Feldman, M., "Non-Linear Free Vibration Identification Via The Hilbert Transform," *Journal of Sound and Vibration*, No. 3, Vol. 208, 1997, pp. 475-489.

[64] Kang, M.S., "Modal Testing Using a Scanning Laser Doppler Vibrometer - Hilbert transform Approach," *Proceedings of IMAC-XIX: A Conference on Structural Dynamics*, Vol. 2, Feb 5-8, 2001, pp. 1709-1715.

[65] Nagarajaiah, S., Varadarajan, N., "Smart Variable Stiffness Control Systems," *Proceedings of SPIE Conference on Smart Systems for Bridges, Structures, and Highways-Smart Structures and Materials*, Vol. 4330, Mar 5-7, 2001, pp. 345-353.

[66] Huang, N. E., "New Method for Nonlinear and Nonstationary Time Series Analysis: Empirical Mode Decomposition and Hilbert Spectral Analysis," *Proceedings of SPIE, Wavelet Applications VII*, Vol. 4056, Apr. 26-28, 2000, pp. 197-209.

[67] Gravier, B.M., Napal, N.J., Pelstring, J.A., Jordan, D.A., and Miksad, R., "An Assessment of The Application of The Hilbert Spectrum to The Fatigue Analysis of Marine Risers," *Proceedings of 11th International Offshore and Polar Engineering Conference*, Vol. 2, Jun 17-22, 2001, Stavanger, pp. 268-275.

[68] Qiang, G., Xiaojiang, M., Haiyong, Z., and Yankun, Z., "The Partial Wave Method for The Analysis of Non-stationary Signals and Its Use in Machine Fault Diagnosis," *Proceedings of the 4th International Symposium on Test and Measurement (ISTM/2001)*, Vol. 2, Jun 1-3, 2001, Shanghai, China, pp. 1465-1468.

[69] Yang, J.N., and Lei, Y., "Identification of Civil Structures with Nonproportional Damping," *Proceedings of SPIE, Conference On Smart Systems for Bridges, Structures, and Highways*, Mar 6-7 2000, Newport Beach, CA, USA, pp. 284-294.

[70] Salvino, L.W., "Empirical Mode Analysis of Structural Response and Damping," *Proceedings of SPIE, IMAC-XVIII: A Conference on Structural Dynamics 'Computational Challenges in Structural Dynamics'*, Vol. 4062, Feb. 7-10, 2000, San Antonio, TX, USA, pp. 503-509.

[71] Anderson, W. D., "Investigation of Reactionless Mode Stability Characteristics of a Stiff Inplane Hingeless Rotor System," *American Helicopter Society*, Preprint No. 734, May 1973.

[72] Hammond, C.E., and Doggett Jr., R.V., "Determination of Subcritical Damping by Moving-Block/Randomdec Applications," *NASA Symposium on Flutter Testing Techniques*, NASA CP-415, October, 1975, pp. 59-76.

[73] Bousman, W.G., and Winkler, D.J., "Application of the Moving-Block Analysis," *22nd AIAA Structures, Structural Dynamics, and materials Conference*, April 6-8, 1983, Atlanta, Ga. AIAA Paper No. 81-0653. Vol. CP812. pp. 755-763.

[74] Smith, C.B. and Wereley, N.M., "Active-Passive Constrained Layer Damping of Composite Rotating Flexbeams," *37th AIAA/ASME Adaptive Structures Forum*, Apr 18-19, Salt Lake City, Utah. Paper No. AIAA-96-1290, 1996, pp. 207-216.

[75] Smith, C.B. and Wereley, N.M., "Composite Rotorcraft Flexbeams with Viscoelastic Damping Layers for Aeromechanical Stability Augmentation," *M3D III: Mechanics and Mechanisms of Material Damping, ASTM STP 1304, A. Wolfenden and V.K. Kinra, Eds., American society for Testing and Materials*, 1997, pp. 62-77.

[76] Kamath, G.M., Wereley, N.M., and Jolly, M.R., "Characterization of Semi-Active Magnetorheological Helicopter Lag Mode Dampers," *SPIE's 5th International Symposium on Smart Structures and Materials*, Mar 1-5, 1998, San Diego, DA, pp. 3329-3337.

[77] Smith, C.B. and Wereley, N.M., "Transient Analysis for Damping Identification in Rotating composite Beams with Integral Damping layers," *Smart Materials and Structures*, Vol. 5, 1996, pp. 540-550.

[78] Tasker, F.A., *Damping Estimation in Helicopter Rotor Stability Testing*, Doctoral Dissertation, Department of Aerospace Engineering, University of Maryland, 1996.

[79] Tasker, F.A., and Chopra, I., "Assessment of Transient Analysis Techniques for Rotor Stability Testing," *Journal of the American Helicopter Society*, Jan, 1990, pp. 39-50.

[80] Torok, M.S., and Chopra, I., "Hingeless Rotor Aeroelastic Stability Analysis with Refined Aerodynamic Modeling," *Journal of the American Helicopter Society*, Vol. 36, No. 4, Oct, 1991, pp. 48-56.

[81] Amrani, A.O., and Du Val, R., "Parameter Identification of Aeroelastic Modes of Rotary Wings from Rransient Time Histories," *Journal of Guidance, Control, and Dynamics*, Vol. 13, No. 4, Jul-Aug, 1990, pp. 669-674.

[82] Ruzzene, M., Fasana, A. Garibaldi, L., and Piombo, B., "Natural Frequencies and Dampings Identification Using Wavelet Transform: Application to Real Data," Mechanical Systems and Signal Processing, Vol. 11, No. 2, March, 1997, pp. 207-218.

[83] Staszewski, W.J., "Identification of Damping In MDOF Systems Using Time-Scale Decomposition," *Journal of Sound and Vibration*, Vol. 203, No 2, June, 1997, pp. 283-305.

[84] Robertson, A.N., Park, K.C., and Alvin, K.F., "Extraction of Impulse Response Data via Wavelet Transform for Structural System Identification," *Journal of Vibration and Acoustics*, Vol. 120, 1998, pp. 252-260.

[85] Lamarque, C.H., Pernot, S., and Cuer, A., "Damping Identification in Multi-Degree-Of-Freedom Systems via A Wavelet-Logarithmic Decrement - Part 1: Theory," *Journal of Sound and Vibration*, Vol. 235, No. 3, 2000, pp. 361-374.

[86] Hans, S., Ibrain, E., Pernot, S., Boutin, C., and Lamarque, C.H., " Damping Identification in Multi-Degree-Of-Freedom Systems via A Wavelet-Logarithmic Decrement - Part 2: Study of A Civil Engineering Building," *Journal of Sound and Vibration*, Vol. 235, No. 3, 2000, pp. 376-403.

[87] Stanway, R., Sproston, J.L., and EI-Wahed, A.K., "Application of Electrorheological Fluids in Vibration Control: A Survey," *Smart Materials and Structures*, Vol. 5, No. 4, 1996, pp. 464-482.

[88] Gavin, H.P., Hanson, R.D., and Filisko, F.E., "Electrorheological Dampers, Part II: Testing and Modeling," *SAME Journal of the Applied Mechanics*, Vol. 63, Sept., 1996, pp. 676-682.

[89] Markho, P.H. "On Free Vibrations With Combined Viscous and Coulomb Damping," American Society of Mechanical Engineers, *Journal of Dynamic Systems, Measurement and Control*, Vol. 102, 1980, pp. 283-286.

[90] Badrakhan, F., "Separation and Determination of Combined Dampings From Free Vibrations," *Journal of Sound and Vibration*, Vol. 100, 1985, pp. 243-255.

[91] Feeny, B. F., Liang, J. W., "A Decrement Method For The Simultaneous Estimation of Coulomb and Viscous Friction," *Journal of Sound and Vibration*, Vol. 195, 1996, pp. 149-154.

[92] Kamath, G.M., Wereley, N.M., and Jolly, M.R., "Characterization of Semi-Active Magnetorheological Helicopter Lag Mode Dampers," *SPIE's 5th International Symposium on Smart Structures and Materials*, San Diego, CA, march 1-5, 1998, pp. 3329-3337.

[93] Smith, C.B. and Wereley, N.M., "Transient Analysis for Damping Identification in Rotating composite Beams with Integral Damping layers," *Smart Materials and Structures*, Vol. 5, 1996, pp. 540-550.

[94] Smith, C.B. and Wereley, N.M., "Nonlinear Damping Identification from Transient Data," *AIAA Journal* Vol. 37, No.12, 1999, pp. 1625-1632.

[95] Zhao, Y. and Wereley, N.M., "Time Domain Damping Identification in Helicopter Rotor Systems," *42th AIAA SDM Conference*, 2001, AIAA-2001-1536.

[96] Nayfeh, A. H., and Mook, D. T., *Nonlinear Oscillation*, John Wiley & Sons, Inc., 1995.

[97] Bielawa, R.L., "Rotary Wing Structural Dynamics and Aeroelasticity," *AIAA Education Series*, 1992, pp. 276-286.

[98] Brackbill, C.R., Lesieutre, G.A., Smith, E.C., and Ruhl, L.E., "Characterization of the Low Strain Amplitude and Frequency Dependent Behavior of Elastomeric Damper Materials," *Journal of the American Helicopter Society*, Vol. 45, No. 1, 2000, pp. 34-42.

[99] Coleman, R.P., and Feingold, A.M. "Theory of Self-Excited Mechanical Oscillations of Helicopter Rotors with Hinged Blades," *NACA TR-1351*, 1956.

[100] Costes, N., "Semi-Active Damping of Ground Resonance in Helicopter Using Magnetorheological Dampers", M.S. Thesis, Dept. of Aerospace Engineering, University of Maryland, 2000.

[101] Gandhi, F., Wang, K. W., and Xia, L. "Magnetorheological Fluid Damper Feedback Linearization Control for Helicopter Rotor Application," *Smart Materials and Structures*, Vol. 10, No. 1, 2000, pp. 96-103.

[102] Hammond, C.E. "An Application of Floquet Theory to Prediction of Mechanical Instability," *Journal of the American Helicopter Society*, Vol. 19, No. 4, October, 1974, pp. 14-23.

[103] Hohenemser K.H., and Yin, S.K. "Some Applications of the Method of Multiblade Coordinates," *Journal of the American Helicopter Society*, Vol. 17, No. 3, 1972, pp. 3-12.

[104] Jang J. and Chopra I. "Ground and Air Resonance of an Advanced Bearingless Rotor in Hover," *Journal of the American Helicopter Society*, Vol. 33, No. 3, July, 1988, pp. 20-29.

[105] Johnson, W. *Helicopter Theory*, Dover Publications, 1980, pp. 668-693.

[106] Lindler, J. and Wereley, N.M. "Analysis and Testing of Electrorheological Bypass Dampers," *Journal of Intelligent Material Systems and Structures*, Vol. 10, No. 5, May, 1999, pp. 363-376.

[107] Lindler, J. "Double Adjustable Shock Absorbers Utilizing Electrorheological and Magnetorheological Fluids," M.S. Thesis, Dept. of Aerospace Engineering, University of Maryland, 2000.

[108] Wereley, N.M. and Lindler J. "Quasi-steady Biviscous Analysis of ER/MR Dampers," *Proceedings of the Tenth International Conference on Adaptive Structures and Technologies*, Paris,France, 1999, pp. 82-91.

[109] Snyder, R., Kamath, G.M., and Wereley, N.M. "Characterization and Analysis of Magnetorheological Damper Behavior Under Sinusoidal Loading," *AIAA Journal*, Vol. 39, No. 7, July, 2001, pp. 1240-1253.

[110] Marathe, S., Gandhi, F., and Wang, K. W. "Helicopter Blade Response and Aeromechanical Stability with a Magnetorheological Fluid Based Lag Damper," *Journal of Intelligent Material Systems and Structures*, Vol. 9, No. 4, 1998, April, pp. 272-282.

[111] Marathe, S., Wang, K. W., and Gandhi, F. "The Effect of Model Uncertainty On Magnetorheological Fluid Damper Based Systems Under Feedback Linearization Control," *Adaptive Structures and Materials Systems*, Vol. 57, 1998, pp. 129-140.

[112] Peters, D.A., and Hohenemser K.H. "Application of the Floquet Transition Array to Problems of Lifting Rotor Stability," *Journal of the American Helicopter Society*, Vol.16, No. 2, 1971, pp. 25-33.

[113] Wereley, N.M, Pang, Li, and Kamath, G.M. "Idealized Hysteresis Modeling of Electrorheological and Magnetorheological Dampers," *Journal of*

Intelligent Material Systems and Structures, Vol. 9, No. 8, August, 1998, pp. 642-649.

[114] Snyder, R., Wereley, N.M., and Sieg, T. "Mechanisms-based Analysis for Elastomeric Lag Damper Behavior Including Temperature Effects," *Annual Forum of the American Helicopter Society*, Washington DC, April, 2001.

[115] El-Ghezawi, O.M.E., Zinober, A.S.I., and Billings, S.A. "Analysis and Design of Variable Structure Systems Using a Geometric Approach," *International Journal of Control*, Vol. 38, No. 3, 1983, pp. 657-671.

[116] Slotine, J. E., and Li, W. *Applied Nonlinear Control*, Prentice Hall, 1991.

[117] Choi, S.B., and Choi, Y.T. "Sliding Mode Control of a Shear-Mode Type ER Engine Mount," *KSME International Journal*, Vol 13, No. 1, 1999, pp. 26-33.

[118] Choi, S.B., Choi, Y.T., and Park, D.W. "A Sliding Mode Control of a Full-Car Electrorheological Suspension System Via Hardware in-th-Loop Simulation ," *ASME Journal of Dynamic Systems, Measurement, and Control*, Vol 122, 2000, pp. 114-121.

[119] Misawa, E., "Robust Nonlinear Control System Design: an Overview," *Proceedings of the American Control Conference*, Vol. 3, 1992, pp. 1819-1823.

[120] Kanellakooulos, I. "Systematic Design of Adaptive Controllers for Feedback Linearizable Systems," *Proceeding of the American Control Conference*, 1991, pp. 649-654.

[121] Slotine, J.J., and Hedreick, J.K. "Robust Input Output Feedback Linearization," *Control of System with Inexact Dynamic Models* ASME DSC, Vol. 33, 1991, pp. 25-30.

[122] DeCarlo, R.A., "Variable Structure Control of Nonlinear Multivariable System: A Tutorial," *Proceedings of the IEEE*, Vol. 76, No.3, March 1988, pp. 212-232.

[123] Sanner, R.M., and Slotine, J.J. "Gaussian Networks for Direct Adaptive Control," *Proceedings of American Control Conference*, 1991, pp. 2153-2159.

[124] Young, P.M., "Structured Singular Value Approach For System with Parametric Uncertainty," *Internation Journal of Robust and Nonlinear Control*, Vol. 11, No. 7, June, 2001, pp. 653-680.

[125] Gueler, R., von Flotow, A.H., and Vos, D.W. "Passive Damping for Robust Feedback Control of Flexible Structures," *Journal of Guidance, Control, and Dynamics*, Vol. 16, No. 4, 1993, pp. 662-667.

[126] Bendat, J.S., and Piersol, A. G., *Random Data: Analysis and Measurement Procedures*, 2nd Ed., John Wiley and Sons Inc., New York, 1986.